Quantifying changes in climate and surface elevation of polar ice sheets during the last glacial-interglacial transition

Jessica Anne Badgeley

A dissertation
submitted in partial fulfillment of the
requirements for the degree of

Doctor of Philosophy

University of Washington

2022

Reading Committee:
Eric J. Steig, Chair
Gregory J. Hakim, Chair
Michelle R. Koutnik

Program Authorized to Offer Degree:
Earth and Space Sciences

University of Washington

Abstract

Quantifying changes in climate and surface elevation of
polar ice sheets during the last glacial-interglacial transition

Jessica Anne Badgeley

Co-Chairs of the Supervisory Committee:
Dr. Eric J. Steig
Earth and Space Sciences

Dr. Gregory J. Hakim
Atmospheric Sciences

This dissertation describes three research projects investigating changes in polar climate and the ice sheets during the last deglaciation. The first project, Chapter 2, reconstructs the past 20,000 years of Greenland temperature and precipitation to learn about their relationship and influences on the ice sheet. The reconstruction method, paleoclimate data assimilation, uses oxygen-isotope ratios of ice and accumulation rates from long ice-core records and extends this information to all locations across Greenland using spatial relationships derived from a transient climate-model simulation. Evaluations against out-of-sample proxy records indicate that the reconstructions capture the climate history at locations without ice-core records. The reconstructions show that the relationship between precipitation and temperature is frequency dependent and spatially variable, suggesting that thermodynamic scaling methods commonly used in ice-sheet modeling are overly simplistic. Overall, the results demonstrate that paleoclimate data assimilation is a useful tool for reconstructing the spatial and temporal patterns of past climate on timescales relevant to ice sheets. To learn how these climate reconstructions relate to the behavior of the ice sheet, we must also reconstruct the history of the ice sheet. Most observational data of the past ice sheet geometry, however, is at the margins of the ice sheet, while the ice core climate records are located in the interior.

The second project, Chapter 3, investigates a common paleoaltimetry method that reconstructs elevation from temperature records. This method suggests the climate and elevation signals contained within an ice-core temperature record can be disentangled by comparing two proxy locations with similar climates. The difference between the records is assumed to be due to elevation, which is estimated by scaling the temperature difference by a lapse rate. I investigate the errors associated with this approach using the Antarctic ice sheet during the Last Glacial Maximum as a case study. Using an ensemble of climate simulations from global circulation models (GCMs), I extract modeled temperatures at locations of real ice cores. The errors are on the order of hundreds of meters and result from spatial heterogeneity in non-adiabatic temperature change, which itself stems in part from elevation-induced atmospheric circulation change. These findings suggest that caution is needed when interpreting temperature-based paleoaltimetry results for ice sheets.

The third project, Chapter 4, seeks to learn about the elevation and climate signals contained within the WAIS Divide ice core temperature record by investigating whether they are consistent with accumulation rate reconstructions and annual layer thickness data at the ice core site. The difference in temperature change between West and East Antarctic ice core sites during the last deglacial period is about 6°C. If this were due to differential elevation change at the sites, then the WAIS Divide ice core site would have been about 400 m higher during the Last Glacial Maximum. Using an ice-flow model, I determine that this elevation change is not consistent with published accumulation rate reconstructions and the annual layer thickness data from the WAIS Divide ice core site. Three factors may explain this inconsistency: the spatial heterogeneity in non-adiabatic temperature changes during the deglaciation, assumptions in the accumulation rate reconstructions, and assumptions in the ice-flow model. Future investigations into these factors may lead to a more consistent understanding of Antarctic climate and interior ice sheet changes during the last deglaciation.

TABLE OF CONTENTS

ACKNOWLEDGMENTS

I thank my advisors, Eric Steig and Greg Hakim for their guidance and support throughout these past six years. I also thank Michelle Koutnik, Peter Blossey, T.J. Fudge, Josh Cuzzone, Marina Dütsch, Robert Tardif, Daniel Shapero, Gerard Roe, and Tim Essington for their helpful discussions and support throughout the years. I also owe a huge thanks to Erin Pettit, who inspired me to pursue this research and has never ceased to be my advocate.

I am grateful for my fellow grad students and postdocs in Earth and Space Sciences, the Women's Glaciology group, and the Steig and Hakim research groups. Emma Kahle, Katie Brennan, Gemma O'Connor, Lindsey Davidge, and Annika Horlings were there for me every step of the way. Finally, special thanks to my family, friends, and, in particular, Perry.

Funding for this research has been supported by the National Science Foundation Division of Graduate Education (grant no. 1256082). For Chapter 3, I also acknowledge 1) the high-performance computing support from Cheyenne (doi:10.5065/D6RX99HX) provided by NCAR's Computational and Information Systems Laboratory, sponsored by the National Science Foundation and 2) the World Climate Research Programme's Working Group on Coupled Modeling, which is responsible for CMIP. I thank the climate modeling groups (listed in Table B.2) for producing and making available their model output. For Climate Model Intercomparison Project, the U.S. Department of Energys Program for Climate Model Diagnosis and Intercomparison provides coordinating support and led development of software infrastructure in partnership with the Global Organization for Earth System Science Portals.

For Chapter 2, I thank my co-authors, Eric J. Steig, Gregory J. Hakim, and Tyler J. Fudge. We thank Robert Tardif for help with code development, and we thank Joshua

Anderson, Bo Vinther, Christo Buizert for their help compiling the ice-core data. We also thank the Snow on Ice project members for their discussions and support, especially Joshua Cuzzone, Jason Briner, and Elizabeth Thomas.

For Chapter 3, I thank my co-authors, Eric J. Steig and Marina Dütsch. We thank Gregory J. Hakim and Peter Blossey for their helpful discussions on the theoretical background for this work.

For Chapter 4, I thank my co-authors, Michelle R. Koutnik and Eric J. Steig. We thank Tyler J. Fudge for sharing code for the one-dimensional ice-flow model and for helpful discussions throughout the project.

DEDICATION

For Lianne, Bill, and Erica

Chapter 1
INTRODUCTION

Our understanding of how sensitive ice sheets are to climate change informs projections of sea level rise over the next century (Fox-Kemper et al., 2021). Such projections are created with models that incorporate our understanding of the physics of the Earth system and are tuned to match observations of the past. Historical records, including satellite data, have good spatial coverage at relatively high temporal resolution, but they only encompass the past several decades, a period which spans a small range of climate states. Paleo records are sparser and less well resolved, but cover a far wider range of climate and ice-sheet changes. This thesis is focused on enhancing our spatial knowledge of past changes in polar climate and ice sheets on multi-millennial timescales.

This introductory chapter provides background for the three main topics that this thesis encompasses: paleoclimate in the polar regions, past evolution of the Greenland and Antarctic ice sheets, and relevant types of data and models and methods used to combine them. For the first two topics, I next introduce open questions that this thesis seeks to address or that I have addressed in additional, parallel work. Last, I provide brief introductions to Chapters 2 through 4, and explain how each study evolved from and is motivated by the previous work. This introduction is followed by the main chapters, which include a manuscript published in *Climate of the Past*, a manuscript in review with *Geophysical Research Letters*, and a manuscript written for this thesis. In the concluding chapter, I capture how this body of work contributes to our understanding of past changes in polar climate and ice sheets, and provide recommendations for future work.

1.1 Polar Paleoclimate

Earth's orbital cycles determine the indensity, timing, and distribution of insolation, the energy received by the Earth from the Sun. During the Pleistocene, changes in insolation have contributed to a cycle of colder and warmer periods that, during the past one million years, alternate on 100,000-year intervals. These are known as glacial-interglacial cycles. As the Earth cools into a glacial period, ice sheets and glaciers can persist at lower elevations, and, along with sea ice, at lower latitudes. This expansion of ice raises the Earth's albedo, causing more shortwave radiation from the Sun to be reflected back to space which further cools the planet. Positive, or reinforcing, feedbacks like this ice-albedo feedback enhance cooling in a cooling climate and enhance warming in a warming climate. Other feedbacks, both positive and negative, enhance and diminish the effects of forcings (e.g., solar insolation, greenhouse gases, and volcanic emissions). Together, forcings and feedbacks determine the timing and magnitude of climate change.

Glacial-interglacial cycles are characterized by near-coincident changes in the Earth system. The most relevant for this thesis are changes in temperature, precipitation, greenhouse gases, sea level, ice sheet size, and atmospheric circulation. Glacial periods are colder, drier periods with lower levels of greenhouse gases, lower sea levels, and larger ice sheets, while interglacial periods are the reverse. Today, we are in an interglacial period called the Holocene that started 11,700 years ago, after the transition out of the last glacial period, which started 115,000 years ago. The Last Glacial Maximum (LGM) was about 20,000 to 26,500 years ago when the ice sheets were at their greatest extent (Clark et al., 2009). It is at the end of the LGM that most ice sheets began their retreat that continued through the last deglaciation and into the Holocene. Due to the relative abundance of climate and ice sheet data, this most recent glacial-interglacial transition is of particular interest for studying how the Earth system responds to large warming events and rapid rates of ice sheet retreat.

During the last deglaciation, global mean annual surface air temperatures rose by 6 to 7°C (Schneider von Deimling et al., 2006; Tierney et al., 2020; Osman et al., 2021), though

estimates from the literature in the last decade range from 2 to 8°C (Masson-Delmotte et al., 2006; Schneider von Deimling et al., 2006; Tierney et al., 2020, and references therein). In the Arctic, this warming was enhanced, with estimates ranging around 20°C for the center of Greenland (Cuffey et al., 1995; Dahl-Jensen et al., 1998; Buizert et al., 2014). Over Antarctica, estimates show a high degree of spatial variability despite the limited range in latitudes, with interior West Antarctic sites warming 10°C (Cuffey et al., 2016), interior East Antarctic sites averaging around 4°C (Buizert et al., 2021), and coastal sites and South Pole showing 6 to 7°C of warming (Kahle et al., 2021). This warming was accompanied by a doubling of precipitation rates over Antarctica (Fudge et al., 2016) and a greater increase over Greenland (Cuffey and Clow, 1997; Steig, 1997), which may have slowed but did not reverse the retreat of the ice sheets. As ice sheets retreated, sea levels rose by 120 to 135 m (Clark and Mix, 2002) with the largest contribution of about 100 m coming from ice sheets that no longer exist today (the Laurentide, Cordilleran, and Innuitian in North America and Scandinavian, Barents, and Kara in Europe, Scandinavia, and Russia). Greenland, Antarctica, and all other glaciers and ice caps contributed around 3 m, 14 to 21 m, and 6 m, respectively (Clark and Mix, 2002).

1.2 Past Evolution of the Greenland and Antarctic Ice Sheets

Ice sheets, like the Greenland and Antarctic ice sheets, are masses of ice on land that cover more than 50,000 square kilometers. These masses of ice are the result of a gradual accumulation of snow over time. The snow compacts to ice under its own weight, and ice builds up. When ice masses grow large enough, they flow under their own weight. Ice near the center (interior) of the mass flows out towards the margins. The boundaries where ice diverges and flows in opposite directions are called ice divides. For an ice sheet that is in steady state (i.e., not growing or shrinking), there is sufficient snow accumulating to replace the ice that is flowing away from the interior. As ice flows, it encounters bumps in the underlying bedrock, slippery patches of basal water or sediment, and changing temperature conditions at the surface and base. These conditions can cause the ice to change in a number of ways,

for example, flow faster or slower, thicken or thin, develop damage in the form of crevasses, melt at the base or surface, or fold over itself. For this reason, ice coring missions that are after high-quality climate records tend to drill near divides where the ice flow history is much simpler.

As the ice approaches the margin, in many places it is channeled into faster-flowing outlet glaciers. These glaciers may terminate on land or in the ocean. If the latter, then an ice shelf (wide) or an ice tongue (narrow) may form that floats on the ocean but is still connected to the ice sheet that is grounded on land. The transition between grounded and floating ice is called the grounding line. For an ice sheet that is in steady state, the ice at the margin will be ablating at the same rate that ice is being brought in from the interior. Ablation can occur through melting at the surface due to warm atmospheric temperatures, melting at the base due to warm ocean temperatures, or breaking off icebergs into the ocean (calving). An ice sheet with a negative mass balance loses more ice than it gains, while a positive mass balance implies more gain than loss. Surface mass balance specifically refers to the net mass change at the ice-atmosphere interface.

The Greenland ice sheet sits on the continent of Greenland at the northern end of the Atlantic Ocean and spans twenty degrees of latitude (60 to 82°N). The ice sheet today holds enough ice to raise global sea level by 7.42±0.05 m (Morlighem et al., 2017). It has a main divide that runs roughly North-South and branches in the North with one branch going Northeast and the other to the West. From the divide, the ice gently slopes towards the margin where outlet glaciers are channeled through the mountainous ring that surrounds much of the continent, before terminating either on land or in the ocean. For the latter, the glacier termini are commonly in a fjord and may form ice tongues. About half of the ablation occurs through surface melt and half occurs through calving (Alley et al., 2010; Khan et al., 2015). Greenland's mass balance is particularly susceptible to warming air temperatures melting ice and causing accelerated rates of ice loss (Alley et al., 2010; Bindschadler et al., 2013). This sensitivity is due to Greenland's relatively warm climate (compared to Antarctica) and shallow surface slopes. If warming causes the elevation at which air tem-

peratures are freezing (0°C) to increase, then vast portions of the ice sheet will be exposed to above-freezing temperatures and have the potential to melt.

The Antarctic ice sheet sits over the geographic south pole and extends northward towards the Southern Ocean to an average latitude of 70°S. Typically, this ice sheet is referred to as two ice sheets, the East and West Antarctic ice sheets (EAIS and WAIS, respectively), with the dividing line being along the Transantarctic Mountain Range. East Antarctica hosts the larger ice sheet, which has the potential to raise sea level by 52 m, while West Antarctica hosts the smaller ice sheet, which could raise sea level by about 5 m (Lythe and Vaughan, 2001). Though some outlet glaciers terminate on land – on the Peninsula and along the western edge of the Ross Sea – most terminate in the ocean where ice shelves are prevalent. These ice shelves vary widely in size with the two largest ice shelves, the Ross and the Ronne-Filchner, each covering areas equivalent to the size of California. Pinned at the sides by land and in the middle by islands, the ice shelves act as a buttress to the ice on land. When these ice shelves collapse, the land ice flows faster, as happened to some glaciers on the Antarctic Peninsula after the Larsen B ice shelf collapsed in 2002 (Rignot et al., 2004). Much of the ablation in Antarctica occurs at the ice shelf both from calving and from warm ocean water entering the cavity beneath the shelf and melting the underside (Rignot et al., 2019). Due to the year-round cold climate, very little surface melting occurs except on the Peninsula (Zwally and Fiegles, 1994).

The EAIS is thought to be the most stable of all ice sheets over glacial-interglacial cycles, while the WAIS is thought to be the most unstable of the modern ice sheets. Here I explain two of many factors that influence the magnitude and rate of ice-sheet advance and retreat as climate changes. One factor is the average climate around which temperature and accumulation fluxes occur. Antarctica tends to be colder than Greenland, which means that it takes much larger increases in air temperature to induce melting, especially at higher elevations. Another factor is the geometry of the bed on which the ice sheet sits. This is partially affected by the ice sheet itself; the immense weight of the ice depresses the bed beneath it. For marine-terminating glaciers and ice sheets, the shape of the bed deter-

mines the sign of the feedback. A bed that slopes down towards the center of the ice sheet (a retrograde bed slope) creates a positive feedback such that an externally-forced retreat into deeper water triggers additional retreat (Schoof, 2007). A bed that slopes up towards the center (a prograde bed slope) provides a negative (stabilizing) feedback. The WAIS is believed to be the modern-day ice sheet that is most sensitive to small fluctuations in the grounding line position because it sits in a deep bedrock bowl that is over 1,000 m below sea level (Morlighem et al., 2020). In contrast, the Greenland ice sheet sits in a gentle bowl that is up to 200 m below sea level at the center (Morlighem et al., 2017) and much of the EAIS sits on a bed that is hundreds of meters above sea level (Morlighem et al., 2020). The EAIS, however, has several marginal basins, some of which are up to 1,000 m or more below sea level (Morlighem et al., 2020) and are also thought to be quite sensitive to grounding line perturbations.

At the LGM, the Greenland ice sheet extended farther out onto the continental shelf and, in southern Greenland, to the shelf break (Alley et al., 2010 and references therein). In this extended state, the ice sheet held an additional 3 m of equivalent sea level (Clark and Mix, 2002), much of which was distributed towards the margins of the ice sheet (Alley et al., 2010). Likely driven primarily by sea level rise, the ice started retreating around 21 to 18 thousand years before present (ka BP) and reached the modern-day coastline at the start of the Holocene (Alley et al., 2010; Lesnek et al., 2020). Much of the evidence for this period of retreat is currently below sea level, which makes it difficult to study. After the margin reached the modern coastline, however, glacial erratics, moraines, and lake sediments provide a more comprehensive record of margin retreat and advance. There is a particularly clear record of Holocene retreat in southwest Greenland (Young and Briner, 2015; Briner et al., 2020). Though the exact timing, rate, and magnitude of ice margin change varies around Greenland, the broad picture of retreat after the Younger Dryas is similar (Alley et al., 2010). Re-advances and standstills are marked by moraines in the early Holocene, some of which coincide with anomalously cold periods in ice core records (Young et al., 2020). In the mid-Holocene, the ice reached a smaller-than-present minimum extent that is commonly

connected to the Holocene thermal maximum, a period when Greenland was, on average, several degrees warmer than the pre-industrial period (Kaufman et al., 2004). After a few thousand years of relative stability, the margin re-advanced to its modern position during the last few thousand years (Young and Briner, 2015).

During the last glaciation, much of the West Antarctic ice sheet extended out to the edge of the continental shelf; however, the exact timing of the maximum grounded ice extent remains unclear in many locations (The RAISED Consortium, 2014). Here, I focus on the timing of deglaciation in the Ross Sea and Amundsen Sea sectors as they are located on either side of the the ice divide near the WAIS Divide ice core site, the subject of Chapter 4. The Weddell Sea sector is the other main outlet for ice in West Antarctica and, while it shares a divide with both the Ross and Amundsen Sea sectors, it likely had less influence on the WAIS Divide ice core site because 1) the Weddell Sea sector is thought to have had low volumes of excess ice during the LGM (Hillenbrand et al., 2014) and 2) the Weddell-Amundsen divide was likely stable throughout the Holocene and maybe longer (Ross et al., 2011).

Grounded ice filled much of the Ross Sea at the LGM, and, in the western Ross Sea, it reached its greatest extent and thickness between 18 and 12 ka BP (Hall et al., 2015). There remains a lack of evidence about the early stages of retreat, however, geologic data suggests that the northern edge of the western Ross Sea sector began to retreat at or just after an abrupt rise in eustatic sea level (meltwater pulse 1a around 14.6 ka BP) (Goehring et al., 2019). Additional evidence suggests that the grounding line reached the mouths of most Transantarctic Mountain outlet glaciers along the western edge of the Ross Sea around 8 ka BP (Spector et al., 2017). This retreat occurred after temperatures and accumulation rates had already begun to rise, so was likely triggered by eustatic sea level rise and enhanced by unstable retreat on reverse bed slopes (Spector et al., 2017; Goehring et al., 2019). A wave of dynamic thinning resulting from this retreat likely propagated upstream into the interior of the ice sheet. In the Amundsen Sea embayment, grounded ice reached the edge of the outer continental shelf (The RAISED Consortium, 2014). Ice retreated most quickly in this

region around 13 ka BP and reached the modern grounding line by about 10 ka BP (Larter et al., 2014; The RAISED Consortium, 2014). At most locations around West Antarctica, the grounding line and ice thickness reached the modern position and level within the last last 7,000 years (Stone et al., 2003; The RAISED Consortium, 2014; Spector et al., 2017, 2019).

1.3 Observational Data, Numerical Models, and Methods to Combine Them

Insights gained about the history of climate and ice sheets are inseparable from both the questions asked and the methods used. In this thesis, I both explore and emphasize ways to combine observational data and numerical models. First, however, it is helpful to understand the types of data and models and their respective strengths and weaknesses.

There are numerous ways that past climate and ice sheet changes are archived in rocks, sediment, biological material, and ice. For each of these types of archives there are multiple records that can be produced from measuring a variety of chemical, biological, and physical properties. Many of these records are called proxies because they are not direct measurements of the variable of interest (e.g., temperature), but instead are strongly (or weakly) related to that variable. Here, I give a brief introduction to ice cores and glacial geologic data, which are the two sources of paleoclimate and ice sheet data that show up most commonly in this thesis and my related work.

Ice cores are an important source of information for learning about the polar regions because each one contains a multitude of records all dated on the same, high-resolution, low-uncertainty timescale. Temperature and accumulation rates are two of the climate variables that exert a strong control over ice sheet size and for which there are highly-developed proxy records from ice cores. Temperature is preserved in several different proxy records in ice cores. In Chapter 2, I focus on oxygen isotopes of ice (δ^{18}O), and, in Chapter 3, I simply refer to temperature reconstructions from ice cores and am agnostic to the proxy record or method used to derive the reconstruction. Through the well-understood process of Rayleigh distillation (Dansgaard, 1964), oxygen isotopes of water undergo fractionation

from their evaporation source to the site of precipitation. The amount of fractionation that these isotopes undergo is strongly related to the temperature at the site of deposition (Johnson et al., 1989). Empirical relationships between the final isotope value (δ^{18}O) and the site temperature have been calculated from modern samples around Greenland and Antarctica (Johnsen et al., 1989; Jouzel et al., 2003). There are other factors, however, that influence δ^{18}O to greater or lesser extents that must be accounted for (e.g., Jouzel et al., 1997; Pausata and Löfverström, 2015). I discuss these factors more thoroughly in Chapter 2. In addition to δ^{18}O, other temperature proxies include borehole thermometry, δ^{15}N of N_2 (nitrogen gas isotope ratios), Δage (the difference between the ice and gas age in the ice core), and the diffusion length of water isotopes (e.g., Cuffey et al., 1995; Dahl-Jensen et al., 1998; Severinghaus et al., 1998; Severinghaus and Brook, 1999; Buizert et al., 2021; Kahle et al., 2021). Each of these proxies is strongly related to temperature or temperature change, reflects a different suite of processes, and requires its own assumptions to estimate temperature. Together, they can be combined to come up with a more robust estimate of paleotemperatures in the polar regions (e.g., Buizert et al., 2021; Kahle et al., 2021).

Accumulation rates are preserved by the thickness of the annual layers of snowfall. These layer thicknesses can be derived from the depth-age scale for the ice core. If the layer of ice for a given year is thick enough (which is more likely the case for younger ice), then in some cores a seasonal cycle may be seen visually as alternating layers of light and dark (dusty) ice that reflect the summer and winter seasons, respectively. Certain chemical species and particulates also show seasonal signals and are measured to verify the visual layer counting (e.g., Sigl et al., 2016). Other techniques are used to improve the depth-age scale, especially at deeper depths where layers are too thin to reliably count (e.g., Buizert et al., 2015). The layer thicknesses, however, are not a direct measurement of accumulation rate because layers of ice thin as they are advected down through the ice sheet. This thinning history can be modeled with known and assumed parameters and used to calculate accumulation rates from annual layer thicknesses.

There are many types of glacial geologic data that indicate the extent and/or thickness

of an ice sheet. The data types that we rely on in Briner et al. (2020), the follow-on study to my Chapter 2, and that I refer to in Chapter 4, are moraines and exposure ages of glacial erratics. As ice flows, it carries rocks that fell on the surface or that it picked up at the bed. These rocks are deposited at the ice margins where they form moraines or more scattered deposits of glacial erratics. As an ice sheet advances, it can override moraines and erratics and either erase them from the landscape if the ice is wet at the base and erosional (e.g., in Greenland) or preserve them if the ice is frozen to the bed (e.g., much of Antarctica). As an ice sheet retreats, it leaves the moraines and erratics behind as a record of its past extent. These deposits can be dated by measuring the concentration of cosmogenic radionuclides in them in a method called exposure dating (see Ivy-Ochs and Kober, 2008, for a review of this method and its many applications). The radionuclides accumulate in a rock when it is exposed at the surface and decay. By measuring the concentration of these radionuclides, the amount of time that the ice has been exposed at the surface and the amount of time it has been covered can be estimated. In the simple case of a rock having been covered by the ice sheet before being deposited in a moraine or as an erratic, the exposure age can be interpreted as the age of the moraine or the time when the ice margin was last at the location of the deposit. In a more complicated scenario of multiple ice advances and retreats, the measurement of multiple radionuclides with different half-lives can be used to help constrain the ice-sheet history (e.g., Schaefer et al., 2016).

Ice cores and glacial deposits are types of data we get directly from the Earth, but another way to study the Earth system is to use models. There are many different types of models, for example, theoretical, physical, conceptual, empirical, statistical, and numerical. Any model can be made more or less complex to suit the needs of an investigation. Here I will discuss numerical models and the different levels of model complexity that are used in this thesis and my related work.

Numerical models of the Earth system are made up of the equations that are to be solved, a method to solve those equations, initial conditions, and boundary conditions (also known as forcings in some contexts). The equations describe our understanding of the physical

processes and may be derived from foundational laws of physics, from observed data, from theory, or from a combination of these. When these equations cannot be solved analytically, which is often the case for real-world applications, they must be solved numerically. To simulate an evolution of the system through time, an initial state of the system is prescribed that is then allowed to evolve according to the equations and external forcings. The simplest numerical models solve a smaller set of equations that isolate a single process or group of processes and may also have a reduced number of dimensions. These simpler models make it easier to identify causes, effects, and the mechanisms that connect them. Often they are used to understand the fundamental nature of a process without the clutter of secondary effects and feedbacks. The Earth system is rarely reduced to one fundamental process, however, so more complex models include more interacting processes and more dimensions. These more complex models are used to learn about the impact of these secondary effects and feedbacks and to try to simulate the real system to compare to observational data.

General circulation models (GCMs) and Earth system models (ESMs) are the most complex climate models. They are usually composed of individual models for different components of the system, for example, the atmosphere, ocean, land, sea ice, ice sheets (some), and geochemical systems, that are then coupled together. A full three-dimensional ice sheet model is on the more complex end of ice-flow models, often using unsimplified equations and including more processes (e.g., calving, damage, subglacial hydrology, sub ice-shelf melting, etc.). Flowline, flowband, and one-dimensional ice-flow models tend to make different approximations and reductions to the equations describing ice flow and target limited domains for which the simplified physics are known to be good approximations.

The limitations of observational data mirror the strengths of numerical models and vice versa. The data provide records of what happened, though interpreting them can be difficult due to multiple, interacting processes. Disentangling these processes can be difficult because several may impact the record in the same way and some processes may be poorly understood. Paleoclimate and paleo ice sheet data are also often sparse in space and across time leading to large gaps that may shield or confuse our understanding. Numerical models incorporate our

understanding of the physics of a system and can provide continuous information across space and in time. They do not, however, tell us what happened. There is too much uncertainty in the small-scale physics, the initial conditions, and the boundary conditions of a model to reproduce reality.

By combining data and models, we can leverage their respective strengths to reduce the uncertainty in our understanding of Earth's history. In my research for this thesis, I have explored three different ways to leverage data and models together to learn about the Earth system: 1) formal combination (assimilation) of data and numerical models as used in Chapter 2, 2) models as a tool for interpreting data as used in Chapter 3, and 3) data used as inputs to or evaluation of numerical models as used in Chapter 4 and Briner et al. (2020). I chose each of these depending on the question, the available data and numerical models, and the state of method development for each field.

1.4 Questions Concerning Climate and Ice Sheet Evolution Over the Last 20,000 Years

Though there is much that we have learned about the last glacial transition, numerous questions remain about climate and ice-sheet change during this time. To better understand the climatic context and how ice sheets responded, I target the following seven questions (and note the chapters or related work that address them in parentheses).
The first three questions relate primarily to climate:

1. How does the relationship between temperature and precipitation vary in space and time across Greenland during the last glacial-interglacial transition? (Chapter 2)

2. Is climate variability stronger in northern or southern Greenland on glacial-interglacial timescales? (Chapter 2)

3. What caused the difference in East and West Antarctic temperature change over the last deglaciation? (Chapters 3 and 4)

The last four questions relate primarily to ice sheets:

4. Will future retreat rates of the Greenland ice sheet outpace rates of change experienced during the last deglaciation and over the Holocene? (Briner et al., 2020)

5. Did accumulation rates enhance or moderate retreat of the Greenland ice sheet during the last deglaciation and the Holocene? (Briner et al., 2020; Young et al., 2021)

6. Has a dome of ice in Southern Greenland survived extensive warming above pre-industrial levels? (Osterberg et al., 2020)

7. What elevation was the interior of the West Antarctic ice sheet at the Last Glacial Maximum? (Chapters 3 and 4)

In the remainder of this section, I briefly explain the context around each of these seven questions. For the questions that I have addressed outside of this dissertation (4, 5, and 6), I also include a brief description of the current results of my collaborative investigations.

1. How does the relationship between temperature and precipitation vary in space and time across Greenland during the last glacial-interglacial transition? We know from numerous proxy records how temperature changed around Greenland during the last glacial-interglacial transition. Precipitation records, however, are much sparser, leaving us with a poorer understanding of these changes. To remedy this, studies, particularly those that apply numerical modeling to understanding past changes in the ice sheet, reconstruct precipitation by scaling temperature using a single relationship across space and time (e.g., Huybrechts, 2002; Greve et al., 2011). This scaling has a foundation in our understanding of water vapor and thermodynamics (via the Clausius-Clapeyron relation), but it has been shown by models and data that it does not capture important aspects of precipitation changes (e.g., Kapsner et al., 1995; Fudge et al., 2016; Cuffey and Clow, 1997).

2. Is climate variability stronger in northern or southern Greenland on glacial-interglacial timescales? Though temperatures across Greenland during the last deglaciation are con-

strained by numerous high-quality records from ice cores, there remains a discrepancy between some of these records. Reconstructions from water isotopes of ice indicate greater temperature variations in northern Greenland, while reconstructions from isotopes of nitrogen gas and a transient climate model simulation point to greater variability in southern Greenland (Buizert et al., 2014; Liu et al., 2009, 2012). Whether variability was stronger in the North or South has different implications for the dominant mechanism(s) driving temperature change over Greenland during the deglaciation. If variability was higher in northern Greenland, this points to a dominating effect of Arctic amplification and perhaps local influences of changes in the other Northern Hemisphere ice sheets (Badgeley et al., 2020). If variability was higher towards the South, this points to stronger connections between Greenland temperature and the Atlantic meridional overturning circulation (Buizert et al., 2014).

3. What caused the difference in East and West Antarctic temperature change over the last deglaciation? In contrast to Greenland climate variability, there is a greater consensus that temperature changed more in West Antarctica than in East Antarctica during the last deglaciation (Cuffey et al., 2016; Buizert et al., 2021; Kahle et al., 2021). The reason for this differential temperature change, however, remains uncertain. The leading hypothesis is differential elevation change, where the interior of the West Antarctic ice sheet (WAIS) is argued to have lowered by several hundred meters while the interior of the East Antarctic ice sheet (EAIS) is widely thought to have remained within 100 m of its current elevation (e.g., Werner et al., 2018; Buizert et al., 2021). As the surface of an ice sheet rises and lowers, the atmospheric temperature lapse rates cause it to cool and warm. In addition to these elevation-induced (adiabatic) temperature changes, other forcings, such as radiative effects from changing greenhouse gas concentrations or changing atmospheric circulation (diabatic effects), contribute to the total temperature change experienced at the ice sheet surface. Some of the diabatic effects may also induce spatially heterogeneous changes in temperature, but model simulations suggest it is not sufficient to explain the East-West temperature differential (Werner et al., 2018; Buizert et al., 2021). Despite this, there is

strong data evidence that the interior of the WAIS could not have changed elevation enough to account for the spatial variability in temperature change (Cuffey et al., 2016; Spector et al., 2019). If it turns out that the interior WAIS did not lower by several hundred meters during the last deglaciation, this implies that there is an undetermined mechanism influencing the spatial pattern of temperature change across Antarctica.

4. Will future retreat rates of the Greenland ice sheet outpace rates of change experienced during the last deglaciation and over the Holocene? One reason for investigating paleo ice-sheet behavior during a time period like the last deglaciation is to help contextualize and predict how ice sheets are responding to current climate change and may respond to future warming. The transition out of the last glacial period is the most recent, large, abrupt warming event. Though it is far from a perfect analog for modern and future change, we can use it both to learn about how the Earth system responds to such events and as a benchmark for comparison of present and predicted future rates of change. We focus on Greenland here because it is more susceptible to warming air temperatures and because it has had a clearly negative mass balance for the past four decades (Mouginot et al., 2019). This does not preclude a similar analysis from being done for Antarctica.

A team of collaborators and I set out to compare the Holocene, present, and predicted future changes in rates of mass loss from the Greenland ice sheet. We combined climate reconstructions, an ice sheet model, and glacial geologic data to create self-consistent simulations of past and future ice-sheet change (Briner et al., 2020). We focused on simulating just the southwest portion of the ice sheet over the last 12,000 years because that region and time period have the most glacial geologic data available for comparison. I produced the climate reconstructions by assimilating ice core water isotope and accumulation rate data with a transient simulation of the last 21,000 years (Badgeley et al., 2020). We used these data-informed reconstructions as boundary conditions for the Holocene ice sheet simulations, which we compared to glacial geologic data. For the modern and future simulations, we used a historical climate reanalysis (Box, 2013) and an ensemble of climate model simulations as boundary conditions. By using the same ice sheet model run from the past and into the

future, we could examine how one set of glaciological assumptions (the model) responded to the reconstructed and projected climate conditions. We found that the rate of Greenland ice sheet mass loss will exceed rates experienced in the Holocene unless anthropogenic greenhouse gas emissions are severely reduced soon (Briner et al., 2020).

5. Did accumulation rates enhance or moderate retreat of the Greenland ice sheet during the Holocene? Reconstructing the past not only provides a source of comparison, but it can also teach us about how different components of the Earth system interact. On glacial-interglacial timescales the Greenland ice sheet primarily responds to changes in temperature by growing during times of cooling and retreating during times of warming (Alley et al., 2010). Sea level change and accumulation rates affect the ice sheet as well, and can act to enhance or moderate the timing and pace of ice-sheet change. Accumulation rates are thought to moderate the pace of ice-sheet change because they tend to be higher in warmer climates and lower in cooler climates (as expected from the Clausius-Clapeyron relation between temperature and water vapor pressure). It is less clear, however, what role accumulation rates play on shorter timescales and under different climate regimes. With the goal of understanding how changes in accumulation rates may or may not help to moderate ice loss in the future, we investigated the Holocene thermal maximum as an analog for the future because 1) it was several degrees warmer than the pre-industrial period (Kaufman et al., 2004) and 2) we have more records about climate and ice-sheet change than from earlier warm periods.

The ice sheet simulations from Briner et al. (2020) provide an opportunity to address the question of how accumulation rates affected Greenland ice sheet retreat during the Holocene. Though a quantitative analysis has not yet been completed, insights into this question are included in both Briner et al. (2020) and Young et al. (2021). The paleoclimate boundary conditions for the Holocene ice sheet simulations are an ensemble of independent temperature and precipitation reconstructions from Badgeley et al. (2020). The independence is key because it also allows us to pair each of the temperature reconstructions with each of the precipitation reconstructions to explore how different combinations of warming and

accumulation rates lead to different realizations of ice sheet retreat.

We find that simulations with cooler temperatures in the early Holocene fit best to data in the Kangerlussuaq region, while simulations with warmer temperatures in the early Holocene fit best to data in the Nuuk region (Briner et al., 2020). The Kangerlussuaq region contains mostly land-terminating glaciers and tends to be driven primarily by changes in the surface mass balance. In contrast, the Nuuk region has many fjord-terminating glaciers that additionally experience calving and submarine melting. These ocean processes are not included in the ice sheet model and the warmer temperatures required to fit the data may be compensating for these missing dynamics (Young et al., 2021). Thus, the comparison to the data in the Kangerlussuaq region is more likely to reveal the respective roles of temperature and precipitation in regulating ice sheet retreat. In that region, pairing the low temperature reconstruction with high and moderate levels of early Holocene precipitation yields the best fit both to the timing of the minimum extent of the ice sheet (driven mostly by temperature) and to the moraine chronology (driven also by precipitation) (Young et al., 2021). These findings suggest that precipitation did moderate Greenland ice sheet retreat during the Holocene.

6. Has a dome of ice in Southern Greenland survived extensive warming above pre-industrial levels? Many areas in Greenland, including southwest Greenland and the central summit area, are susceptible to extensive retreat in the face of warming above pre-industrial levels (Schaefer et al., 2016). The two areas that models show ice persisting despite warming are South Dome and the parts of eastern Greenland that receive the highest amounts of precipitation (Schaefer et al., 2016). These locations provide an opportunity to test a hypothesis about the most stable parts of the Greenland ice sheet (Osterberg et al., 2020). Because it is a dome, South Dome is the likelier of the two to contain a high-quality climate record that reaches back to at least 40 ka BP, which allows the ice to be more easily dated and matched to past climate events. In Osterberg et al. (2020), we propose South Dome as a future ice core drilling site as the first step towards retrieving the data necessary to address this question.

7. What elevation was the interior of the West Antarctic ice sheet at the Last Glacial Maximum? In contrast to the potential stability of South Dome in Greenland, the WAIS is reasoned to be the most sensitive and potentially dynamic of the modern ice sheets. Similar to South Dome, however, it remains unclear how much it has changed in the past, especially in the interior. Much of the observational evidence for WAIS change comes from exposure ages of bedrock and glacial erratics, ocean sediment cores, and sea level data. The sites where this data has been and can be collected are typically around the margins of the ice sheet, with the most interior sites being nunataks that are still far from ice core sites. This leaves us without strong evidence for how the interior of the ice sheet has changed in the past.

1.5 Introduction of Dissertation Chapters

Some of the strongest constraints on past climate and ice-sheet change are from ice core records and dated glacial deposits, respectively. These datasets, however, are from different areas of the ice sheet with ice cores being located at the center near ice divides and most glacial deposits being around the edges of the ice sheet. Extrapolating climate or ice-sheet change to another site faces the difficulty of needing to know both the spatial patterns of the changes and any lags in the system. Models can help by applying our understanding of the physics of the systems.

Chapter 2, originally published as Badgeley et al. (2020) in *Climate of the Past*, shows how climate models and ice core records can be combined with a formal data assimilation technique, the ensemble Kalman filter, to create spatially-complete reconstructions of temperature and precipitation across paleo timescales. Evaluation shows that the reconstruction is an improvement over the model alone and is likely to provide high-quality information beyond the sites of the assimilated ice core records. With these reconstructions, I address questions one and two (from Section 1.4) concerning the relationship between temperature and precipitation and the North-South temperature variability over Greenland during the last deglaciation. Towards the first question, I find that the temperature-precipitation re-

lationship is spatially variable and only follows the theoretical scaling on glacial-interglacial timescales. In response to the second, I find that temperature is more variable in the North; however, this finding is dependent on the climate simulation used for the reconstruction, indicating that the data constraints are not currently strong enough to definitively answer this question.

As a follow-on to my investigations into Greenland paleoclimate, I worked with a team to apply these temperature and precipitation reconstructions as boundary conditions for a numerical ice sheet model (Briner et al., 2020). Though this work is not included in this thesis, it represents a significant contribution that I made to the fields of paleoclimatology and paleoglaciology. The ice sheet model bridges the gap between my climate reconstructions and information about paleo extents of the Greenland ice sheet gathered from dated moraines and lake sediment cores. We find that the ice sheet model forced by my climate reconstructions agrees reasonably well with the geologic constraints on ice sheet extent, indicating that the climate data from ice cores at the center of the ice sheet are consistent with ice sheet data at the margins. Though this agreement is promising, questions remain about how accurate the climate reconstructions are at the margins of the ice sheet and how well the ice sheet model captures changes away from the ice margin in the interior.

From Chapter 2 and Briner et al. (2020) we learn that models are helpful tools for extrapolating information from data sites to other locations, however, questions can remain about the validity of model results in locations where there is little-to-no data available for evaluation. Such questions could be resolved with co-located records of climate and ice-sheet change. An additional reason for obtaining co-located data is that the complete interpretation of temperature records from ice cores requires knowledge of how the ice sheet changed at or near the site of the record.

Chapters 3 and 4 explore ways to obtain elevation information that is co-located with ice core sites. For these chapters I shift my focus to Antarctica where there is a lack of consensus about the elevation change of the interior West Antarctic ice sheet (WAIS) over the last deglaciation. Before exploring novel means for reconstructing elevation change at

ice core sites in the WAIS interior, I focus Chapter 3 on assessing a temperature-based paleoaltimetry method that has been applied to ice cores (Steig et al., 2001; Vinther et al., 2009) and is commonly used in the broader paleoaltimetry literature (Meyer, 2007, and references therein). This method estimates elevation by using a lapse to scale the difference between two temperature records that are assumed to have experienced the same climate (diabatic temperature) change. Using an ensemble of climate simulations of the LGM and pre-industrial period, I investigate the source and magnitude of the uncertainties in reconstructing Antarctic elevation change during the last deglaciation. I find that the errors in the elevation estimates are on the order of hundreds of meters, leading to estimates that are likely to be insufficiently precise to narrow the current bounds on WAIS elevation change.

Chapter 3 addresses question three from Section 1.4, concerning the reason for the East-West temperature change differential during the last deglaciation. Similar to previous studies (e.g., Werner et al., 2018; Buizert et al., 2021), the climate simulations indicate that this spatial pattern in temperature change is due to differential elevation change. This finding, however, does not preclude the possibility of an unidentified mechanism that may be missing from or misrepresented in the climate models.

With the results from Chapter 3 indicating that the temperature-based paleoaltimetry method is insufficient for reconstructing elevation at ice core sites, Chapter 4 seeks a new way to gain insight into elevation change during the last deglaciation. There have been efforts to do this previously, for example by interpreting total air content from ice cores as elevation (e.g., Raynaud, 1979; Buizert et al., 2021), but there remain large uncertainties (e.g., Martinerie et al., 1994; Krinner et al., 2000). These efforts have not been able to sufficiently reduce the uncertainty to meaningfully contribute to ice sheet reconstructions (Briggs and Tarasov, 2013). In Chapter 4, I focus on learning about elevation change at the WAIS Divide ice core site by investigating whether thinning histories implied by published elevation changes are consistent with a) the currently accepted accumulation rate histories from the WAIS Divide ice core, b) the high-quality and low-uncertainty layer thickness data from the ice core, and c) two glaciological models of different complexity. In response to

question seven from Section 1.4 concerning the height of the WAIS at the LGM, I find that the thinning histories that are most consistent with currently accepted accumulation rate histories, layer thickness data, and glaciological models have the least amount of elevation change. This is the leading order effect over all other variables we tested in the models. This finding also has implications for question three from Section 1.4: if elevation did not change very much in the WAIS interior, what other mechanisms could have caused the differential East-West temperature change during the last deglaciation? This is a question to be addressed by future work, as discussed in Chapter 5.

Chapter 2

GREENLAND TEMPERATURE AND PRECIPITATION OVER THE LAST 20,000 YEARS USING DATA ASSIMILATION

Jessica Badgeley, Eric J. Steig, Gregory J. Hakim, and Tyler J. Fudge

Originally published in Climate of the Past

2.1 Introduction

Predicting the future behavior of the Greenland ice sheet requires understanding its sensitivity to changes in temperature and precipitation (Bindschadler et al., 2013). One important constraint on this sensitivity is the response of the paleo ice-sheet to changing climate in the past. On glacial-interglacial timescales, temperature, not precipitation, appears to be the dominant control on the size of the Greenland ice sheet (Alley et al., 2010), as evidenced by the fact that the ice sheet is largest during cold and arid glacial periods and smallest during warm and wet interglacials. On these timescales, precipitation over the Greenland ice sheet scales positively with temperature (Robin, 1977), as anticipated by the Clausius-Clapeyron relation between temperature and saturation vapor pressure. Ice-core records, however, show that this thermodynamic relation is a poor approximation on annual to multi-millennial timescales (Kapsner et al., 1995; Fudge et al., 2016). For example, the GISP2 ice core from central Greenland shows that cooling coincided with increased snowfall between the early Holocene and present (Cuffey and Clow, 1997). Despite such evidence, paleo ice-sheet models typically assume precipitation fields that are parameterized in time using a thermodynamic relationship that is constant for all locations and timescales (e.g., Huybrechts, 2002; Greve et al., 2011).

Ice-core records provide the best empirical estimates of climate history over the Green-

land ice sheet. For temperature, important proxies include oxygen and hydrogen isotopes of ice (e.g., Jouzel et al., 1997), nitrogen isotope ratios of gas trapped in ice (e.g., Severinghaus et al., 1998; Severinghaus and Brook, 1999), and borehole thermometry (e.g., Cuffey et al., 1995; Dahl-Jensen et al., 1998). For precipitation, the thickness of annual layers of accumulated ice, corrected for thinning, is used (e.g., Dahl-Jensen et al., 1993). Ice-core records, however, are limited in their spatial coverage. In contrast, climate-model simulations are spatially-complete estimates of past climate, but they are subject to uncertainty due to model dynamics, boundary conditions, and spatial resolution.

Efforts to combine information from proxy data and climate models have long been a part of ice-sheet modeling. The most common approach is to scale the modern spatial pattern of temperature and precipitation using data from a single ice core (e.g, Huybrechts et al., 1991; Huybrechts, 2002; Greve, 1997; Greve et al., 2011; Nielsen et al., 2018). This assumes a fixed spatial pattern through time, which is unlikely to be valid. Recently, Buizert et al. (2018) used the average of the three best-understood Greenland ice-core records to adjust the results of a transient climate-model simulation (the transient climate evolution experiment, TraCE-21ka; Liu et al., 2009; He et al., 2013). This approach allows for possible changes in spatial relationships, but focuses on ice cores in central and northern Greenland and provides no information on precipitation. Other attempts to incorporate more proxy data have been limited to short time periods (e.g., Simpson et al., 2009; Lecavalier et al., 2014).

In this study we apply paleoclimate data assimilation to obtain a new, spatially-complete reconstruction of Greenland temperature and precipitation. We focus on the last 20,000 years, which includes the end of the last glacial period, the glacial to interglacial transition, and the Holocene thermal maximum (HTM), when temperatures at the Greenland ice sheet summit reached 1-2 °C warmer than present (Cuffey and Clow, 1997; Dahl-Jensen et al., 1998). The climate history, and the corresponding changes in the size of the ice sheet, are well-documented over this time period (e.g., Kaufman et al., 2004; Young and Briner, 2015).

Paleoclimate data assimilation combines spatial information from a climate-model simulation and temporal data from proxy records to produce a climate reanalysis, where the

term is taken from the modern climate reanalysis methods on which the data assimilation method is based (e.g., Kalnay et al., 1996). We adapt the paleoclimate data assimilation framework developed by Hakim et al. (2016), who reconstructed annual two-meter air temperature and 500 hPa geopotential height over the last millennium using a global network of temperature and precipitation-sensitive proxy records. Here, we use oxygen isotopes of ice and layer thickness from ice cores to reconstruct temperature and precipitation, respectively. We choose these proxies for their high temporal resolution, direct relationships to climate over the ice sheet, and availability from multiple ice cores. For the climate-model simulation, we use TraCE-21ka (Liu et al., 2009; He et al., 2013), which was run with the Community Climate System Model version 3 (CCSM3) to simulate the last 22,000 years. We compare the resulting reanalysis to previously-published climate reconstructions (Sections 2.3.1, 2.4.2, and 2.4.3), and assess the precipitation-temperature relationship (Section 2.4.1). We evaluate the reanalysis with independent proxy records and sensitivity tests (Sections 2.3.2 and 2.3.3).

2.2 Methods

Our paleoclimate reconstruction method assimilates oxygen isotope ratios and accumulation from ice cores with a transient climate-model simulation to reconstruct the last 20,000 years of Greenland temperature and precipitation. In the following subsections we discuss the ice-core data, the climate-model simulation, and the details of our paleoclimate data assimilation approach.

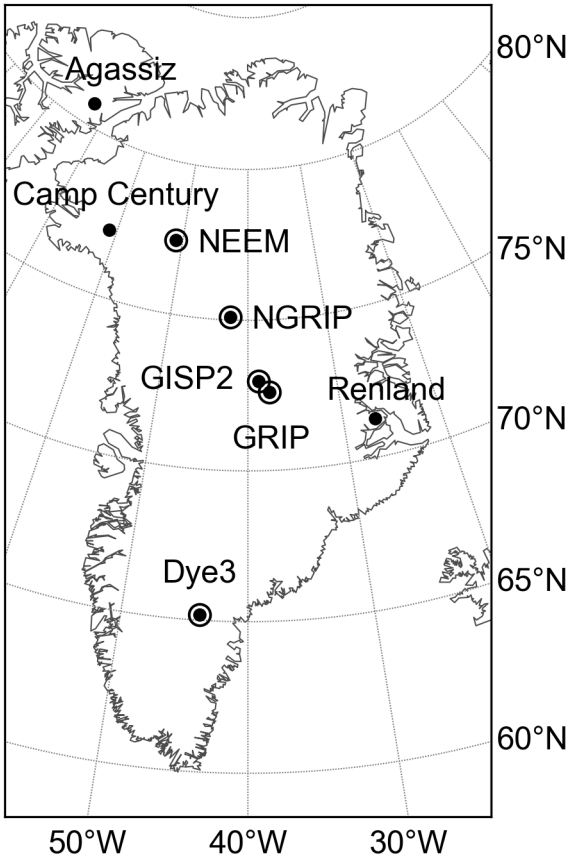

Figure 2.1: Locations of the ice-core sites referenced in this study. We use oxygen isotope (δ^{18}O) records from all eight sites and accumulation records from the five circled sites.

Table 2.1: Metadata for the water isotope (δ^{18}O) and accumulation (accum) records referenced in this study. "NBI" refers to the Niels Bohr Institute data access site (http://www.iceandclimate.nbi.ku.dk/data/) and "Pangaea" refers to the Pangaea data access site (https://www.pangaea.de/). Latitude and longitude are in units of decimal degrees (dd) and dates are in thousands of years before 1950 CE (ka). [1] Vinther et al. (2009), [2] NEEM Community Members (2013), [3] Schüpbach et al. (2018), [4] personal comm. Bo Vinther, [5] Rasmussen et al. (2013), [6] Andersen et al. (2004), [7] Vinther et al. (2006), [8] Rasmussen et al. (2006), [9] Andersen et al. (2006), [10] Svensson et al. (2006), [11] Grootes and Stuiver (1997), [12] Stuiver and Grootes (2000), [13] Cuffey and Clow (1997), [14] Johnsen et al. (1997), [15] Dansgaard et al. (1982), [16] this study.

Ice core name	**Lat. (dd)**	**Long. (dd)**	**Variables**	**Oldest (ka)**	**Youngest (ka)**	**Source**	**Citations**
Agassiz	80.7	286.9	δ^{18}O	11.64	−0.02	NBI	1
Camp Century	77.18	298.88	δ^{18}O	11.64	−0.02	NBI	1
NEEM	77.45	308.94	δ^{18}O	>20	−0.0108	NBI	2, 3, 4
			accum	>20	−0.04	NBI	5
NGRIP	75.1	317.7	δ^{18}O	>20	−0.04	NBI	6
			accum	>20	−0.02	this study	7, 8, 9, 10
GISP2	72.97	321.2	δ^{18}O	>20	−0.04	NBI	11, 12
			accum	>20	−0.0375	Pangaea	13
GRIP	72.6	322.4	δ^{18}O	>20	−0.02	NBI	14
			accum	>20	−0.02	this study	7, 8, 9, 10
Renland	71.27	333.27	δ^{18}O	11.64	−0.02	NBI	1
Dye3	65.18	316.18	δ^{18}O	>20	−0.02	NBI	1, 15
			accum	11.64	0	this study	7, 8, 16

2.2.1 Ice-Core Data

We use proxy records from eight ice cores from the Greenland ice sheet and nearby ice caps (Figure 2.1, Table 2.1). As a proxy for temperature, we use previously-published measurements of oxygen isotope ratios from the ice, which we discuss using the conventional δ^{18}O nomenclature (Dansgaard, 1964). We note that while other proxies (such as borehole thermometry or δ^{15}N of N_2) have been used to produce temperature estimates (e.g., Cuffey et al., 1995; Dahl-Jensen et al., 1998; Severinghaus et al., 1998; Severinghaus and Brook, 1999), they are not available for many of the core locations; we instead rely on such data to obtain independent estimates of error in the δ^{18}O-temperature relationship (see Section 2.2.3) and as comparisons to our resulting reanalysis (see Section 2.3). The accumulation history has been estimated for five of these cores from layer thickness corrected for vertical ice-thinning due to dynamical strain in the ice sheet. We rely on previously-published accumulation histories for the GISP2 and NEEM cores (Cuffey and Clow, 1997; Rasmussen et al., 2013), and we estimate accumulation for the Dye3, GRIP, and NGRIP cores using available layer-thickness data and simple ice-thinning calculations (see below and Section A.2). We do not use accumulation records from the Agassiz, Camp Century, or Renland cores because the ice-thinning history at these sites is not adequately constrained. Most of the ice-core data are available at 50 year or higher resolution and have been synchronized to a common depth-age scale (the Greenland ice core chronology 2005, GICC05; Andersen et al., 2006; Rasmussen et al., 2006; Svensson et al., 2006; Vinther et al., 2006, 2008). All of these ice-core records extend from the beginning of the Holocene to the present. Five δ^{18}O and four accumulation records also include the last glacial period. To evaluate the impact of the differing lengths of these records, we produce a sensitivity reanalysis for which we assimilate just the fixed proxy-network (i.e., only those data that span the full reanalysis time period, the last 20,000 years).

To extract the accumulation signal from layer-thickness, the layers must be destrained using assumptions about the history of ice flow. For the Dye3, GRIP, and NGRIP cores,

we use a one-dimensional ice-flow model (Dansgaard and Johnsen, 1969) to calculate the cumulative vertical strain the layers have experienced at each core site. The Dansgaard-Johnsen model requires specifying the vertical velocity at the surface and a kink height which determines the shape of the vertical velocity profile. The velocity profile below the kink height approximates the influence of greater deformation rates in deeper ice due to increased deviatoric stress and warmer ice temperature. For sites at the pressure-melting point at the bed, such as NGRIP, we also implement the basal melt-rate (e.g., Dahl-Jensen et al., 2003). Previous work on many of the Greenland ice cores has estimated cumulative vertical thinning assuming that the accumulation history scales with δ^{18}O and then found optimal parameter values by comparing the modeled and measured depth-age relationships (Dahl-Jensen et al., 1993, 2003; Rasmussen et al., 2014). Here, we wish to maintain independent determinations of the δ^{18}O and accumulation proxy records. To do this, we select reasonable ice-flow parameters independently, based on the glaciological setting of each site; specifically, we use kink-height values of 0.1-0.2 for flank flow and 0.4 for ice flow near ice divides where the deviatoric stress is low (Raymond, 1983; Conway et al., 1999). Where available, we use published values or kink-height values that result in a good match to published accumulation records (Dahl-Jensen et al., 2003; Gkinis et al., 2014). Based on this range of plausible ice-flow parameters, we develop three scenarios for each site: "low", "moderate", and "high", where the names reflect the relative magnitude of accumulation in the glacial and early Holocene. We assimilate the intermediate-value ("moderate") accumulation records to produce our main precipitation reanalysis, while we assimilate the high and low accumulation records into high and low sensitivity scenarios, respectively, to provide a conservative estimate of uncertainty. Descriptions of the rationale for the parameter choices at each site are given in Section A.2. Our method to estimate accumulation should be most accurate for the interior ice cores (i.e., GISP2, GRIP, NEEM, NGRIP); these sites are thicker and have lower accumulation rates such that layers of the same age have experienced less cumulative strain than for the more coastal cores (i.e., Agassiz, Camp Century, and Renland). We do not attempt to reconstruct accumulation from these coastal cores because the layers cannot be

destrained with sufficient accuracy. Dye3 suffers from the same challenges; however, it is the only ice core with long-term climate data south of 70°N (Figure 2.1). Thus, we include the Holocene Dye3 accumulation rates despite the greater uncertainty relative to the interior cores.

Because records from the Dye3 ice core are our only source of information in southern Greenland, we take the following steps to increase the data available for assimilation. The Dye3 record has not been previously assigned a depth-age scale beyond 11.7 ka (throughout this paper, ka refers to thousands of years before 1950 CE). We extend the depth-age scale to 20 ka to take advantage of the glacial portion of the δ^{18}O record. To do this, we match the δ^{18}O record from Dye3 to the δ^{18}O record from NGRIP using the cross-correlation maximization procedure from Huybers and Wunsch (2004) (Section A.3). We interpolate the glacial δ^{18}O record from Dye3 (which, as measured, has an average resolution of only 85 years) to the same 50 year resolution used for our other ice-core records. Extension of the Dye3 depth-age scale also provides a layer-thickness record from 20 ka to present; however, we do not use accumulation data from Dye3 for the period 20-11.7 ka because the low resolution impedes our ability to estimate accumulation variations from layer thickness. Using this depth-age scale extension for Dye3 may introduce error that is difficult to quantify; however, we find that including Dye3 has an important impact on the resulting reanalysis of southern Greenland climate (Section A.4).

Where possible, we account for non-local effects on the ice-core records. The global-mean δ^{18}O of seawater fluctuates with global ice-volume, while on the regional scale, horizontal advection brings ice from other elevations and latitudes. We correct for changes in the oxygen-isotope composition of seawater following the methods of Stenni et al. (2010), using the benthic foraminifera dataset from Bintanja et al. (2005). For ice cores in regions of high horizontal advection, we correct for elevation and latitude differences between the site of snow deposition and the ice-core site. Following the methods from NEEM Community Members (2013), we apply corrections for advection-caused elevation changes in the δ^{18}O records from Camp Century, Dye3, and NEEM and for advection-caused latitude changes in

the δ^{18}O record from NEEM (Vinther et al., 2009; NEEM Community Members, 2013). We do not correct the accumulation records for advection from upstream because the elevation-accumulation relationship is complicated by the prevailing wind direction (Roe and Lindzen, 2001) and the thinning function uncertainties are likely to be larger than the effects of ice advection. We also do not correct δ^{18}O or accumulation for changing elevation at the ice-core site; our goal is to reconstruct conditions at the surface, rather than at a constant reference elevation. We take the anomaly of each corrected δ^{18}O record and the ratio of each accumulation record relative to the mean of all data in the record that falls within the time period 1850-2000 CE. We then average each record to 50 year resolution, the lowest resolution in these records (with the exception of δ^{18}O from the glacial period in the Dye3 core). It is these corrected, averaged records that we use in the data assimilation (Figures 2.2 and 2.3).

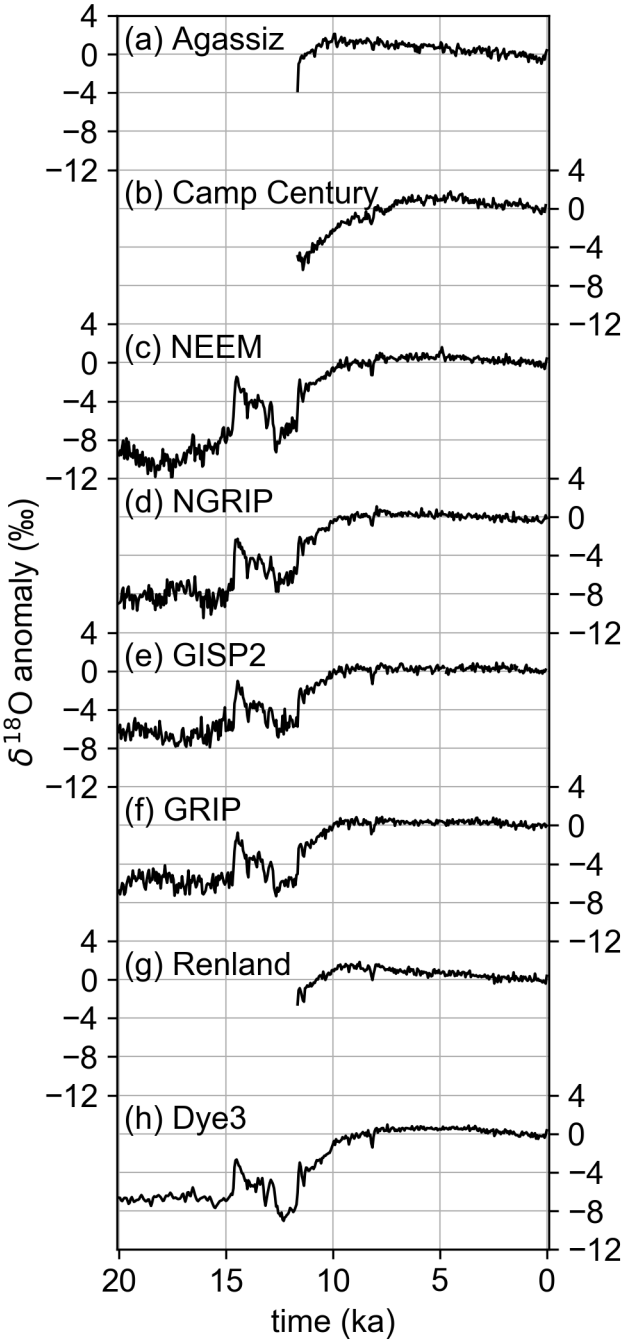

Figure 2.2: δ^{18}O records assimilated into the temperature reconstruction. Records are shown as anomalies relative to the mean of 1850-2000 CE and are ordered top to bottom from northernmost to southernmost. Ice-core site names are given above each record.

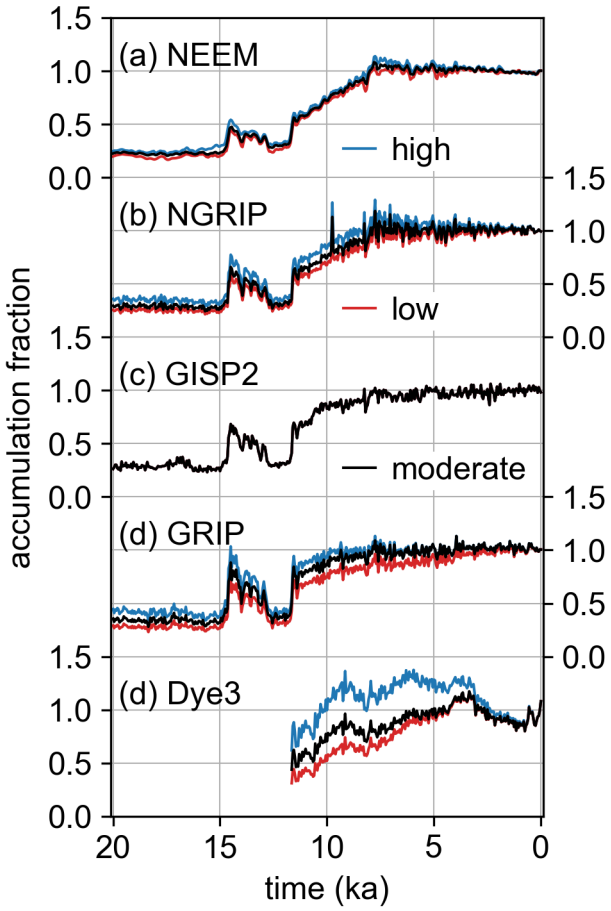

Figure 2.3: Accumulation records assimilated to reconstruct precipitation for the main reanalysis and two sensitivity scenarios. Records are shown as fractions relative to the mean of 1850-2000 CE and are ordered top to bottom from northernmost to southernmost. Black lines are the moderate records which are included in the main precipitation reanalysis, red lines are the low records which are included in the low sensitivity scenario, and blue lines are the high records which are included in the high sensitivity scenario. Note that we use the same GISP2 accumulation record for the main, high, and low scenarios. Ice-core site names are given above each set of records.

2.2.2 Climate-Model Simulation

We use TraCE-21ka, a simulation of the last 22,000 years of climate (22 ka to -.04 ka), which was run using the fully-coupled CCSM3 at T31 resolution (approximately 3.75 degrees horizontally) with transient ice-sheet, orbital, greenhouse gas, and meltwater flux forcings

(Liu et al., 2009, 2012; He et al., 2013). For paleoclimate data assimilation, it is important that the climate simulation capture a range of possible climate states over the time period of interest. By design, TraCE-21ka captures the major glacial-to-Holocene temperature changes, as well as some of the short-term, rapid climate changes, such as the Blling-Allerd transition (Liu et al., 2009). Many higher-resolution climate simulations are transient only over the last millennium (e.g., PAGES 2k-PMIP3 group, 2015) or provide a snapshot of a certain time, such as Last Glacial Maximum or the mid Holocene (e.g., Harrison et al., 2014). Individually, these millennial-length simulations have too little variability to capture the range of climate states across the glacial-interglacial transition. If combined, the biases in each simulation would need to be individually addressed, which is beyond the scope of this study.

From TraCE-21ka, we use two-meter air temperature for temperature (T) and the sum of large-scale stable precipitation and convective precipitation for precipitation (P). To correct for model bias in TraCE-21ka, we assume that the bias is stationary in time and apply the delta-change method (Teutschbein and Seibert, 2012) by taking the anomaly of temperature and the fraction of precipitation relative to the mean of our reference period (1850-2000 CE). An assumption of a stationary model bias is required because, with a small number of proxy records, we cannot afford to subsample them for the purposes of bias correction, data assimilation, and evaluation. After the bias correction, we average the TraCE-21ka variables (which originally have monthly resolution) to 50 year resolution, as we did for the ice-core records. In this process, we average 50 consecutive years (600 months) such that no year (or month) is used in more than one 50 year average. This averaging results in 440 time steps spaced 50 years apart.

TraCE-21ka includes changes in orbital forcing, which contribute to changes in the seasonality of temperature and precipitation. The strength of these seasonal cycles influences the mean-annual relationship between δ^{18}O and temperature (Steig et al., 1994; Werner et al., 2000; Krinner and Werner, 2003). TraCE-21ka consistently shows stronger temperature and precipitation seasonality in the glacial (20 to 15 ka) than in the Holocene (5 to 0

ka) at each of the eight ice-core sites considered in this study (Figure A.3). Relative to the annual mean, the glacial had warmer and wetter summers and colder and drier winters. The Holocene also shows such a seasonal cycle; however, there is a smaller difference between the summers and winters. Any seasonal signal with wetter summers than winters will bias the δ^{18}O towards summer values. According to TraCE-21ka, this effect is amplified in the glacial. As we discuss in Section 2.2.3, the particularly strong summer bias in the glacial affects the mean-annual δ^{18}O-temperature relationship in ways that are consistent with findings from borehole thermometry at the GISP2, GRIP, and Dye3 ice-core sites (Cuffey and Clow, 1997; Jouzel et al., 1997).

In addition to a change in the strength of the seasonal cycle, TraCE-21ka shows a temporal shift, with summer temperature and precipitation peaking earlier in the glacial (around June and July) than in the Holocene (from July to September) (Figure A.3). In the glacial, both variables peak around June and July, with only two exceptions: precipitation peaks in August at the Renland and Dye3 ice-core sites. In contrast, Holocene temperature peaks slightly later, in July, while precipitation peaks even later, in August and occasionally September. Both variables and both time periods show winter minimums in February, again with the two exceptions of Renland and Dye3, which show later precipitation minimums. In this study, the timing of the seasonal peaks is relevant because it affects the precipitation-weighted temperature, defined in Eq. 2.7.

TraCE-21ka also includes prescribed transient ice sheets as a boundary condition. The transience is important for capturing the influence of elevation change on the ice-core records; however, the low horizontal resolution of TraCE-21ka leads to difficulties in capturing elevation changes at the edges of the ice sheet, in southern Greenland, and at coastal ice caps. In addition, the ice sheets in TraCE-21ka are independent of climate, updated only every 500 years during the simulation, and taken from ICE-5G (Peltier, 2004), a now outdated ice-sheet reconstruction (Roy and Peltier, 2018).

2.2.3 Paleoclimate Data Assimilation

To combine the ice-core and climate-model data, we use an offline data assimilation method similar to that described in Hakim et al. (2016). If no covariance localization is used, as in this study, this method can be summed up as a linear combination of randomly-selected model states that are weighted according to new information provided by the proxy records. "Offline" refers to the absence of a forecast model that evolves the climate state between assimilation time steps. The offline method is appropriate when model predictive-skill is small given the assimilation time step (Hakim et al., 2016, and references therein). Model predictive-skill is generally poor on decadal to longer timescales (Latif and Keenlyside, 2011, and references therein) except possibly during times of strong forcing, such as the Bølling-Allerød (14.7-12.7 ka) and the Younger Dryas (12.7-11.7 ka) (Hawkins and Sutton, 2009). Because each of our time steps is an average over 50 years, as dictated by the resolution to which we average the proxy records, the offline method is appropriate except possibly during these large-forcing events. For these events, an online method may be appropriate (assuming that the models correctly capture both the forcing and the response); however, online ensemble data assimilation over glacial-interglacial cycles using a fully-coupled earth system model is impractical due to the computational cost and is beyond the scope of this study.

Our paleoclimate data assimilation framework uses ensembles for the initial (prior) and final (posterior) estimates of the climate state, providing a probabilistic framework for interpreting and evaluating the results. To compute the posterior ensemble, we apply the Kalman update equation (Whitaker and Hamill, 2002), which spreads new information gained from proxy records to all locations and variables in the prior ensemble:

$$\vec{x_a} = \vec{x_b} + \mathbf{K}(\vec{y} - \mathcal{H}(\vec{x_b})) \tag{2.1}$$

Bold lowercase letters are vectors, bold capital letters are matrices, and script capital letters are mapping functions. The posterior ensemble is $\vec{x_a}$, $\vec{x_b}$ is the prior ensemble, $\vec{y}$ is the proxy data, and $\mathcal{H}$ is the function that maps from the prior variables to the proxy variables. $\mathbf{K}$ is

the Kalman gain matrix:

$$\mathbf{K} = \mathbf{B}\mathbf{H}^T(\mathbf{H}\mathbf{B}\mathbf{H}^T + \mathbf{R})^{-1} \tag{2.2}$$

where ^{T} indicates a matrix transpose, $\mathbf{B}$ is the covariance matrix computed from the prior ensemble, $\mathbf{H}$ is the linearization of $\mathcal{H}$ about the mean value of the prior, and $\mathbf{R}$ is a diagonal matrix containing the error variance for each proxy record, the use of which requires an assumption that error covariances between proxy records are negligible.

To compute the new information gained from the proxy records, the prior ensemble must first be mapped into proxy space to get prior estimates of the proxy ($\mathcal{H}(\vec{x_b})$). This mapping ($\mathcal{H}$) is the proxy system model (PSM). Our PSM for the δ^{18}O-temperature relationship is a linear function and for accumulation is a direct comparison between ice-core-derived accumulation and precipitation from the prior. For these PSMs, both temperature and precipitation are interpolated from the climate-model grid to the geographic location of the ice core. These PSMs are detailed in Sections 2.2.3 and 2.2.3. Comparing the prior estimates of the proxy ($\mathcal{H}(\vec{x_b})$) to the proxy data ($\vec{y}$) yields the innovation ($\vec{y} - \mathcal{H}(\vec{x_b})$), the new information gained from the proxy records.

The Kalman gain ($\mathbf{K}$, equation 2.2) weights the innovation by the relative magnitude of the ensemble covariance of the prior estimates of the proxy ($\mathbf{H}\mathbf{B}\mathbf{H}^T$), and the error covariance of the proxy records ($\mathbf{R}$). The Kalman gain spreads the weighted innovation to all locations and variables in the prior ensemble, using the covariance structure ($\mathbf{B}\mathbf{H}^T$) from the prior ensemble.

The prior ensemble is an initial estimate of possible climate states, which we form using 100 randomly-chosen 50 year averages from the TraCE-21ka simulation. States from both the glacial and the Holocene make up a prior ensemble. The same prior is used for all time steps in the reconstruction, leading to a prior that is constant in time. For a longer discussion on the reasoning behind our choice to use a constant prior, please refer to Appendix A, Section A.1. Proxy records are assimilated into the prior using equation 2.1, which produces the posterior ensemble, a new estimate of possible climate states. We assimilate δ^{18}O to reconstruct temperature and separately assimilate accumulation to reconstruct precipitation.

This approach maintains independence between temperature and precipitation, which avoids imposing linearity and stationarity on the relationship between these two variables. As Cuffey and Clow (1997) show, not only is this relationship non-linear on long timescales but it is also not well-approximated by simple thermodynamic expectations. Separating these variables ensures that the relationship between temperature and precipitation is consistent with the empirical relationship between δ^{18}O and accumulation from ice cores, rather than being derived exclusively from the climate model.

We repeat the data assimilation process over multiple iterations, with each iteration using one of ten different 100-member prior ensembles and excluding one proxy record. Each of the ten prior ensembles is made up of a different random selection of 50 year averages from TraCE-21ka. Thus, each prior ensemble has a different variance and spatial covariance structure. Each proxy record is excluded from a total of ten iterations, where each of these iterations uses a different one of the ten prior options. Every iteration is uniquely identifiable by which prior ensemble is used and which proxy record is excluded. For a reanalysis, the total number of iterations is thus ten times the number of proxy records, such that for temperature we have 80 iterations and for precipitation we have 50 iterations. A reanalysis is a compilation of the 100-member posterior ensembles from these iterations, resulting in a temperature reanalysis having 8,000 ensemble members and a precipitation reanalysis having 5,000 ensemble members.

The proxy record that is excluded from an iteration is independent of that iteration's posterior ensemble, such that we can evaluate the posterior against this record. With our PSMs, we convert the posterior ensemble into predictions of the independent record using the mapping $\mathcal{H}$ and compare these predictions to the record along the time axis. We use four skill metrics to evaluate different aspects of the predictions. The correlation coefficient (corr; equation 2.3) measures the relative timing of signals in the predictions and the proxy record:

$$corr = \frac{1}{n-1} \sum_{i=1}^{n} \left(\frac{(y_i - \bar{y})(v_i - \bar{v})}{\sigma_y \sigma_v} \right) \tag{2.3}$$

where v is the ensemble mean of the predicted values, y is the proxy record value, an overbar indicates a time mean, n is the number of time steps, and σ is the standard deviation of the variable in the subscript. The coefficient of efficiency (CE; equation 2.4) (Nash and Sutcliffe, 1970) is affected by signal timing as well as signal amplitude and mean bias:

$$CE = 1 - \frac{\Sigma_{i=1}^{n}(v_i - y_i)^2}{\Sigma_{i=1}^{n}(y_i - \bar{y})^2} \tag{2.4}$$

The root mean squared error (RMSE; equation 2.5) gives an intuitive sense for the magnitude of the differences between the predictions and proxy record:

$$RMSE = \left(\frac{1}{n}\sum_{i=1}^{n}(y_i - v_i)^2\right)^{1/2} \tag{2.5}$$

The ensemble calibration ratio (ECR; Eq. 2.6) indicates whether the ensemble has enough spread (uncertainty) given the error in the ensemble mean (e.g., Houtekamer et al., 2005):

$$ECR = \frac{1}{n}\sum_{i=1}^{n}\left(\frac{(y_i - v_i)^2}{var(\vec{v_i}) + r}\right) \tag{2.6}$$

where $\vec{v}$ is a vector of the ensemble members of the predicted values, r is the error variance for the proxy record (y), and var indicates the variance. Accordingly, if the ensemble variance is appropriate for the amount of error, then the ensemble calibration ratio is near unity.

We compute all four skill metrics for both the posterior and prior ensembles, which shows whether assimilation of proxy records results in an improved estimate of the climate state over our initial estimate. We define improvement as correlation coefficient closer to 1, CE closer to 1, RMSE closer to 0, and ensemble calibration ratio closer to 1. We anticipate that our reanalysis will show improvement over the prior because the prior is constant in time and contains no information about temporal climate variations; however, improvement is not gauranteed, especially if proxy records contain highly-localized climate signals or if the prior covariance structure is unable to appropriately spread information from the proxy sites to other locations. For further comparison, we additionally compute the correlation coefficient, CE, and RMSE between the TraCE-21ka simulation and the proxy records.

We evaluate results over three time periods: 1) the full overlap between the reanalysis time period and the proxy record, 2) a time representative of the glacial, 20-15 ka, and 3) a time representative of the Holocene, 8-3 ka. Some proxy records overlap the full reanalysis period, 20-0 ka, while others overlap just the Holocene, 11.7-0 ka. The skill metrics computed for these two groups should be considered separately.

To remove mean bias from temperature, we subtract out the reference-period mean. For precipitation, we divide by the reference-period mean. It is these bias-corrected results that are referred to unless noted otherwise.

Proxy System Model: $\delta^{18}O$

The isotopic composition of precipitation, as recorded in ice cores, is highly correlated with temperature at the time and location of deposition, but is also sensitive to conditions at the moisture source region (i.e. sea surface temperature and relative humidity at the ocean surface; e.g., Johnsen et al., 1989). Moisture-source conditions primarily affect the deuterium excess, which we do not use here, and the influence on δ^{18}O is comparatively weak (e.g., Armengaud et al., 1998). For our δ^{18}O PSM, we use a linear relationship with temperature at the ice-core drill site (T_{site}) that has a slope of 0.67 ± 0.02 ‰ $^{\circ}C^{-1}$, which was calibrated using modern, spatial data (Johnsen et al., 1989). It is well known that this modern, spatially-derived slope does not necessarily apply to temporal δ^{18}O-T_{site} relationships, which have effective slopes that are time, frequency, and location dependent. Temporal changes in precipitation seasonality, inversion-layer thickness, and source region conditions introduce nonlinearity into the effective δ^{18}O-T_{site} relationship (e.g., Jouzel et al., 1997; Pausata and Löfverström, 2015). Diffusion in the firn column also affects this relationship, but it is negligible for annual and longer timescales at the locations of the ice cores we use (Cuffey and Steig, 1998). Borehole thermometry at the GISP2 and GRIP sites show that for the low-frequency changes associated with the last glacial-interglacial transition, the temporal slope is less than half the modern, spatial slope (Cuffey and Clow, 1997; Jouzel et al., 1997). Numerous studies have suggested that precipitation seasonality is the largest source

of nonlinearity in the δ^{18}O-T_{site} relationship (e.g., Steig et al., 1994; Pausata and Löfverström, 2015); changes in precipitation seasonality are thought to be the primary reason that the effective δ^{18}O-T_{site} relationship for the glacial-interglacial transition has such a low slope (Werner et al., 2000; Gierz et al., 2017; Cauquoin et al., 2019).

We rely on TraCE-21ka to estimate the site-specific effects of precipitation seasonality on the δ^{18}O-T_{site} relationship. Site-specific effects can also be estimated using independent temperature reconstructions, e.g. from borehole thermometry or δ^{15}N of N_2 measurements; however, such independent reconstructions for the last 20,000 years exist only for a few of the long ice-core records, GISP2, GRIP, and NGRIP (Buizert et al., 2018; Dahl-Jensen et al., 1998; Gkinis et al., 2014), limiting the utility of such records to capture the spatial variability of the δ^{18}O-T_{site} relationship across Greenland .

To incorporate estimates of the site-specific effects of precipitation seasonality from TraCE-21ka, we adjust the linear δ^{18}O PSM by replacing T_{site} with T^*_{site}, the precipitation-weighted temperature at the model grid-cell closest to the ice-core drill site. We compute T^* across Greenland using T and P from TraCE-21ka (see Figure A.4 for a visual comparison of T and T^* at the GISP2 ice-core site):

$$T^* = \sum_{i=1}^{n=12} \left(T_{mon} \frac{P_{mon}}{P_{ann}} \right) \tag{2.7}$$

With T^*_{site} in our PSM, we find that the δ^{18}O-T_{site} slope is spatially variable (e.g., Figure A.5), ranging between 0.42 and 0.66 ‰ °C^{-1} at the ice-core sites (Table A.1), and tending to be less than the modern spatial relationship of 0.67 ‰ °C^{-1} at most locations around Greenland. Due to the data assimilation method outlined above, these slopes vary both in space and across iterations, the latter being due to the varying prior ensembles. These slopes do not vary in time in the prior, but they do in the posterior (note that δ^{18}O-T_{site} slopes mentioned throughout this paper refer to the prior ensemble). By using ten different prior ensembles, we capture the uncertainty in the δ^{18}O-temperature relationship from variations in the precipitation seasonality. These TraCE-21ka-derived estimates lie within the range of slopes estimated for sites around Greenland for a variety of time periods (Table A.1).

Differences seen in Table A.1 reflect both the different methods used and the time period considered. Some estimates, such as Guillevic et al. (2013) and Buizert et al. (2014) are for abrupt transitions, such as Dansgaard-Oeschger events, while others find mean slopes over longer periods of time, such as Kindler et al. (2014) and this investigation.

To evaluate the sensitivity of our results to the choice of PSM, we produce four other reconstructions (S1-S4). The S1 scenario uses the PSM, $\delta^{18}\mathrm{O}= 0.67T_{site}$, which is the modern (high-frequency) relationship and does not account for precipitation seasonality. The S2 scenario uses $\delta^{18}\mathrm{O}= 0.5T_{site}$, the mean of the high-frequency and low-frequency temporal slopes. The S3 scenario uses $\delta^{18}\mathrm{O}= 0.335T_{site}$, which is similar to published estimates of the glacial-interglacial temporal slope (half the high-frequency slope) (Cuffey and Clow, 1997; Jouzel et al., 1997). By lowering the slope in the S2 and S3 scenarios, we implicitly account for precipitation seasonality; however, in these scenarios and S1, the $\delta^{18}\mathrm{O}$-T_{site} relationship is spatially uniform, whereas it is spatially variable in the main reanalysis because we include the spatial pattern of precipitation seasonality. The S4 scenario uses the same PSM as in the main reanalysis, $\delta^{18}\mathrm{O}= 0.67T^{*}_{site}$, but we adjust the strength of the precipitation seasonality in TraCE-21ka such that the average $\delta^{18}\mathrm{O}$-T_{site} slope around Greenland is approximately 0.335 ‰ $^{\circ}\mathrm{C}^{-1}$. The S4 scenario thus has the same spatially-variable $\delta^{18}\mathrm{O}$-T_{site} relationship as in the main reanalysis, but a greater influence of precipitation seasonality.

These sensitivity tests are equivalent to testing different assumptions about the $\delta^{18}\mathrm{O}$-T_{site} relationship. The availability of a 20,000 year-long isotope-enabled climate simulation would allow us to determine this relationship from model physics, which incorporate a variety of processes that can affect water isotopes, including precipitation seasonality.

Proxy System Model: Accumulation

Accumulation is closely related to total precipitation at our ice-core sites, which have limited surface melting and evaporation. Simulations from the regional climate model HIRHAM5 show that for modern climate at the GISP2, GRIP, NEEM, and NGRIP ice-core sites, surface mass balance, snowfall, and precipitation are all within 1.6 cm water equivalent (w.e.) when

averaged over the years 1989 to 2012 CE (Langen et al., 2015, 2017). For this reason, and because TraCE-21ka lacks process-based ablation variables, our PSM is a direct-comparison between ice-core accumulation and simulated precipitation at the model grid-cell closest to the ice-core site.

This direct-comparison PSM may be an incomplete model of the accumulation-precipitation relationship at the Dye3 ice-core site; regional climate simulations show that modern surface mass balance is lower than precipitation due to melt rates that average 84 cm w.e. year^{-1}. Significant melt rates would cause the spatial covariance structure of accumulation across these sites to differ from that of precipitation; however, both models and observations lack the necessary variables or duration to show the extent to which this difference exists for 50 year timescales through the last glacial-interglacial cycle. We emphasize that we use relative, rather than absolute changes in the data assimilation, to account for the mean bias between precipitation and accumulation.

Proxy Error Variance Estimation

In the Kalman filter (equation 2.1), the diagonal elements of $\mathbf{R}$ contain the error variance of each proxy record, which includes how we model the proxy (the PSM). We compute representative error variances for δ^{18}O and accumulation, and apply them to all records and time slices. We do not include error associated with corrections applied to the ice-core data (Section 2.2.1) or associated with the accumulation PSM (Section 2.2.3) because we cannot characterize the statistical properties of these errors.

A universal, but typically small, error source is from the measurement of proxies. For δ^{18}O, measurement error is equivalent to laboratory precision. We compute a representative measurement error from the GISP2 ice core, for which a single measurement of δ^{18}O has a laboratory precision (variance) of 0.024 ‰^{2} (Stuiver and Grootes, 2000). Assuming independent error and annual measurements, the 50 year average error variance reduces to 0.0034 ‰^{2}, which is insignificant compared to other sources of error. For accumulation, the measurement error is from the measurement of layer thickness, which is related to the

error in annual-layer counts per unit depth. Again, we assume GISP2 is a representative core and estimate the layer-thickness error from Table 3 in Alley et al. (1997), which provides repeat annual-layer counts for several depth intervals. From this table, we find the standard deviation of counted years in each depth interval, divide by the average number of years, average across all depth intervals, and square the result. This computation results in a layer-thickness error variance of 0.0015, a unitless number due to our use of fractional accumulation records.

Another source of error is the extent to which a model grid-cell may misrepresent a point proxy-measurement. In the innovation, there is an implicit assumption that the proxy ($\vec{y}$) and the prior estimate of the proxy ($\mathcal{H}(\vec{x_b})$) are representative of the same processes. However, an ice core is about 100 cm^2, an area that is affected by processes at all scales, from regional change to local, sub-meter-scale topography, while a model grid-cell in TraCE-21ka can cover tens of thousands of square kilometers, an area that is affected by only the largest scales, from global to regional. Thus, there is an inherent inability of the prior to represent local processes at the ice-core site, which we refer to as the spatial representation error. To estimate this error, we compute the variance of the local noise (e.g., Reeh and Fisher, 1983) using the GISP2 and GRIP ice-core records, which are located about 30 km apart within the same model grid cell. For δ^{18}O, our estimate is 0.21 ‰^{2} which is about half the value determined by Fisher et al. (1985) at several locations around Greenland. Our estimate is relatively conservative, considering that we are using 50 year averages rather than annual averages as in Fisher et al. (1985). For accumulation, we estimate a spatial representation error variance of 0.0023 using the same method as for δ^{18}O.

A third source of error is the extent to which the δ^{18}O PSM may be an inaccurate model of the δ^{18}O-T_{site} relationship. The less accurate the PSM, the less weight that should be given to the innovation. We estimate PSM error variance by calculating the mean squared error (MSE) between a δ^{18}O record and an independent temperature record mapped to δ^{18}O using the PSM, $\delta^{18}\text{O} = 0.67 T_{site}$. We use independent datasets taken from the GISP2 ice core: the δ^{18}O record and three δ^{15}N-derived temperature estimates for the Holocene, a

mean estimate and the two-standard-deviation uncertainty bounds (Kobashi et al., 2017). From these datasets, we estimate three PSM error variances that range from 0.56 to 1.1 ‰^{2}, from which we choose the largest.

For the assimilation of each δ^{18}O record, we use an estimated total error variance of 1.3 ‰^{2}, which is a sum of the measurement, spatial representation, and PSM error variances. For the assimilation of each accumulation record, we use an estimated total error variance of 0.0038, which is a sum of the measurement and spatial representation error variances.

2.3 Results

2.3.1 Overview

Through the assimilation of ice-core data with a prior ensemble that is constant in time, we produce a spatially-complete, mean-annual Greenland temperature and precipitation reanalysis at 50 year resolution (Figures 2.4 and 2.5). Here we focus on results for the late glacial and the Holocene thermal maximum (HTM).

In our reanalysis, late glacial (20-15 ka) mean-temperature anomalies range from about −20 °C in northern Greenland to less than −10 °C in southern Greenland (Figure 2.4c). At the GRIP and GISP2 ice-core sites, the reanalysis has a −14 °C anomaly with a standard deviation of 2 °C. This is in excellent agreement with the mean-temperature anomaly of −14 °C for the same period at the GISP2 site, which was derived from δ^{18}O calibrated with borehole thermometry (Cuffey et al., 1995; Cuffey and Clow, 1997). Also in agreement with borehole thermometry, this period is warmer than the Last Glacial Maximum (Dahl-Jensen et al., 1993; Cuffey and Clow, 1997). Average late-glacial precipitation in the reanalysis ranges from a third to half of modern with the highest values on the coasts around southern Greenland (Figure 2.4d).

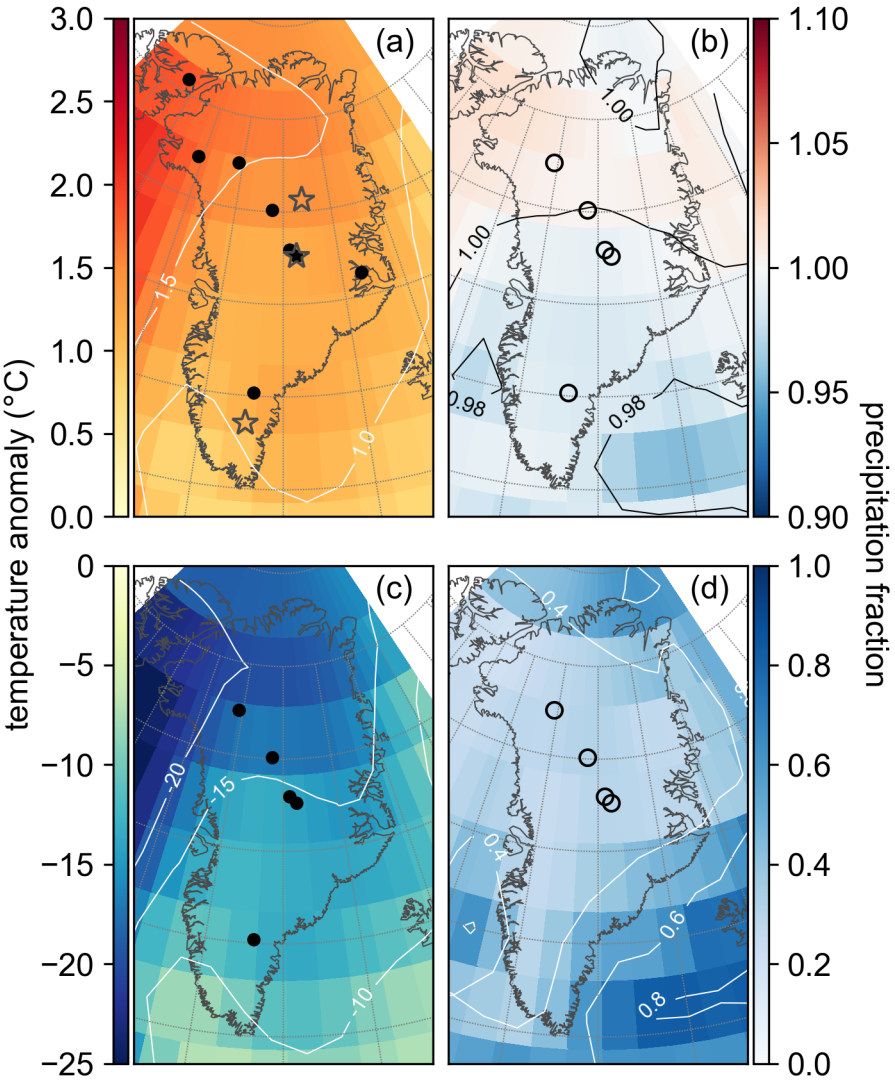

Figure 2.4: Spatial pattern of the reanalysis mean for temperature (panels (a), (c)) and precipitation (panels (b), (d)). (a) and (b) are averaged over 1,000 years around the peak warmth in the Holocene, 5.5-4.5 ka, while (c) and (d) are averaged over 5,000 years in the late glacial, 20-15 ka. Anomalies and fractions are with respect to the mean of 1850-2000 CE. Points show ice-core locations used for each reanalysis with closed circles indicating δ^{18}O records and open circles indicating accumulation records. Grey stars show the locations of the EGRIP ice-core site, Summit, and South Dome, which are referenced in Figures 2.5 and 2.10.

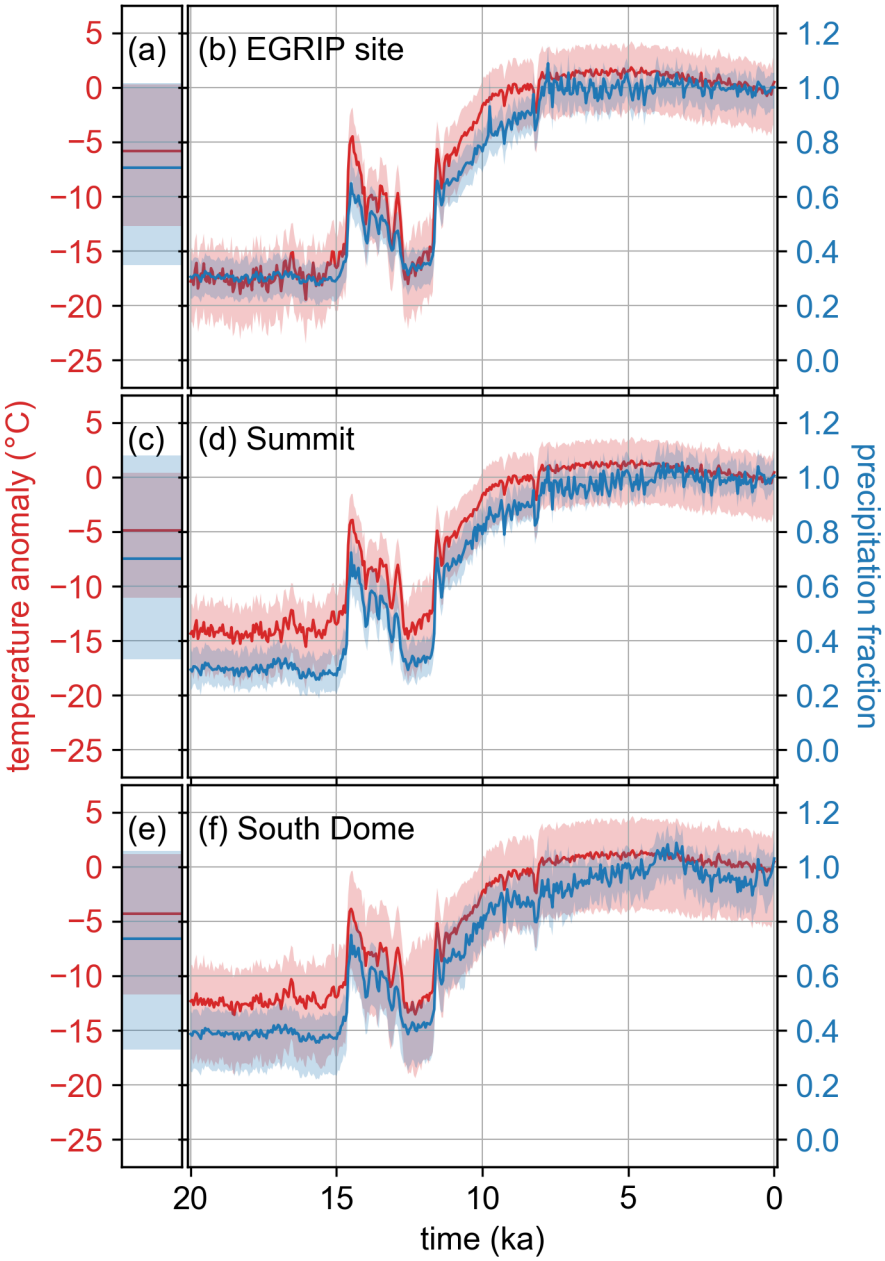

Figure 2.5: Time series of the prior (panels (a), (c) and (e)) and reanalysis (panels (b), (d) and (f)) ensemble mean and 5^{th} to 95^{th} percentile shading for temperature (red) and precipitation (blue) at three locations. Anomalies and fractions are with respect to the mean of 1850-2000 CE. (a) and (b) show these time series for the location closest to the EGRIP ice-core site, (c) and (d) show for the location closest to Summit, and (e) and (f) show for the location closest to South Dome. These locations are ordered from northernmost (top) to southernmost (bottom) and are shown on a map in Figure 2.4.

Our reanalysis shows warmest temperatures occurred across Greenland between 7 and 3 ka, reaching a temperature maximum around 5 ka (Figure 2.5). Although this timing tends to be later than many estimates of the HTM, it lies within the ranges reported in the literature; for example, a summary of proxy records from around Greenland shows peak warmth usually occurring around 9-5 ka, but also as early as 10.8 ka and as late as 3 ka (Kaufman et al., 2004). Borehole thermometry shows that temperatures peaked around 6-7.7 ka at Summit and 4.5 ka at the Dye3 ice-core site (Cuffey and Clow, 1997; Dahl-Jensen et al., 1998; Kaufman et al., 2004). Temperature estimates from δ^{15}N of N_2 show an earlier HTM peak at Summit around 8 ka (Kobashi et al., 2017). In northwest Greenland, δ^{18}O measurements from lake sediments show the HTM starting before 7.7 ka and ending around 6 ka (Lasher et al., 2017), while chironomid assemblages show peak warmth around 10-8 ka (McFarlin et al., 2018).

Mean-annual HTM temperature anomalies in our reanalysis range from nearly +2 °C in northern Greenland to about +1 °C in southern Greenland (Figure 2.4a). Similar to the late-glacial temperature anomalies, the pattern of the HTM is dominated by a north-south trend that has the greater temperature changes to the north, especially in northwest Greenland. While this spatial pattern agrees well with previous studies which have noted especially warm Holocene temperature anomalies in northwest Greenland (Lasher et al., 2017; Lecavalier et al., 2017; McFarlin et al., 2018), many estimates of HTM anomalies around Greenland are higher than our reanalysis indicates. Our low temperature estimates (compared to previous work) may be in part due to our reconstructing the annual mean rather than the summer mean; the greatest temperature anomalies in the HTM are thought to have occurred in the summer months and many proxies are more sensitive to summer than annual temperature (Kaufman et al., 2004). Importantly, in our reanalysis, the higher HTM temperatures do not translate to a marked increase in precipitation as would be expected from a thermodynamically-scaled relationship between temperature and precipitation. Instead, we find fractional precipitation within 2% of modern values (1.0±0.02) during the HTM (Figure 2.4b), with slightly higher-than-modern precipitation in central Greenland and slightly lower-

than-modern precipitation in northwestern Greenland.

2.3.2 Independent Proxy Evaluation

Here we evaluate our results against proxy records that are excluded from ten of the iterations that make up the temperature and precipitation reanalyses. For this evaluation, we use the raw results (without a mean-bias correction). We find, however, that the mean biases are small relative to climate changes over the last 20,000 years; there is little difference between our bias-corrected and uncorrected results and it is unlikely that the mean bias has a large effect on our evaluation.

Evaluation against independent proxy data shows that our reanalysis captures the timing and magnitude of low-frequency climate changes (Figs. 2.6 and 2.7) and is an improvement over both the prior ensemble and TraCE-21ka (Figures A.6 -A.7 and A.8-A.9). Evaluation over the full 20,000 years of the temperature and precipitation results shows high, positive correlation coefficients (ranging from a minimum of 0.97 to maximum of 0.99), which indicate that the reanalysis captures both the timing and sign of climate events, while high CE (0.87-0.98) and low RMSE values (0.62-1.2 ‰ for δ^{18}O and 0.04-0.08 for accumulation) indicate that the reanalysis captures the magnitude of these events. Our skill during this longest evaluation period is primarily due to the presence of low-frequency climate changes, which tend to be coherent across Greenland, such that evaluation over this full 20,000-year period shows more skill than evaluation over the full Holocene, which shows more skill than evaluation over just 5,000 years in the Holocene (or 5,000 years in the glacial) (Figures 2.6 and 2.7).

Our posterior ensemble consistently shows improvement over the uninformed, constant prior ensemble during the 20,000-year evaluation period (Figures A.6 and A.7). The TraCE-21ka simulation is also uninformed by the ice-core data, but it is transient and generally captures glacial to Holocene changes. Over the 20,000-year evaluation period, relative to the reconstructions, we find that TraCE-21ka has consistently lower correlation coefficients (0.86-0.96), lower CE values (0.50-0.86), and higher RMSE values (1.9-2.8 ‰ for δ^{18}O and 0.11-0.15

for accumulation) (Figures A.8 and A.9). This comparison suggests that our reconstruction captures the timing and magnitude of the glacial to Holocene transition better than TraCE-21ka.

Even for the shorter evaluation periods, which are dominated by high-frequency, spatially-incoherent noise, the reanalysis shows improvement over both the prior ensemble and TraCE-21ka (Figures A.6 -A.7 and A.8-A.9); however, the improvement is not as consistent as for the 20,000-year evaluation period. For our reconstruction, correlation is positive except for three locations in the temperature reconstruction, with Holocene precipitation showing the largest correlation values (up to 0.60) and the total range being -0.30 to 0.60. The prior correlation is zero for these shorter evaluation periods and locations; however, TraCE-21ka shows correlation values ranging from -0.29 to 0.69, with eight negative correlations (more than we find for our reconstruction), but generally higher correlations in the Holocene than our reconstruction.

For the shorter evaluation periods, the reconstruction CE is generally negative (ranging from -82 to 0.17) with a few exceptions; however, the reconstruction may still be skillful (e.g., Cook et al., 1999). The skill of the reconstruction is better measured by the difference between prior and posterior CE due to the strong influence that bias can have on CE (Hakim et al., 2016). There is consistent improvement of the posterior CE over that of the prior (ranging from an increase of 4.7 to 3200) and over that of TraCE-21ka (ranging from an decrease of -6.9 to an increase of 230). RMSE is the most consistent of the skill metrics for these shorter evaluation periods, with our reconstruction showing improvement over both the prior and TraCE-21ka, the one exception being that TraCE-21ka has greater skill at the Agassiz ice-core site in the Holocene. For the reconstruction, RMSE values range from 0.24 to 1.8 $‰^2$ for temperature and 0.025 to 0.10 for precipitation.

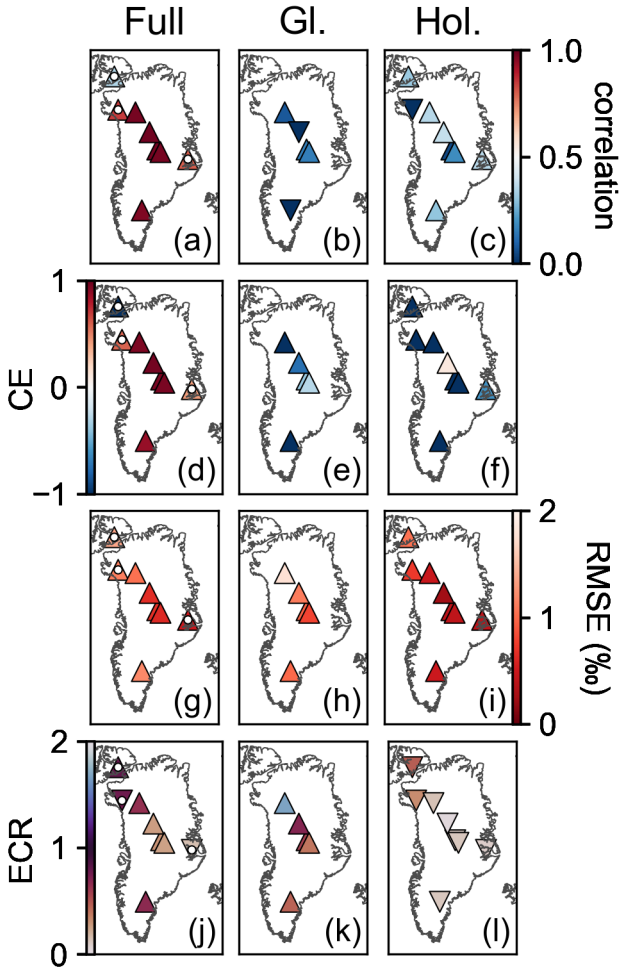

Figure 2.6: Skill metrics averaged over iterations and time for the temperature reanalysis. The first column (panels (a), (d), (g), and (j)) shows the skill metrics for the full overlap (Full) between the proxy record and reanalysis. A white dot indicates evaluation against proxy records that overlap only the Holocene (11.7-0 ka). The middle column (panels (b), (e), (h), and (k)) shows the skill metrics for a period in the glacial (Gl.) (20-15 ka), while the right column (panels (c), (f), (i), and (l)) is for a period in the Holocene (Hol.) (8-3 ka). The first row (panels (a)-(c)) reports the correlation coefficient, the second row (panels (d)-(f)) the coefficient of efficiency (CE), the third (panels (g)-(i)) the root mean square error (RMSE), and the fourth row (panels (j)-(l)) the ensemble calibration ratio (ECR). Triangle symbols pointing up indicate that the posterior ensemble evaluates better than the prior ensemble for that location and statistic. Triangle symbols pointing down indicate the opposite. We define better evaluation as correlation coefficient closer to 1, CE closer to 1, RMSE closer to 0, and ECR closer to 1.

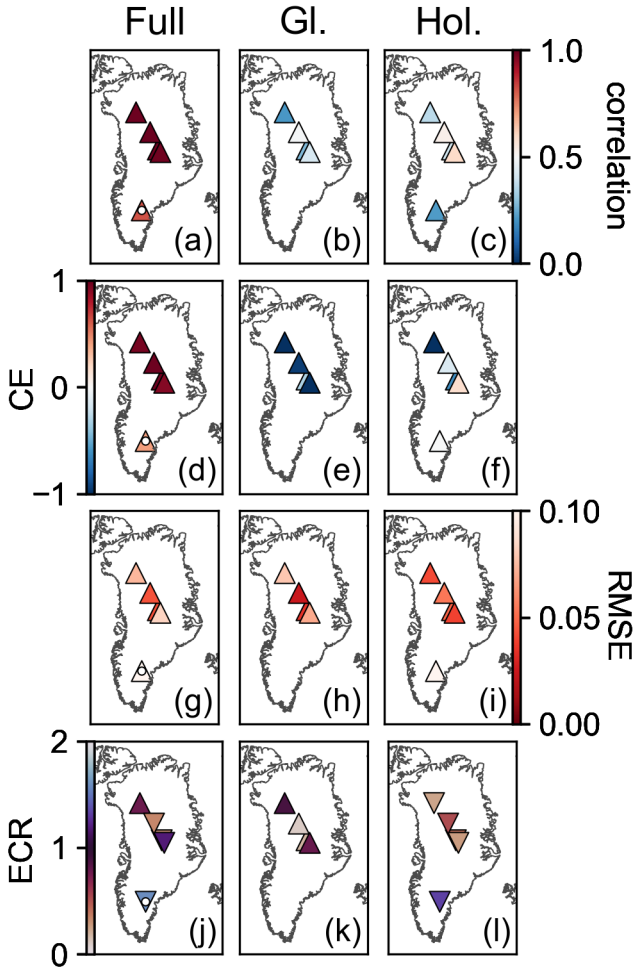

Figure 2.7: Skill metrics averaged over iterations and time for the precipitation reanalysis. The first column (panels (a), (d), (g), and (j)) shows the skill metrics for the full overlap (Full) between the proxy record and reanalysis. A white dot indicates evaluation against proxy records that overlap only the Holocene (11.7-0 ka). The middle column (panels (b), (e), (h), and (k)) shows the skill metrics for a period in the glacial (Gl.) (20-15 ka), while the right column (panels (c), (f), (i), and (l)) is for a period in the Holocene (Hol.) (8-3 ka). The first row (panels (a)-(c)) reports the correlation coefficient, the second row (panels (d)-(f)) the coefficient of efficiency (CE), the third (panels (g)-(i)) the root mean square error (RMSE), and the fourth row (panels (j)-(l)) the ensemble calibration ratio (ECR). Triangle symbols pointing up indicate that the posterior ensemble evaluates better than the prior ensemble for that location and statistic. Triangle symbols pointing down indicate the opposite. We define better evaluation as correlation coefficient closer to 1, CE closer to 1, RMSE closer to 0, and ECR closer to 1.

For all evaluation periods and both variables, the ensemble calibration ratio (ECR) for

the prior is skewed towards values greater than unity (0.66-8.7), which suggests that the prior ensemble tends to have too little spread. Conversely, for the posterior, the ECR is generally less than unity (0.10-1.7) (Figures 2.6 and 2.7), suggesting that the posterior ensemble has more spread than the error in the ensemble mean (as compared to the proxy records). This result indicates that the reanalysis ensemble encompasses the climate as recorded by the proxy records for most times and locations over the last 20,000 years.

2.3.3 Sensitivity Evaluation

Proxy networks that change in time, such as ours, can introduce artificial discontinuities into the reanalysis, especially if the number of proxies is low or the proxy uncertainty values are inappropriate. We produce another reconstruction with a fixed proxy network, in which all assimilated proxy records participate in every time step in the reconstruction (see Section 2.2.3). A comparison of these results with our main reanalysis shows no apparent discontinuities for the ensemble mean and 5th to 95th percentiles at Summit (Figure 2.8) or other locations around Greenland.

Our results are sensitive to the δ^{18}O-T_{site} relationship. To test this, we compare the main reanalysis to the four scenarios (S1-S4, as described in Section 2.2.3) that use different δ^{18}O PSMs, each of which assumes a different slope and spatial pattern of the δ^{18}O-T_{site} relationship. We show this comparison for Summit as an example (Figure 2.9), but the findings are applicable for all locations. As discussed previously, scenarios S1-S3 all assume that the δ^{18}O-T_{site} relationship has a uniform spatial pattern, but they each assume a different influence of precipitation seasonality. From these scenarios, we find that the temperature reconstruction is sensitive to the assumed precipitation seasonality, especially in the glacial where a stronger seasonality results in a greater glacial temperature anomaly. At Summit, this difference is nearly 10 °C between S1, which assumes no influence, and S3, which assumes the most influence of precipitation seasonality (Figure 2.9). Similarly, the main reanalysis and S4 scenario both assume that the δ^{18}O-T_{site} relationship has a spatially-variable pattern, but S4 assumes a greater influence of precipitation seasonality. Again we find that the results

are sensitive to assumed seasonality, with the greatest impact on the glacial-to-interglacial change.

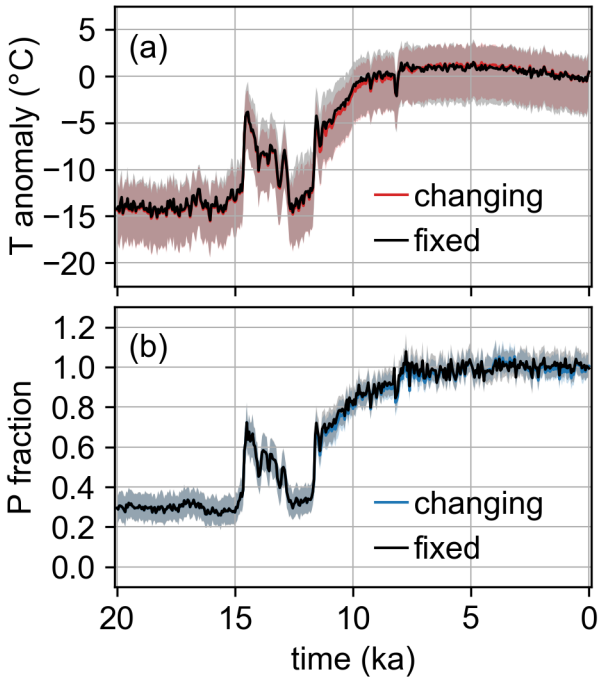

Figure 2.8: Changing (red and blue) vs. fixed (black) proxy-network for the (a) temperature (T) and (b) precipitation (P) reanalysis mean and 5^{th} to 95^{th} percentile shading. Anomalies and fractions are with respect to the mean of 1850-2000 CE. These time series are for the location closest to Summit, which is representative of the results around Greenland.

The temperature results are also sensitive to the spatial pattern of the δ^{18}O-T_{site} relationship. We find this by comparing the results from the S1-S3 scenarios that assume a spatially-uniform relationship to results from the main reanalysis and S4 scenario that assume a spatially-variable relationship. The S1-S3 scenarios have a characteristic shape to their time series (Figure 2.9), and, although the main reanalysis and S4 scenario generally fit this characteristic shape in the glacial and middle-late Holocene, in the early Holocene the main reanalysis and S4 diverge and show slower warming trends than the S1-S3 scenarios (Figure 2.9b). In addition, the reconstructions with spatially-varying δ^{18}O-T_{site} relationships show stronger north-south gradients during times of abrupt temperature change than those with spatially-constant relationships (Tables A.2 and A.3). These findings indicate that there

is new information added by using a PSM that includes spatial variability in precipitation seasonality.

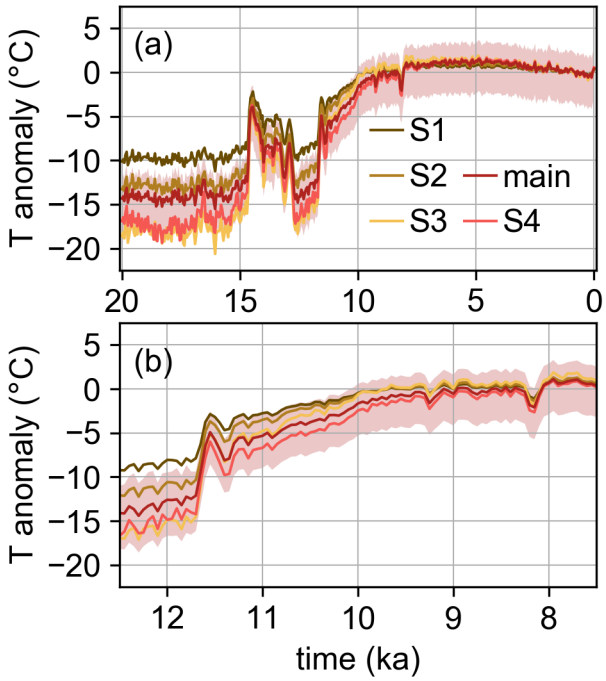

Figure 2.9: The main temperature (T) reanalysis (ensemble mean and 5^{th} to 95^{th} percentile shading) and ensemble mean for four sensitivity scenarios, S1-S4. Panel (a) shows the full 20,000 year reconstruction, while panel (b) shows a the Younger Dryas to early Holocene period (13 to 7 ka). Each sensitivity scenario reflects a different assumption about precipitation seasonality, with S1-S3 assuming a spatially-uniform seasonality and S3-S4 assuming stronger seasonality than the main reanalysis. Anomalies are with respect to the mean of 1850-2000 CE. These time series are for the location closest to Summit, which is representative of the results around Greenland.

For precipitation, we find that the results are sensitive to which accumulation record is assimilated at each ice-core site. As explained in Sections 2.2.1 and A.1, we use a low, moderate, and high accumulation record for most of the ice-core sites to produce the low, main, and high precipitation scenarios, respectively (Figure 2.10). The largest spread among the scenarios is in the earliest part of the reconstruction, i.e. the last glacial through the early Holocene, since uncertainties in the ice thinning history have the greatest impact at greater depths (and hence, greater ages). There is also a larger spread among the scenarios at more

southern locations because the accumulation record at Dye3 has both the most influence on southern Greenland (Section A.4) and the largest uncertainty in the ice thinning history (Figure 2.3, Section A.2).

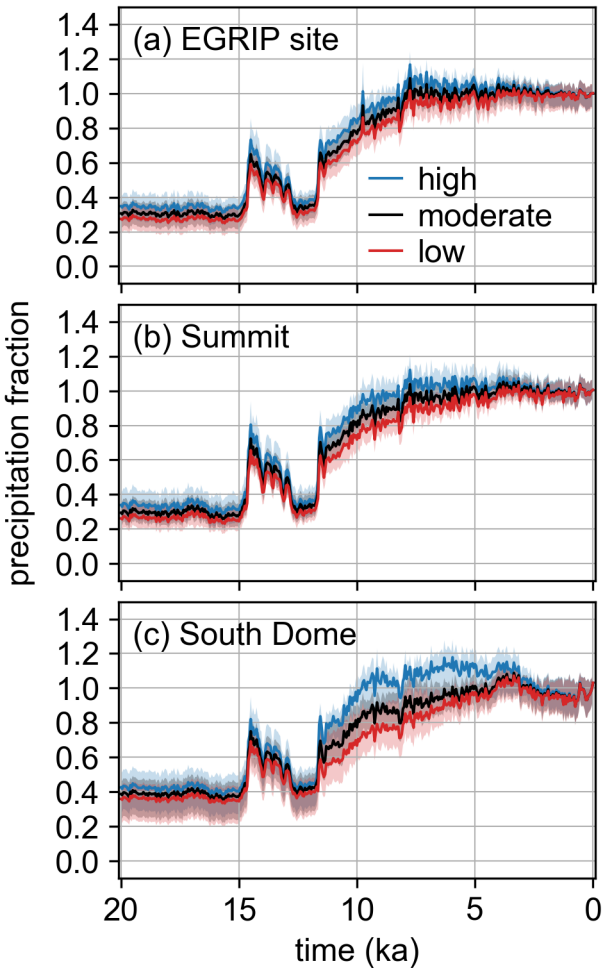

Figure 2.10: Ensemble mean and 5^{th} to 95^{th} percentile shading for the main precipitation reanalysis (black), high sensitivity scenario (blue), and low sensitivity scenario (red). Fractions are with respect to the mean of 1850-2000 CE. (a) is the time series for the location closest to the EGRIP ice-core site, (b) is closest to Summit, and (c) is closest to South Dome, which are representative of northern, central, and southern Greenland and are shown on a map in Figure 2.4.

2.4 Discussion

2.4.1 Precipitation-Temperature Relationship

Our results allow us to investigate the relationship between temperature and precipitation. To facilitate comparison with thermodynamic scalings widely used by ice-sheet models, we define the relationship as exponential and find the best fit for our reanalysis:

$$P_{fraction} = \frac{P_{past}}{P_{modern}} = e^{\beta(T_{past} - T_{modern})} \tag{2.8}$$

where P is the precipitation rate, T is the temperature, and β is a scaling factor (Greve et al., 2011). For a given temperature change, a higher value of β results in a larger change in precipitation (orange in Figure 2.11a). In ice-sheet models that use this scaling, it is commonly applied with a uniform β value for all locations (e.g., Huybrechts et al., 1991; Huybrechts, 2002; Greve, 1997; Greve et al., 2011; Pollard and DeConto, 2012; Cuzzone et al., 2019). The best-fit scaling-factors (β) center on the Greve et al. (2011) value of 0.07 for locations around Greenland, but the scaling factors tend to be larger (β >0.10) where late-glacial precipitation is lowest and smaller (β <0.05) where late-glacial precipitation is highest (Figures 2.4d and 2.11a).

Spatial varibility in the temperature-precipitation relationship was also found by a previous study, which looked at decadal averages over a recent 110 year period (Buchardt et al., 2012). Also using an exponential to represent the relationship, Buchardt et al. (2012) similarly found weaker relationships in northern than in central and southern Greenland (compare their Figure 3 to our Figure 2.11). In southern Greenland, they found a negative β value in southwest and a positive value in southeast Greenland, which they attribute to the Foehn effect. We find the opposite pattern, with larger, positive β values in southwest Greenland as compared to southeast Greenland. These differences may result from the time periods, timescales, and spatial resolutions considered in each investigation and from methodology. The spatial pattern found by (Buchardt et al., 2012) is limited to the ice-core locations they considered, such that they have little information about the relationship near the ice-sheet

edges. The spatial pattern in our reanalysis is influenced by both the ice-core records and the spatial covariance structures of the prior ensembles. With only one long ice core in southern Greenland, the east-west gradient in β values is highly influenced by the spatial patten inherited from TraCE-21ka.

The precipitation-temperature relationship in our reanalysis is driven by the assimilated ice-core records, though, as mentioned above, the spatial pattern of this relationship is also influenced by the spatial covariance structures of the prior ensembles. Previous work with ice-core records has found that the relationship between temperature and precipitation is frequency dependent, with a stronger relationship at lower frequencies (Cuffey and Clow, 1997); as expected, there is a similar frequency-dependence in our reanalysis. We find that an exponential scaling captures the low-frequency glacial to Holocene precipitation change; however, this fails at higher frequencies (Figure 2.11b-e). To evaluate this frequency-dependence, we filtered our results using 6th order, low-pass and high-pass Butterworth filters with 5,000 year^{-1} cutoff frequencies. The low-pass filtered dataset shows the same precipitation-temperature relationship as the unfiltered dataset (Figure 2.11c-d), while the high-pass filtered dataset shows that precipitation is less sensitive to changes in temperature (i.e., the value of β is lower) at these higher frequencies (Figure 2.11e). This decoupling of temperature and precipitation is apparent in the amplitude difference of high-frequency signals in the glacial and the Holocene. In our temperature reanalysis, we find that high frequencies in the glacial have a greater amplitude than those in the Holocene, while in our precipitation reanalysis, we find the opposite. A single scaling, as is typically used in ice-sheet modeling, cannot capture this difference.

We examine how the sensitivity experiments (Figures 2.9 and 2.10) affect the scaling factor (β) in the precipitation-temperature relationship. We pair the five temperature reconstructions (main, S1-S4) and three precipitation reconstructions (low, moderate, and high) into fifteen possible combinations and conduct the same analysis as described above. Across these fifteen combinations, we find that the spatial pattern of β is robust (Figure 2.11a). The exact magnitude depends primarily on the temperature reconstruction and how cold

it is in the glacial, with colder temperatures giving lower β values. To a lesser degree, the magnitude also depends on the precipitation reconstruction, with wetter scenarios giving lower β values. As previously, we find that the low-pass filtered datasets have the same or nearly the same β value as the unfiltered dataset, while the high-pass filtered datasets have consistently lower β values. As an example of this, Table A.4 shows the β value found for the Kangerlussuaq region for all fifteen combinations and three filtering options.

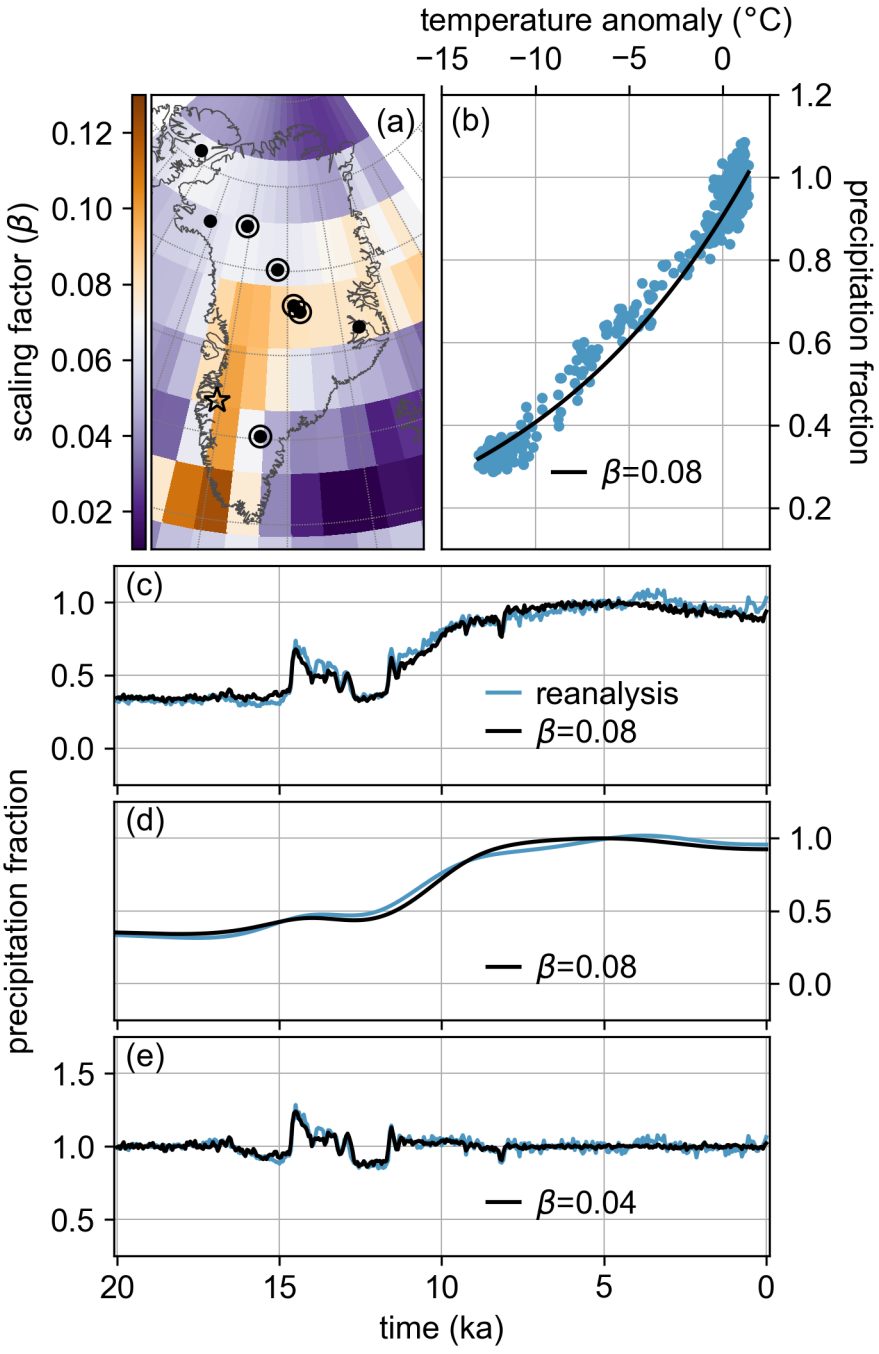
temperature anomaly (°C)
−15
−10
−5
0
(a)
(b)
(c)
(d)
(e)
scaling factor (β)
0.12
0.10
0.08
0.06
0.04
0.02
1.2
1.0
0.8
0.6
0.4
0.2
precipitation fraction
β=0.08
reanalysis
β=0.08
β=0.08
β=0.04
1.0
0.5
0.0
1.5
1.0
0.5
precipitation fraction
20
15
10
5
0
time (ka)

Figure 2.11: The precipitation-temperature relationship in our reanalysis. (a) shows the spatial pattern of the scaling factor (β) for the best-fit thermodynamic scaling. The colorbar is centered on 0.07, the value used by Greve et al. (2011). Points indicate ice-core locations used for each reanalysis with closed circles indicating δ^{18}O records and open circles indicating accumulation records. The star is at the center of the area used in panels (b)-(e) (65N to 68.7N and 48.5W to 52.5W). (b) is a scatter plot of temperature anomaly vs. precipitation fraction from the reanalysis (blue points). The black line shows the best-fit exponential scaling. (c) shows the time series of the precipitation reanalysis (blue line) and precipitation scaled from temperature using the best-fit scaling (black line). (d) and (e) are the same as (c) except low-pass and high-pass filtered, respectively, with a cutoff frequency of 5,000 year^{-1}.

2.4.2 Spatial Patterns During Abrupt Climate Change Events

Our paleoclimate data assimilation framework is not limited to the assimilation of δ^{18}O and accumulation rate records. In this section we examine how our reanalysis compares to reconstructions driven by another type of proxy, δ^{15}N of N_2. In particular, we focus on abrupt temperature events, for which there is previous work using δ^{15}N (e.g., Severinghaus et al., 1998; Guillevic et al., 2013; Buizert et al., 2014). Abrupt temperature events increase the thermal gradient in the firn – the upper, porous portion of the ice column – which leads to fractionation of the stable isotopes of N_2 (Severinghaus et al., 1998). Using a firn compaction model, temperature can be derived from δ^{15}N measurements with inverse methods (e.g., Severinghaus et al., 1998; Severinghaus and Brook, 1999; Guillevic et al., 2013; Kindler et al., 2014; Buizert et al., 2014; Kobashi et al., 2017). We assimilate temperatures derived from δ^{15}N data collected from the GISP2, NGRIP, and NEEM ice cores (Buizert et al., 2014).

Our reanalysis and the Buizert et al. (2014) records cover three abrupt temperature events – the Bølling-Allerød warming (14.6 ka), cooling into the Younger Dryas (12.9 ka), and warming at the end of the Younger Dyras (11.5 ka). For these three abrupt temperature events, the δ^{15}N-derived temperature records show larger temperature changes at GISP2 in central Greenland (Buizert et al., 2014), while the δ^{18}O changes are larger at NEEM in northwest Greenland (Figure 2.2). We perform three sets of experiments to investigate how

these two sets of proxy records affect the mean spatial pattern indicated by our reanalysis during abrupt temperature events. The first experiment, "O8", assimilates all eight δ^{18}O records with one 100-member prior ensemble from TraCE-21ka. This results in a 100-member reanalysis ensemble. The second experiment, "N3O5", assimilates all three of the δ^{15}N-derived temperature records and the five remaining δ^{18}O records (those that do not overlap with the δ^{15}N sites), using the same 100-member prior ensemble as used in the O8 experiment. Finally, we perform a modified experiment, "N3O5_BA", with both δ^{18}O and δ^{15}N records, but using a prior ensemble selected from the 1,000 years surrounding the Bølling-Allerød warming. To maintain a 100-member prior ensemble, we use decadal rather than 50 year averages of TraCE-21ka for this experiment. This adjustment does not affect the comparison (results not shown). Detailed methods for these experiments are given in Section A.6.

For both the O8 and N3O5 experiments, the spatial pattern for the abrupt climate change events are similar to our main reanalysis, with the largest magnitude temperature changes in northern and northwestern Greenland, decreasing magnitude with decreasing latitude, and slightly larger change in the central east and southeast than corresponding western regions. For example, the spatial pattern of the Younger Dryas cooling is nearly the same regardless of which grouping of records is assimilated (Figures 2.12a and b). This overall finding is robust to different combinations of these proxy records; for example, if we assimilate just the three δ^{15}N-derived temperature records and no δ^{18}O records (results not shown) the pattern is not substantially changed. This pattern of temperature change differs from spatial patterns inferred previously from δ^{15}N for various abrupt climate events (Guillevic et al., 2013; Buizert et al., 2014); however, the O8 and N3O5 experiments show that these differences are not due to the assimilation of δ^{18}O rather than δ^{15}N-derived temperatures. The replacement of δ^{18}O records with δ^{15}N-derived temperature records does not change the overall spatial pattern of these abrupt events, though it does result in a reconstruction with slightly larger temperature changes in the south and slightly smaller changes in the north. This effect, however, is less important than the choice of prior ensemble, as is shown by the third experiment, N3O5_BA.

For N3O5_BA, we restrict the prior ensemble to the Bølling-Allerød warming, which pro-

duces a reconstructed spatial pattern similar to those reported by Buizert et al. (2014) for each of the three abrupt climate events. In TraCE-21ka, the Bølling-Allerød warming is forced by a sudden termination of freshwater forcing in the North Atlantic (Liu et al., 2009). This forcing leads to large temperature fluctuations in southern Greenland that decrease with increasing latitude. With this covariance pattern dominating the prior ensemble, the N3O5_BA reconstruction indeed shows the largest temperature changes in southern Greenland, followed by central and then northern Greenland (Figures 2.12c, A.12c, and A.13c).

These experiments suggest that current ice-core records are insufficient to place a strong constraint on the spatial pattern of abrupt climate events. Reconstructions of these events may be improved with additional data, especially from southern Greenland (Section A.4), and with prior ensembles that are designed to sample over uncertainty in the forcing and boundary conditions unique to these events.

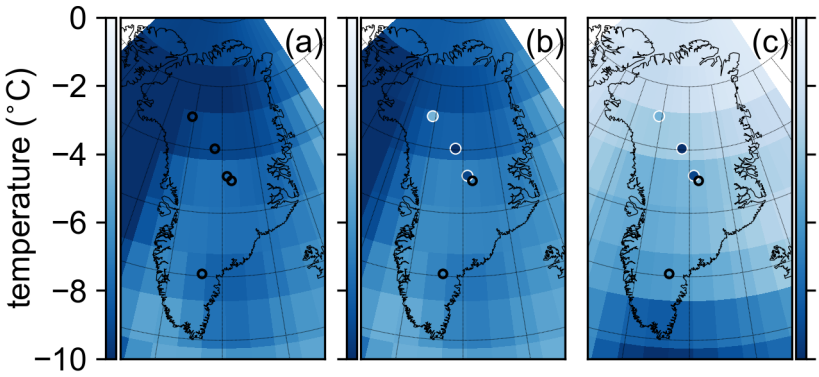

Figure 2.12: Spatial pattern of the abrupt cooling event into the Younger Dryas. Panel (a) shows results from experiment O8, assimilating all eight δ^{18}O records, panel (b) shows results from experiment N3O5, assimilating all three δ^{15}N-derived temperature records and the remaining five δ^{18}O records (those that do not overlap with the δ^{15}N sites), and panel (c) shows results from experiment N3O5_BA, which is similar to the N3O5 experiment except the prior ensemble is selected from the 1,000 years surrounding the Bølling-Allerød warming. Unfilled black circles show locations of assimilated δ^{18}O records, while filled circles with white outlines show locations of assimilated δ^{15}N-derived temperature records. Filled circles in panels (b) and (c) show the δ^{15}N-derived temperature values as reported by Buizert et al. (2014) on the same color scale as the rest of the panel. The temporal definition of this event is the same as defined in Buizert et al. (2014).

2.4.3 Climate and the Ice Sheet: A Case Study of Southwest Greenland

Our main reanalysis is one of very few spatially-complete time series of Greenland climate over the last 20,000 years. Here, we compare our reanalysis with other Greenland climate histories, and suggest that, together, they should be treated as an ensemble of climate boundary conditions that can be used to produce ensembles of ice-sheet model simulations. These climate histories can also be further evaluated using a combination ice-sheet models and independent constraints from the glacial-geologic record of past ice-sheet configurations.

We compare our results with the recent reconstruction of Buizert et al. (2018), hereafter referred to as the B18 reconstruction. The B18 temperature reconstruction was produced by adjusting a part of the TraCE-21ka temperature field that is affected by changes in the Atlantic meridional overturning circulation such that the full temperature field provides a good match to an average of three δ^{15}N-derived temperature records recovered from ice cores. The B18 snow-accumulation reconstruction is simply a reference climatology scaled to accumulation rates from the GISP2 ice core. We treat this as a precipitation reconstruction, but note that accumulation may be less than precipitation at some locations around Greenland, especially near the coast. It is also informative to compare these results with our S4 temperature and high precipitation reconstructions (hereafter referred to as S4 and high P or simply 'sensitivity' as in Figure 2.13), as well as the TraCE-21ka simulation itself (i.e., the climate model output, unconstrained by data). For brevity, we focus on the area around Kangerlussuaq in southwest Greenland, but the comparisons are generally applicable to any region of Greenland. Southwest Greenland is of interest because the ice-sheet behavior here is primarily a response to changes in surface forcing (i.e., temperature and precipitation) because there are few tidewater glaciers (Cuzzone et al., 2019). Furthermore, the Kangerlussuaq region has a particularly well-documented ice-sheet retreat history through the Holocene (Young and Briner, 2015; Lesnek and Briner, 2018).

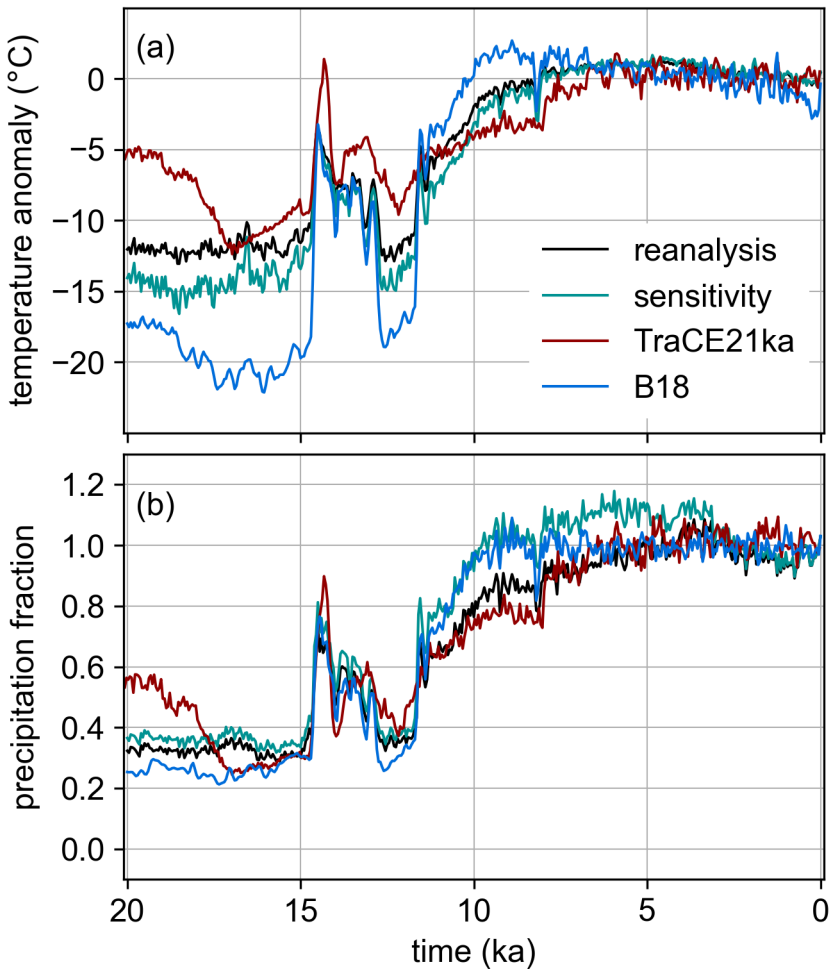

Figure 2.13: Temperature (a) and precipitation (b) reconstructions from our main reanalysis (black), our sensitivity scenarios S4 and high P (green), TraCE-21ka (red), and B18 (blue) (Buizert et al., 2018). Each reconstruction is averaged to a 50 year time resolution and averaged over a spatial domain in the Kangerlussuaq region, defined by the latitude-longitude box 65N to 68.7N and 48.5W to 52.5W, the center of which is located at the star in Figure 2.11a. Temperature anomalies and precipitation fraction are defined with reference to the mean of 1850-2000 CE.

In the Kangerlussuaq region, the B18 reconstruction shows more extreme temperature changes than our reconstructions, with late-glacial (20-15 ka) anomalies of about −20 °C and peak HTM temperature anomalies of about +2 °C at 9 ka (Figure 2.13). B18 also shows a faster rate of transition between the glacial and Holocene, reaching temperatures close to modern by 10 ka. In constrast, TraCE-21ka shows more moderate temperature

anomalies and a slower transition, with late-glacial anomalies of about −8.6 °C and near-modern temperatures that first appear around 7 ka. TraCE-21ka has no obvious HTM in this location or any location in Greenland. Our main reanalysis and the S4 version of our temperature reanalysis both lie between B18 and TraCE-21ka, with late-glacial anomalies of about −12 and −14 °C, respectively, Holocene peak temperature anomalies of +1 °C around 5 ka, and temperatures close to modern first appearing around 8 ka.

For precipitation, the B18 reconstruction again tends to show the largest fluctuations and fastest transition, with a late-glacial precipitation fraction of about 0.26 and precipitation rates close to modern first appearing just after 10 ka. TraCE-21ka again shows the most moderate fluctuations and a slower transition, with a late-glacial fraction of about 0.38 and rates close to modern not appearing until around 5 ka. Our main reanalysis and high P lie in the middle during the late-glacial, with fractions of about 0.32 and 0.36, respectively; however, our main reanalysis has a slow transition into the Holocene, similar to TraCE-21ka, while high P has a fast transition similar to B18. In the Holocene, high P shows the most elevated precipitation out of all the reconstructions, with 10-15% more precipitation than modern occurring around 7-3 ka. B18 shows precipitation values similar to modern for the last 10,000 years of the Holocene, while TraCE-21ka and our main reanalysis show lower-than-modern precipitation throughout most of the Holocene.

All of these paleoclimate reconstructions – our main reanalysis, the sensitivity scenarios, and B18 – are plausible histories of temperature and precipitation over Greenland. Given any past change in the ice-sheet, each of these histories has a different implication for ice-sheet sensitivity to climate, the veracity of which could be tested by using them to force an ice-sheet model and comparing this ensemble of results to the geologic record.

Our results have potentially important implications for the response of the Greenland ice sheet to climate change. In particular, we find maximum Holocene temperatures were reached around 5 ka, which is between 500 years earlier and 4,000 years later than most previous estimates. Moreover, there is little corresponding change in precipitation in our main reanalysis and the low sensitivity scenario. If these findings are correct, they imply

a relatively rapid response to temperature forcing for sections of the ice sheet margin that retreated less than a century later (Young and Briner, 2015). A caveat is that proxy data remains very sparse, particularly in southern Greenland, where the poorly-resolved Dye3 core is the only long record. Future work to obtain improved measurements on the Dye3 core, or to gather new data from southern Greenland, would help to alleviate this limitation, as would the incorporation of data from off the ice sheet, such as from lake and ocean sediment cores.

An important distinction among various different paleoclimate reconstructions for Greenland is in the treatment of elevation changes. Any paleoclimate reconstruction from ice-core records is complicated by ice-sheet elevation changes. In Vinther et al. (2009), it is assumed that the climate history is the same at all locations around Greenland, and that any differences among the ice core paleotemperature records is a result of that elevation change. In B18, past elevation changes are assumed to be negligible. In our reconstruction, the impact of elevation change on the spatial covariances of temperature and precipitation is implicitly accounted for as part of the data assimilation methodology. Formally, our reconstruction is of surface climate, not climate at a fixed elevation. Consequently, our reanalysis may not be directly comparable to other paleoclimate reconstructions. For example, the HTM is commonly reconstructed as an early Holocene event in records that are at a fixed or nearly-fixed elevation. In our reanalysis, the early Holocene is cooler than the mid Holocene. Changes in the ice-surface elevation could account for this apparent discrepancy. Thinning in the early Holocene (Vinther et al., 2009) would result in a lowering of the ice surface and an apparent warming at the ice surface due to lapse rate effects. This warming signal would be captured in ice-core records. If the warming trend due to surface lowering occurs at the same time as an overall climate cooling, then the climate signal would be dampened or possibly reversed.

Our method depends on the accuracy of the climate-elevation relationships in our prior – i.e. in the TraCE-21ka climate model simulation, which probably does not capture such relationships with particularly high fidelity since the model resolution is low and the climate and ice-sheet models are not coupled. Future work could take advantage of the probabilistic

relationships among accumulation, temperature, and surface elevation as simulated in fine-scale regional climate models (Edwards et al., 2014).

2.5 Conclusions

Paleoclimate data assimilation is a novel method for reconstructing climate fields over the Greenland ice sheet. Our approach, combining ice-core records with a climate-model simulation, provides complete spatial reanalyses of mean-annual temperature and precipitation covering the last 20,000 years. Evaluation against independent proxy records shows that this methodology leads to significant and meaningful improvement over the prior ensemble (drawn from a climate simulation) and TraCE-21ka. Between the posterior ensemble and sensitivity experiments, our results provide a range of climate scenarios for ice-sheet modeling. Moreover, independently reconstructing both precipitation and temperature allows the assumption of purely thermodynamic control on precipitation to be relaxed, and an examination of the relationship between these quantities over a range of timescales. Specifically, we find that the Clausius-Claypeyron scaling is a good approximation over glacial-interglacial cycles, but not for shorter timescales where precipitation variability partially decouples from temperature.

Paleoclimate reconstructions would benefit from a larger selection of long climate-model simulations at higher resolution. Particularly valuable would be transient simulations that include water isotopes as prognostic variables, which allows for direct assimilation of water isotope ratios (Steiger et al., 2017; Okazaki and Yoshimura, 2017), rather than the use of an explicit proxy system model between temperature and δ^{18}O. Recent work shows significant improvements to the realism of water-isotope enabled models in the polar regions (Nusbaumer et al., 2017; Dütsch et al., 2019a; Cauquoin et al., 2019; Okazaki and Yoshimura, 2019), and longer simulations, once available, should allow us to further improve upon the results we have presented here. In principle, our method could also be applied to climate-model simulations that include a fully-coupled Greenland ice sheet. At present, fully-coupled simulations of Greenland over thousands of years are prohibitively expensive except at low

resolution, and the limited work that has been done shows significant biases (Vizcaino et al., 2015). Nevertheless, incorporating data assimilation into such models would provide the groundwork for more-complete data-constrained simulations as computing power becomes less of a limiting factor in the future.

2.6 Data Availability

The paleoclimate reconstructions in this paper made use of code from the Last Millennium Reanalysis project, which is publicly available at https://github.com/modons/LMR (Hakim, 2019). The reconstructions and ice-core records, including the new accumulation histories for Dye3, GRIP, and NGRIP, are publicly available at the Arctic Data Center (doi:10.18739/A2599Z26M).

Chapter 3

UNCERTAINTY IN RECONSTRUCTING PALEO-ELEVATION OF THE ANTARCTIC ICE SHEET FROM TEMPERATURE-SENSITIVE ICE CORE RECORDS

Jessica Badgeley, Eric J. Steig, and Marina Dütsch

In Review at Geophysical Research Letters

3.1 Introduction

Paleoclimate proxy records are important sources of information for learning about Earth's past surface temperature. Such records reflect changes in climate forcings, including greenhouse gases, volcanic emissions, and Earth's orbital parameters; however, a record may also be influenced by elevation change depending on its location and timescale. For example, over millions of years tectonics cause shifts in the land surface and, on Quaternary timescales, the continental ice sheets evolve. Paleoaltimetry methods are designed to quantitatively estimate past elevation, which is one way to disentagle climate and elevation signals.

One paleoaltimetry method follows equation 3.1, which uses two temperature-sensitive proxy records (T) to determine the elevation (z) difference between their locations (see Meyer (2007) for a review of this method).

$$z_{\text{site}_1}(t) - z_{\text{site}_2}(t) = \frac{T_{\text{site}_1}(t) - T_{\text{site}_2}(t)}{-\Gamma} \text{ or } \Delta z(t) = \frac{\Delta T(t)}{-\Gamma} \tag{3.1}$$

In this approach, one of the records serves as an estimate of the shared climate. Deviations from this shared climate are scaled by a lapse rate (Γ) to obtain the elevation difference between the two sites, i.e., the relative elevation. If the elevation at one site is known, then the elevation at the other site can be obtained.

In practice, for the application discussed in this paper, the elevations and temperatures in equation 3.1 are anomalies with respect to some reference time period, for example, the modern state.

$$\Delta dz = \frac{\Delta dT}{-\Gamma} \tag{3.2}$$

where Δ denotes a spatial change in the variable and d denotes a temporal change in the variable.

Since early work developing this paleoaltimetry method from observational data (e.g., Axelrod, 1965), researchers have continued to improve it; however, the question of which temperature lapse rate is most applicable remains an active area of research (e.g., Meyer, 2007; Farnsworth et al., 2021). Several options have been considered: dry adiabatic, moist adiabatic, environmental (free air), and terrestrial (spatial or surface) lapse rate. Additionally, the choice must be made whether to use a global, regional, or local estimate derived, for example, from the modern climatology or a climate simulation of the time period of interest (Meyer, 2007). Lapse rates can vary from 3 to >10 °C/km, which implies a greater than factor-of-three difference in the resulting elevation estimate. Despite the uncertainty, this temperature-based paleoaltimetry method and similar isotope-based methods (Rowley, 2007) have been applied broadly across a variety regions and time periods.

Many studies argue that changes in ice sheet topography largely or fully explain the spatial variability of surface temperature change for a variety of locations and time periods Grootes and Stuiver (1986, 1987); Steig et al. (2001); Vinther et al. (2009); Masson-Delmotte et al. (2011); Werner et al. (2018); Buizert et al. (2021). In this study, we expand on this previous work by examining the uncertainty associated with estimating past ice sheet elevation changes from this temperature-based paleoaltimetry method. We begin by examining the thermodynamic assumptions for using temperature records for paleoaltimetry, following earlier work by Forest et al. (1995, 1999). We then evaluate these thermodynamic assumptions against an ensemble of climate simulations. Finally, we use the same climate ensemble to evaluate the sources of uncertainty in this method and to quantify the errors for our case study: changes in Antarctic ice sheet elevation from the Last Glacial Maximum (LGM) to

the pre-Industrial (PI).

3.2 Theoretical Background

The first law of thermodynamics can be written as follows by assuming hydrostatic balance and reversible external heating (Wallace and Hobbs, 2006) (Appendix B):

$$dT = -\Gamma_d dz + \frac{T}{\theta} d\theta \tag{3.3}$$

where Γ_d is the dry adiabatic lapse rate and θ is potential temperature. For the purposes of paleoaltimetry, equation 3.3 can be interpreted as a decomposition of temporal temperature change into an adiabatic component, $-\Gamma_d dz$, and a diabatic component, $\frac{T}{\theta} d\theta$, the latter of which can be impacted by both climate forcings and elevation-induced circulation change. When applied to a proxy record, this equation is not quite Lagrangian nor Eulerian because proxy records are fixed in horizontal space (assuming no tectonic movement) yet change elevation between the time periods of interest. We discuss the implications of this in Appendix B. The full derivation of this temperature decomposition (equation 3.3), and a moist version that includes the effects of water vapor (equation B.8; Randall (2009)), can be found in Appendix B.

Subtracting the decompositions for two sites from each other results in an equation for the relative elevation change ($\Delta dz = dz_{\text{site}_1} - dz_{\text{site}_2}$). Here this is done for the dry decomposition:

$$\Delta dz = \frac{(dT_{\text{site}_1} - dT_{\text{site}_2}) - (\frac{T}{\theta} d\theta_{\text{site}_1} - \frac{T}{\theta} d\theta_{\text{site}_2})}{-\Gamma_d} \tag{3.4}$$

By assuming that the diabatic temperature changes are the same at both sites, we obtain equation 3.2. From this derivation, we now know that the lapse rate is the moist or dry adiabatic lapse rate, depending on the application, but we still must assume that the lapse rate is constant in time. We've also learned that equation 3.2 assumes that both sites experience the same climate and that any differences in the proxy records are due to adiabatic effects of elevation.

3.3 Methods and Data

3.3.1 Error Quantification

Simulations from numerical models provide possible realizations of past climate that can be used to evaluate the temperature-based paleoaltimetry method and its uncertainty. We consider both the error:

$$\text{error} = \Delta dz_{\text{estimated}} - \Delta dz \tag{3.5}$$

and the signal-to-noise ratio (SNR):

$$\text{SNR} = \left| \frac{\Delta dz}{\text{error}} \right| \tag{3.6}$$

We quantify the uncertainty at ice core sites for which there are empirical estimates of the LGM temperature (Figure 3.1, table B.1). We also include Hercules Dome, a location in East Antarctica that is being considered as a future ice coring site (Jacobel et al., 2005), and a grid of locations that covers the continent with a uniform spacing of 200 km (grey points in Figure 3.1). To simplify the interpretation of the errors, for each pair of locations we define "site$_1$" and "site$_2$" such that Δdz is always positive; this is not necessary for general application of this method.

3.3.2 Climate Simulations

For our case study of the Antarctic ice sheet, we use an ensemble of ten climate models with simulations of the Last Glacial Maximum (LGM) and pre-Industrial (PI). Nine of the ensemble members are fully-coupled simulations from PMIP3, PMIP4, CMIP5, and CMIP6 (Paleoclimate Modeling Intercomparison Project phases 3 and 4 and Climate Modeling Intercomparison Project phases 5 and 6) with specified forcings and ice sheet changes (Braconnot et al., 2011, 2012; Taylor et al., 2012; Eyring et al., 2016; Kageyama et al., 2017). Each ensemble member is from a different climate model and each was chosen as the most up-to-date version of the simulations at the time of download from the World Climate Research Programme (November 23, 2020 to July 21, 2021). From PMIP3, we have simulations from

the CNRM-CERFACS, NASA-GISS, IPSL, LASG-CESS, and MRI modeling centers, and from PMIP4 we have simulations from the AWI, INM, MIROC, and MPI-M modeling centers (table B.2).

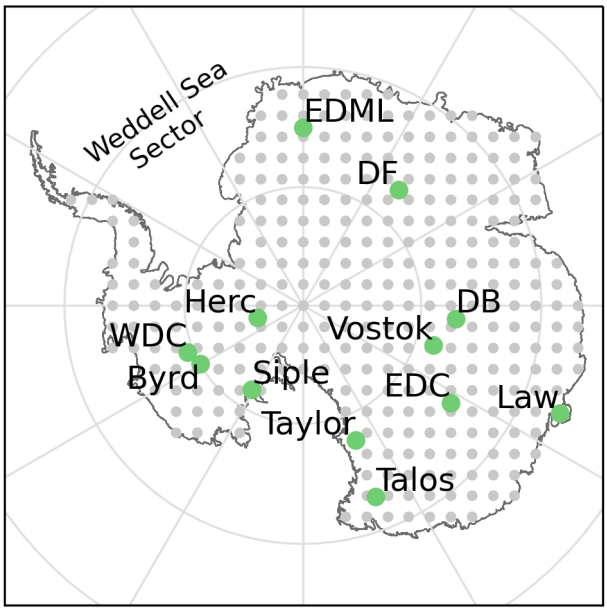

Figure 3.1: Ice core and other site locations. Ice core sites are shown by green points with labels (see table B.1 for the long name of each ice core). A grid of locations (grey points) spaced 200 km apart allows for analysis over the whole continent. For all spatial plots, latitude and longitude lines have 10° and 30° spacing, respectively, and the contenental outline is the modern grounding line (Haran et al., 2014).

An additional ensemble member, conducted for this study, is composed of three atmosphere-only simulations with iCESM1.2.0.1 (hereafter referred to as CESM) from the NCAR modeling center (Brady et al., 2019). These simulations are designed to separate the influences of climate forcings and elevation change on the temperature change. All three simulations are run with the finite-volume dynamical core at 1.9°Nx2.5°E horizontal resolution and a hybrid sigma-pressure vertical coordinate system with 30 levels. The PI simulation, which has ice sheet topography from GTOPO30 (U.S. Geological Survey, 1996), is forced with preindustrial (year 1850) greenhouse gas concentrations and orbital parameters, as well as sea surface temperatures and sea ice concentrations from Hurrell et al. (2008). The LGM simulation, which has ice sheet topography from ICE-6G (Peltier et al., 2015), is forced with

year 21 ka BP greenhouse gas concentrations and orbital parameters, as well as sea surface temperatures and sea ice concentrations from a coupled simulation by Zhu et al. (2017). The intermediate simulation is similar to the LGM simulation except that the Antarctic topography is replaced by the PI topography. Hereafter, we refer to the difference between the PI and LGM CESM simulations as $\text{CESM}_{\text{FULL}}$, the difference between the PI and intermediate simulations as $\text{CESM}_{\text{CLIM}}$, and the difference between the intermediate and LGM simulation as $\text{CESM}_{\text{ELEV}}$. The first includes both climate and elevation influences, the second includes the impact of climate forcings alone, and the third has only the impact of changing the elevation of the Antarctic ice sheet.

To obtain our results, we use the following variables from each PMIP simulation: two-meter air temperature, surface elevation, surface pressure, and surface specific and relative humidities. Surface humidities are not available for the FGOALS and IPSL simulations, so we use the lowest level atmospheric value for each grid cell. For the CESM simulations, we use the same variables but from the lowest level in the terrain-following coordinates. We do this because more than one variable was unavailable at surface or two-meter reference levels. Additionally, for several models, there is no grid cell at the South Pole. To avoid extrapolating values to the South Pole ice core location, we use the southernmost grid cell at the same longitude as the ice core (98.16° W) (Johnson et al., 2021; Souney et al., 2021). For variables that represent a change in time, we subtract the LGM from the PI (PI minus LGM). For all other variables, such as those in the diabatic term (equation 3.3), we use the LGM value, but find that this choice has a negligible impact on the results.

3.4 Results

3.4.1 Temperature Decomposition Applied to Climate Simulations

To evaluate the thermodynamic assumptions of the temperature-based paleoaltimetry method, we apply the dry and moist temperature decompositions (equations 3.3 and B.8) to the ensemble of climate simulations described in section 3.3.2. We also compute the residual, i.e.

the difference between the left and right sides of the equations. We find that the difference between the ensemble means of the dry and moist decompositions is 1.2 °C or less for the adiabatic component, diabatic component, and residual (Figures 3.2 and B.1). We use the dry decomposition throughout the rest of the paper because the dry adiabatic lapse rate is constant in space and time, which simplifies assumptions about how temporal changes in the lapse rate should be accounted for. Because the moist and dry lapse rates, and the decompositions that result from them, are similar over the Antarctic continent, our findings are not significantly affected by this choice.

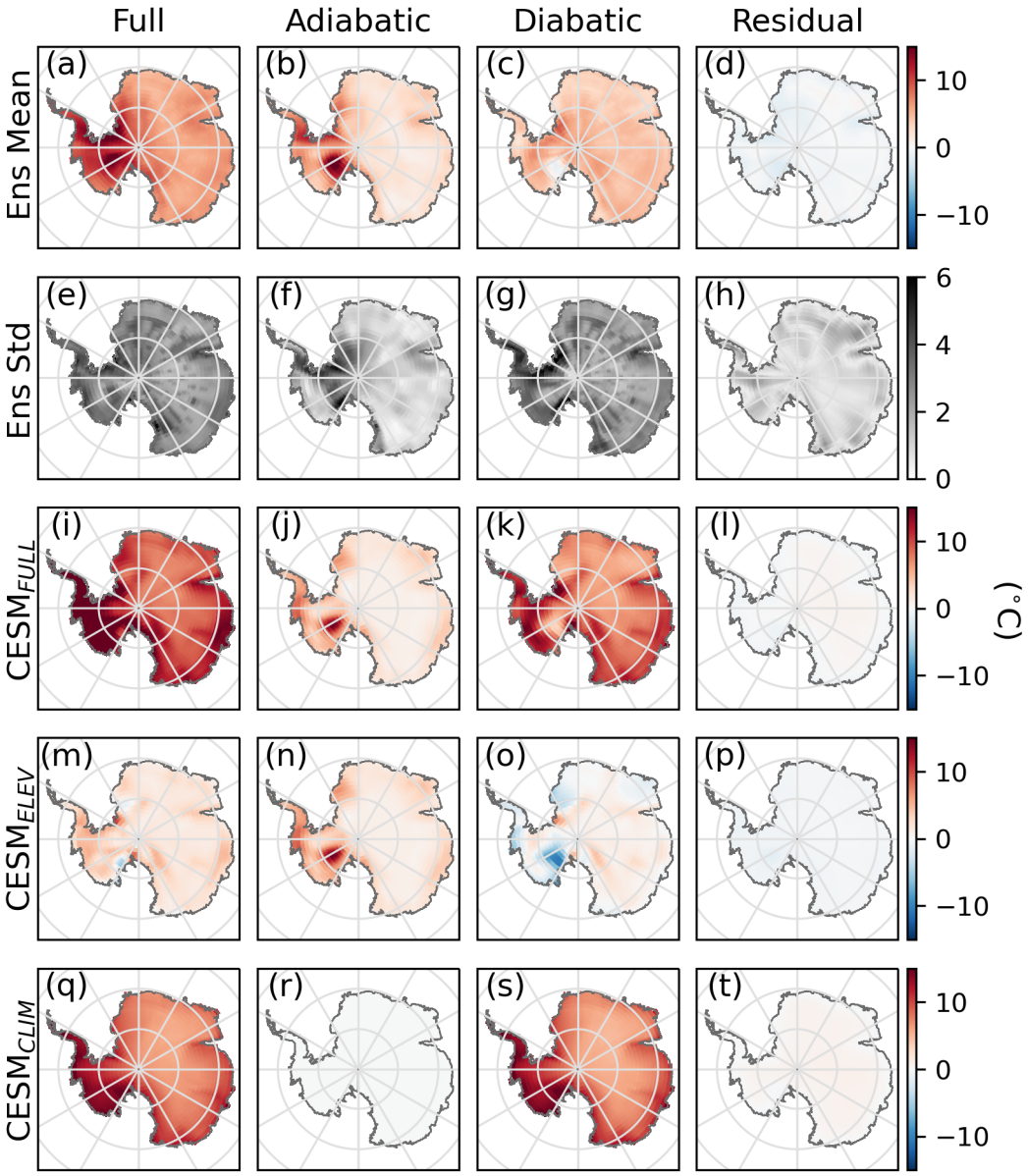

Figure 3.2: Temperature decomposition for Antarctica as calculated with the dry adiabatic lapse rate (equation 3.3). Panels (a)–(d) are ensemble means and panels (e)–(h) are ensemble standard deviations (std). Panels (a) and (e) show results for the full temperature change (PI minus LGM), panels (b) and (f) are for the adiabatic component, panels (c) and (g) are for the diabatic component, and panels (d) and (h) are for the residual. Panels (i)–(t) are similar except they show the dry temperature decomposition for the CESM ensemble member with both climate and elevation change ($\text{CESM}_{\text{FULL}}$), elevation change only ($\text{CESM}_{\text{ELEV}}$), and only changes in the climate forcings ($\text{CESM}_{\text{CLIM}}$).

All ensemble members impose greater ice loss in West Antarctica than in East Antarctica, which is apparent in the larger warming signal over this region as seen in both the full and adiabatic temperature changes (Figure 3.2a,b). The diabatic term, which is a mix of influences of climate forcings and elevation-induced circulation changes, is more spatially uniform except for the anomalous sign reversal near the Siple Coast and Siple Dome ice core site (Figure 3.2c).

As expected with any simple model applied to a complex system, there is a non-zero residual (Figures 3.2d and B.2d). Although the spatial pattern, magnitude, and sign of the residual varies greatly between ensemble members (Figure B.4), it remains small compared to the adiabatic and diabatic terms with the exception of the LASG-CESS model. We find that these resuduals can be largely explained by the different atmospheric hydrostatic equilibria in the LGM and PI simulations. For further discussion of this, refer to Appendix B. The small residuals are not unique to the Antarctic continent, the residual is small across the entire globe (Figure B.5d). The residual is, however, proportionally larger outside of the polar regions where LGM-to-PI temperature changes are much smaller.

3.4.2 Influences of Climate Forcings and Elevation on Temperature

The intermediate CESM simulation makes it possible to separate the effects of elevation change from the effects of climate forcings (Figure 3.2i–t). As expected, we find that elevation change accounts for the entire adiabatic term and that both climate forcings and elevation contribute to the diabatic term. Climate forcings have a more spatially uniform contribution to the diabatic term, while the contribution from elevation is more spatially variable. The elevation-induced variability in the diabatic term is caused by circulation changes as has been found in previous work (e.g., Steig et al., 2015) and as illustrated by the close alignment of the elevation-induced wind field and diabatic term (Figure B.6).

3.4.3 Paleoaltimetry Error Quantification

Applying the paleoaltimetry method (equation 3.2) to the ensemble of climate simulations shows that the estimated relative elevation change (Δdz) is significantly correlated with Δdz from the models (correlation coefficient of 0.57), but has a mean bias of -75 m (Figure B.7b). The bias is increasingly negative for larger relative elevation changes. Considering all pairs of points around Antarctica for all ensemble members, the errors range between -2240 and 1840 m, with a standard deviation of 337 m. For the ensemble mean, errors range from -1130 to 668 m, with a standard deviation of 161 m.

The magnitude of the largest errors is quite constant across Δdz values, leading to a signal-to-noise ratio (SNR) that tends to increase as the signal (Δdz) increases. This accounts for the lower bound on the SNR that increases with larger Δdz values (Figure B.7c). At a large enough Δdz, the SNR is consistently greater than 1, a transition which occurs at Δdz = 1840 m for the full ensemble of climate simulations and at Δdz = 941 m for the ensemble mean.

These error statistics are for all pairs of ice cores and other grid locations across Antarctica; however, the paleoaltimetry method is typically applied to pairs of locations that are thought *a priori* to have experienced the same climate (i.e., diabatic temperature) change (Grootes and Stuiver, 1986, 1987; Steig et al., 2001; Masson-Delmotte et al., 2011; Parrenin et al., 2013). To investigate whether any of the ice core sites (or averages over multiple sites) are representative of the continent's diabatic temperature change, we examine the errors for each pairing of sites. Site pairings with the lowest error mean and spread are those that are closest to each other (Figures B.8 and B.9). Otherwise, there are few pairs that stand out as optimal for estimating relative elevation change in Antarctica from the LGM to PI, and no one site stands out as most representative of the diabatic temperature change for all other sites. Siple Dome is distinctly not representative, which is consistent with it being the only location that shows diabatic cooling in the ensemble mean (Figure 3.2c) and with the findings from Steig et al. (2015) that show, when the West Antarctic ice sheet is lowered,

this region cools due to the increased advection of cold air from the East Antarctic plateau. Dome Fuji produces relatively low errors with other East Antarctic cores, while EPICA Dome C, despite being in East Antarctica, produces relatively low errors when paired with West Antarctic cores. Of the coastal cores, the pairing of Law Dome and Taylor Dome ice cores stand out from the rest, but no core site consistently pairs well with the coastal sites. Though the error mean and spread may be smaller for these pairings, the SNR is high only for location pairs that also have a large relative elevation change (Figure 3.3). For these simulations, that means pairs with one site in West Antarctica and one in East Antarctica.

3.4.4 Paleoaltimetry Error Attribution

Error in estimating Δdz arises when the diabatic temperature changes at each site are unequal (equation 3.4). In practice, a difference in the residual at the two sites also contributes to the error. The spatial variations in the diabatic term tend to be greater than in the residual for most models (Figure 3.2c,d), but some residual terms are both large in magnitude and spatially variable (Figure B.4). Thus, for most ensemble members and pairs of locations, the diabatic term has a larger contribution to the error, but for some models and location pairs there is also a sizeable contribution from the residual (Figure 3.4a–c).

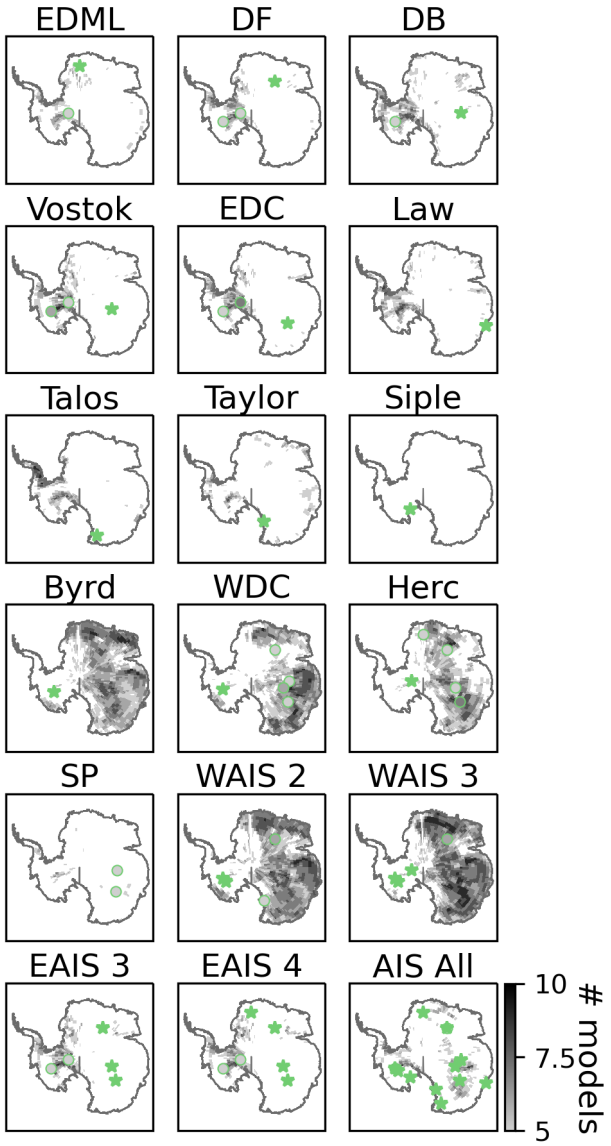

Figure 3.3: Signal-to-noise ratios (SNR) of the estimated relative elevation change. Each subplot shows errors for pairing each ice core and average over multiple ice cores – locations shown by green stars and names given in subplot titles (see table B.1 for long names) – with every other ice core and location around Antarctica. Green circles show the locations of cores that, if paired with the starred core or average, produce a SNR greater than 1.0 in five or more of the models (number of models that reach the threshold is shown by the grey shading inside the circle). Around the ice core locations, the grey shading shows how many models have an SNR greater than 3.0 when that site is paired with the starred ice core site or average. Shading is only shown if at least five models reach the SNR threshold.

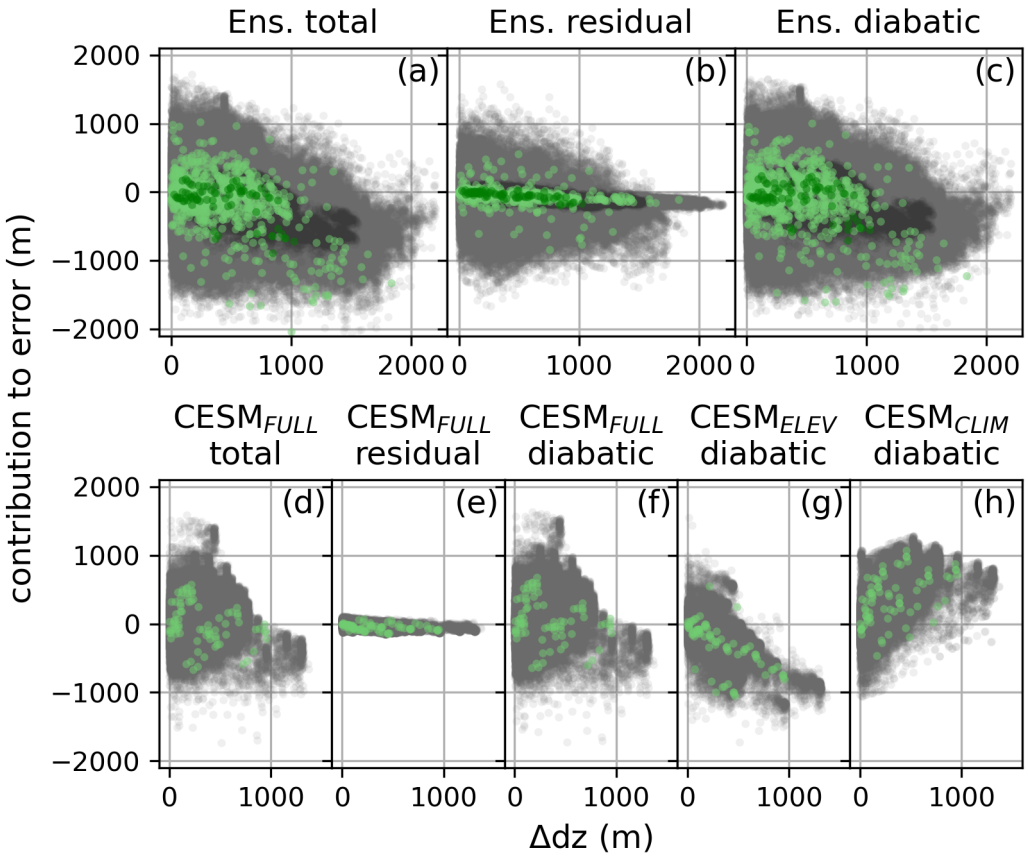

Figure 3.4: Attribution of error in estimates of relative elevation change. For the 10-member climate model ensemble, the full error (panel a) is broken down into the components due to the residual (b) and the diabatic term (c). For the $\text{CESM}_{\text{FULL}}$ ensemble member, the full error (d) is broken down into the components due to the residual (e) and the diabatic term (f). The diabatic error contribution is further broken down into the influence of the elevation change (g) and the influence of the climate forcings (h). The contributions to the error (y-axis) are plotted against the relative elevation change (Δdz). Green points are all pairings of ice cores and grey points are all pairings of all other locations (Figure 3.1). For panels (a)–(c), ensemble means are shown in darker shades of green and grey.

The three CESM simulations allow for a finer examination of the error by showing which parts of the error are due to elevation change and which are due to climate forcings. For these simulations, the spatial variability in the diabatic term is much greater than the variability in the residual (Figure 3.2k,l); the diabatic term explains nearly all of the error (Figure 3.4d–f). The diabatic variability arises from both elevation change and climate forcings.

Lowering of the surface elevation in West Antarctica drives an increased cyclonic circulation over that region resulting in diabatic cooling near the Siple Coast (and Siple Dome ice core) and diabatic warming in the Weddell Sea Sector (Figures 3.2o, B.6, and 3.1). Additional circulation-induced cooling occurs over the Peninsula and east of the Weddell Sea, while warming is seen across large areas of East Antarctica. The climate forcings have a different impact on the diabatic temperature change; they lead to warming everywhere, but this warming is especially pronounced just inland of the grounding line and in the whole of West Antarctica (Figure 3.2s).

Elevation and climate forcings also have different quantitative contributions to the error (Figure 3.4g,h). Elevation change explains much of the error structure and spread and leads to errors that are biased negative. The climate forcings lead to smaller but still significant errors that are biased positive. Thus, we find that elevation changes, and the resulting changes in atmospheric circulation, explain much of the error, but that climate forcings also contribute to the errors.

3.5 Discussion and Conclusion

In this paper, we investigate a widely-used, temperature-based paleoaltimetry method in a case study of Antarctica during the Last Glacial Maximum (LGM). Examining the thermodynamic assumptions behind this method shows that temporal temperature changes can be decomposed into the sum of adiabatic and diabatic changes. The validity of this decompostion is confirmed by the small residual that results from applying it to an ensemble of climate simulations. The residual is largely explained by the fact that the LGM and pre-industrial (PI) simulations have different atmospheric hydrostatic equilibria.

With the climate simulations, we also investigate the magnitude and source of uncertainty in this method. For our case study, we find a mean error of -75 m with a standard deviation of 337 m for relative elevation change; however, individual errors can be over a kilometer in either direction. These findings are consistent with previous error estimates found for different locations and different time periods (e.g., Forest et al., 1999). The leading source of

error arises from spatial variability in the diabatic temperature change. A set of simulations run with CESM allows us to separate the effects of elevation and climate forcings. We find that elevation change has a greater effect than climate change on the spatial variability of the diabatic term and thus on the magnitude of the error. The residual also contributes to the error, but it tends to be an order of magnitude smaller than the diabatic term.

The errors from this study must be considered within the context they were derived. Errors are likely to be even larger for real ice core data due to higher climate variability at spatial scales that are smaller than what is captured by the climate models. Additionally, in this study we do not consider error in the conversion from the original measurement to the temperature record (e.g., conversion of water isotopes to temperature discussed in Kahle et al. (2021)) nor the error associated with estimating the absolute elevation change at either site. Our error estimates are conservative in this respect. Last, we do not have a large variety of LGM ice sheet geometries in our ensemble nor do we filter the climate simulations based on how well they simulate Antarctic climate and capture near surface processes. The impact of these choices on our error estimates depends on whether each choice would lead to a more or a less spatially-variable diabatic term.

Overall, our findings suggest that the temperature-based paleoaltimetry method is likely to produce high errors and low signal-to-noise ratios (SNRs). For our case study of Antartica during the LGM, the relative elevation change of an ice core in East Antarctica versus one in West Antarctica was large enough to produce a SNR larger than one, and in some locations, larger than three (Figure 3.3). If the true relative elevation change between East and West was smaller than in our simulations, then the signal may not be large enough for an estimate from this paleoaltimetry method to be useful without additional information. Smaller ice-sheet-wide relative elevation changes, for example during the Holocene (e.g, Steig et al., 2001; Vinther et al., 2009), however, may lead to smaller circulation changes resulting in less spatial variability in the diabatic temperature change. Thus, there may be a tradeoff between large relative elevation changes leading to both greater signals and more noise. Elevation-induced circulation changes may be somewhat predictable, however, such that they could be

estimated and accounted for. Examining the signal-noise tradeoff and the predictability of circulation changes are areas for future work.

3.6 Data Availability

All output from PMIP3, PMIP4, CMIP5, and CMIP6 climate simulations (described in Table B.2) are available through the World Climate Research Programme (https://esgf-node.llnl.gov/projects/cmip5/ and https://esgf-node.llnl.gov/projects/cmip6/) (data for this paper accessed November 23, 2020 to July 21, 2021). The CESM simulations and scripts to create the figures will be made available through Zenodo. CESM is publicly accessible online (https://github.com/NCAR/iCESM1.2).

Chapter 4

EVALUATING THE CONSISTENCY OF THINNING AND ACCUMULATION-RATE HISTORIES AT THE WAIS DIVIDE ICE CORE SITE DURING THE LAST DEGLACIATION

Jessica A. Badgeley, Michelle R. Koutnik, and Eric J. Steig

4.1 Introduction

During the last deglaciation, ice core sites in the interior of West Antarctica warmed about 6°C more than ice core sites in the interior of East Antarctica (Cuffey et al., 2016; Kahle et al., 2021; Buizert et al., 2021). This temperature heterogeneity has been attributed to a difference in elevation change (Werner et al., 2018; Buizert et al., 2021); however, the magnitude of elevation changes remain uncertain, particularly for the WAIS Divide ice core site. For this site, the literature provides estimates ranging from no elevation change to over 500 m of surface lowering during the last deglaciation. This translates to estimates of ice thickness change that range from 0 to over 700 m, assuming isostatic equilibrium.

Direct evidence for ice thickness change comes from exposure dating of moraines and glacial erratics, which suggest that the interior of the West Antarctic ice sheet (WAIS) thickened after the Last Glacial Maximum (LGM) and reached a highstand of 100 to 200 m thicker-than-present in the early Holocene before thinning to the modern ice thickness around 7 ka BP (thousand years before 1950) (Ackert et al., 1999; Steig et al., 2001; Ackert et al., 2007, 2011, 2013; Spector et al., 2019). Temperature reconstructions from ice core proxies, total air content data from ice cores, and borehole temperature profiles all provide less direct constraints on ice elevation and thickness, but are co-located with the ice core site. Some of these constraints suggest an alternative history: ice was several hundred meters

thicker-than-present at the LGM before thinning to modern levels in the early Holocene (Werner et al., 2018; Buizert et al., 2021). Regional and global modeling studies support both hypothesized histories (e.g., Roy and Peltier, 2018; Pollard et al., 2016), leading to a lack of consensus on elevation and ice thickness change at the WAIS Divide ice core site during the last deglaciation. Section 4.2.2 provides a more detailed discussion of this literature.

The ice-column thickness history (also referred to as the thinning history throughout this paper) of a site influences the vertical velocity of the ice, which decreases with depth from the surface velocity to the melt rate at the base of the ice sheet. The basal melt rate varies across the ice sheet and is zero where the ice is frozen to the bed. The vertical velocity at the surface is determined by the accumulation rate, the basal melt rate, and ice-column thickness changes (e.g., Lliboutry, 1979). The vertical velocity profile as a function of depth is different depending on where it is located on the ice-sheet. At a divide, the vertical velocity decreases quickly in the upper part of the ice sheet and more slowly at depth. Over several ice thicknesses away from a divide, like at the WAIS Divide ice core site, which is about 24 km from the modern divide, the ice is in a flank-flow regime and the vertical velocity decreases approximately linearly with depth. Changes in vertical velocity with depth cause ice layers to strain by stretching horizontally and thinning vertically. Each packet of ice that starts at the surface will accumulate strain as it moves down through the ice column over time. The total accumulated vertical strain determines how much a single layer within the ice column thins from the time of deposition to when it is observed at depth in an ice core (ignoring firn compaction and densification).

The ice-column thinning history is thus connected to both the history of initial layer thicknesses and the final layer thicknesses at depth through the history of vertical velocity profiles and associated accumulated strain. Using a range of ice-column thinning histories of the past 20,000 years, we investigate whether they are glaciologically consistent with ice-equivalent accumulation rate reconstructions (the initial layer thicknesses) and annual layer thickness data (the final layer thicknesses) published for the WAIS Divide ice core site. If our findings suggest that the accumulation rates and annual layer thicknesses are

consistent with an ice sheet that was 300 to 500 m higher in the LGM, then they would also be consistent with the hypothesis that the differential East-West temperature change in Antarctica during the last deglaciation was due to elevation change. If our finding suggest the opposite, however, then the datasets are inconsistent with this hypothesis and we must reconsider the hypothesis, the datasets, or our glaciological assumptions.

4.2 Data

In this section, we present accumulation rate reconstructions, thinning histories, and annual layer thickness data that have been published for the WAIS Divide ice core site. The WAIS Divide ice core was collected from 2006 to 2011 at a site located in West Antarctica about 24 km to the West of the Ross-Amundsen ice divide (79.48°S and 112.11°W). At present, the site sits 1766 m above sea level where accumulation rates are about 22 cm/yr, the ice is 3465 m thick, and basal melt rates are about 1 cm/yr (Clow et al., 2012; WAIS Divide Project Members, 2013).

4.2.1 Accumulation Rate Reconstructions

The Fudge et al. (2016) accumulation rate reconstruction is calculated from annual layer thickness data and an estimate of the total accumulated vertical strain, which is derived from a one-dimensional thermomechanical ice-flow model. The model is calibrated against the measured borehole temperature data, δ^{15}N of N_2 constraints on firn thickness, and the annual layer thickness data. The accumulation rates reconstructed from the model are compared to results from an inverse approach that relies on δ^{15}N of N_2 data and a firn compaction model (Buizert et al., 2015). Fudge et al. (2016) estimate the uncertainties on their reconstruction to increase linearly from 0% in the modern to 16% at 20 ka BP.

Buizert et al. (2021) update the Fudge et al. (2016) estimates by adding constraints from Δage data (the difference between the gas and ice age) and estimating the reconstruction uncertainty using a Monte-Carlo approach, which leads to an ensemble of 1,000 accumulation rate reconstructions that are all consistent with the data within uncertainty.

In addition to the Fudge et al. (2016) reconstruction and the 1,000-member ensemble from Buizert et al. (2021), we include in our analysis the ensemble mean, minimum, and maximum (Figure 4.1). We smooth each of the 1,004 accumulation rate reconstructions using a low-pass Butterworth filter with a 1/1000 yr^{-1} cutoff frequency. If higher frequencies are included, then short-lived events that are unrelated to ice thickness changes can lead our analysis to show glaciological inconsistency between the datasets. The chosen cutoff frequency ensures that we focus our attention on multi-millennial timescales, which are most relevant for ice thickness and elevation changes. A different study focusing on the glaciological consistency of shorter timescale processes may want to include the higher frequencies.

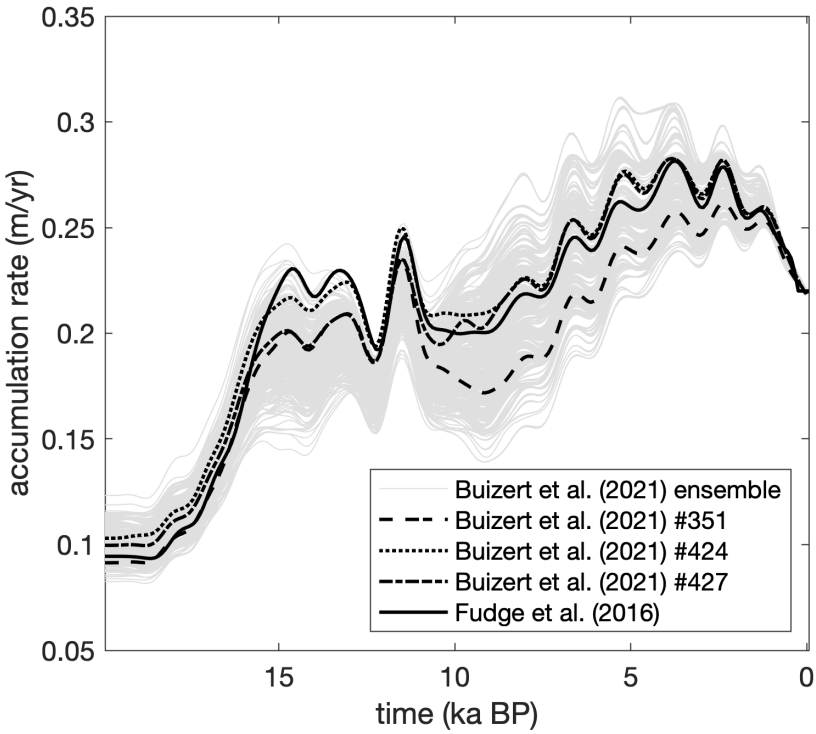

Figure 4.1: Accumulation rate reconstructions from Fudge et al. (2016) and Buizert et al. (2021) that are smoothed using a low-pass filter. Grey lines show the Buizert et al. (2021) ensemble members, mean, minimum, and maximum, while bold black lines highlight specific ensemble members that are referenced in later figures and the Fudge et al. (2016) reconstruction.

4.2.2 Thinning Histories

Previous studies have proposed a wide range of thinning and elevation histories for the WAIS Divide ice core site. The results of this previous work can be summarized into three generalized thinning histories: 1) little-to-no thinning from the LGM to present, 2) an ice sheet that was several hundred meters thicker in the LGM and subsequently thinned, and 3) ice thickened into the early Holocene, and then thinned. We refer to these literature-informed thinning histories as *No Thinning*, *Thinning Only*, and *Thickening-Thinning*, respectively (Figure 4.2).

The *No Thinning* history maintains the modern ice thickness throughout the deglaciation. The *Thinning Only* history starts with a thicker ice column, thins rapidly in the early Holocene, and reaches a near-modern ice thickness around 7 to 5 ka BP. The *Thickening-Thinning* history starts with the modern ice thickness, begins to thicken around 17 ka BP in tandem with the accumulation rate increase (Fudge et al., 2016), reaches a peak thickness in the early Holocene, and thins to a near-modern ice thickness by 7 to 5 ka BP. For the *Thinning Only* and *Thickening-Thinning* histories, we examine the impact of five maximum thickness anomalies of 60, 125, 250, 350, and 500 m on our results. In addition to the highstand, we also examine the uncertainty in the timing of the thinning by shifting each history forwards and backwards in time by 500 and 1,000 years.

In the rest of this section, we provide details on the work that motivates our choice of thinning histories, including the timing of the thinning and the maximum thickness anomalies. For studies that address elevation rather than thickness change, we reconstruct changes in thickness by assuming two end-member scenarios: 1) the bed is rigid such that thickness change equals elevation change and 2) the bed is in isostatic equilibrium with the ice sheet such that thickness change is equal to about 140% of the elevation change, assuming a mantle density of 3,300 kg/m^3.

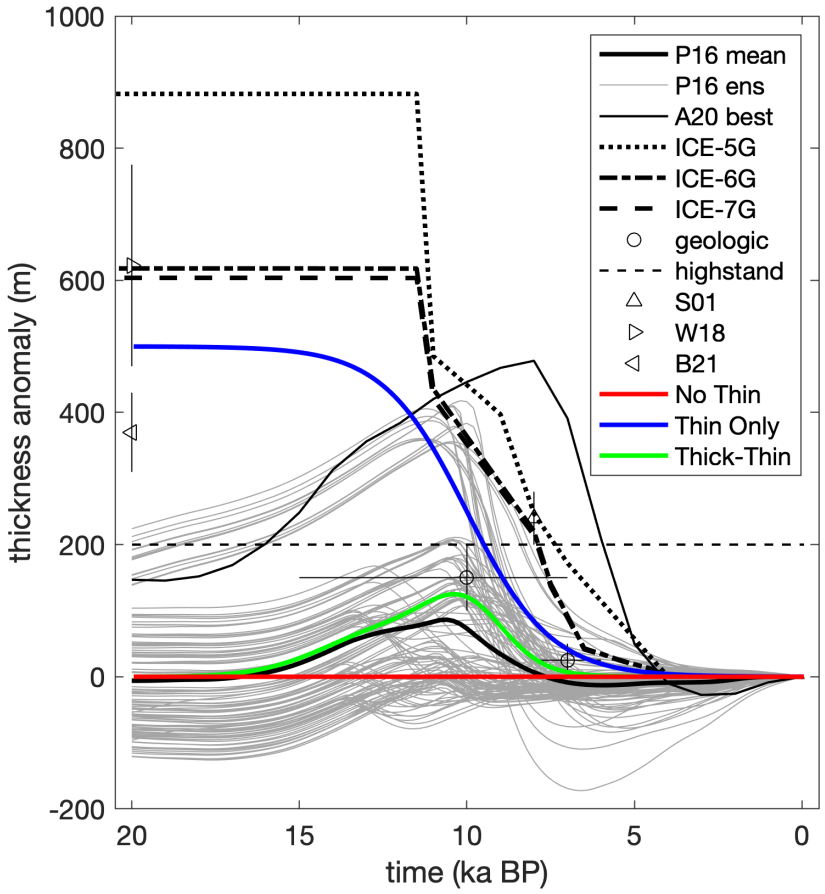

Figure 4.2: Selected thinning histories for the WAIS Divide ice core site given as thickness anomalies relative to present. P16 mean is the score-weighted mean of the best-fit ensemble from Pollard et al. (2016) and the P16 ens lines are the 120 individual ensemble members. A20 best is the best-scoring ensemble member from Albrecht et al. (2020). ICE-5G, ICE-6G, and ICE-7G are the reconstructions from Peltier (2004), Peltier et al. (2015), and Roy and Peltier (2018), respectively. The empty circles, corresponding uncertainty bars, and lightweight dashed line summarize results from the glacial geologic data presented in Ackert et al. (1999), Ackert et al. (2007), Ackert et al. (2011), Ackert et al. (2013), and Spector et al. (2019). S01 shows the amount of Holocene thinning experienced at the Byrd ice core site as estimated in Steig et al. (2001). W18 shows the range of LGM thickness estimates from Werner et al. (2018), while B21 shows the range from Buizert et al. (2021). No Thin, Thin Only, and Thick-Thin are the *No Thinning*, *Thinning Only*, and *Thickening-Thinning* histories from this study that are scaled to maximum thickness anomalies of 0, 500, and 125 m, respectively.

Direct Evidence for Ice Thickness Change

In the interior of the West Antarctic ice sheet (WAIS) near divides yet still hundreds of kilometers from the WAIS Divide ice core site, exposure dates from moraines and glacial erratics on nunataks suggest that the ice sheet reached a maximum thickness anomaly of about 100 to 200 m in the early Holocene (Ackert et al., 1999, 2007, 2011, 2013; Spector et al., 2019). Mt. Waesche is near the Ross-Getz-Amundsen divide and is the closest of these studied nunataks to the divide that crosses near the ice core site. Geologic data from Mt. Waesche indicate that the ice was 45 to 85 m thicker during the highstand around 10 ka BP (Ackert et al., 1999, 2013). The Whitmore Mountains are closer to the ice core site, but lie on the Ross-Weddell divide. Data from there suggest ice was no more than 190 m thicker in the last 30,000 years with additional constraints suggesting that this highstand occurred in the last 15,000 years (Spector et al., 2019). The Ohio Range is near the same divide but is closer to the grounding line. It shows multiple highstands, all of which occur during transitions into interglacial periods. The most recent highstands were around 10 ka BP and 130 ka BP, both of which had ice up to 125 m thicker than today (Ackert et al., 2007, 2011).

These geologic constraints suggest a WAIS that thickened into the early Holocene and subsequently thinned. At the Whitmore Mountains and other nunataks around the Ross Sea sector, Spector et al. (2019) infer that modern ice levels were reached around or just after 7 ka BP. This inferred thinning history is different from the retreat of the grounding line in the Ross Sea embayment, which is thought to have thinned monotonically from at least 14 ka BP and ending around 7 ka BP (Spector et al., 2017; Goehring et al., 2019). Ice in the interior WAIS was likely not in equilibrium with the margins during the LGM (Ackert et al., 1999; Todd et al., 2010; Ackert et al., 2013). This disequilibrium, along with the increase in accumulation rates during the deglaciation, may have led to a thickening in the interior while the margins thinned. The increased accumulation rates alone had the potential to cause over 600 m of thickening from 18 to 10 ka BP at the WAIS Divide ice

core site (Fudge et al., 2016) if one assumes an ice sheet in equilibrium at 18 ka BP and no change in ice dynamics. A wave of thinning triggered by the grounding line retreat may have then propagated inland, outpacing the thickening and leading to net thinning in the early and mid-Holocene (Ackert et al., 1999; Steig et al., 2001; Todd et al., 2010; Spector et al., 2019). This history is inferred from data at nunataks that are on divides other than the Ross-Amundsen divide and/or are located hundreds of kilometers away from the WAIS Divide ice core site (Spector et al., 2019).

Interpretations from Ice Core Data

Data from the WAIS Divide ice core and borehole do not provide as direct of constraints on the ice thickness. Here, we discuss three types of data and associated methods that have been used to estimate thickness or elevation change during the last deglaciation: temperature proxies, total air content, and borehole temperature profiles.

One method, also applied broadly in the paleoaltimetry community, assumes that the spatial pattern in temperature change can be explained by differential elevation change (Meyer, 2007, and references therein). The differential elevation change can then be directly estimated from temperature reconstructions (or proxy records) or can be inferred by comparing to climate model simulations. Steig et al. (2001) directly compare measurements of the oxygen isotopes of ice (δ^{18}O), which is a temperature proxy, from the Taylor Dome and Byrd ice core sites, the latter of which is close to the WAIS Divide site. Assuming an isotope-temperature relationship and a temperature lapse rate, they estimate that the Byrd site experienced about 200 m of elevation loss, or 200 to 280 m of thinning, from 8,000 years ago to present.

Werner et al. (2018) compare δ^{18}O records from ice cores around Antarctica to δ^{18}O output from climate simulations that use variable topographic congurations for the Antarctic ice sheet at the LGM, taken from ice sheet and glacial isostacy models, as boundary conditions. With the simulations, they find a δ^{18}O-elevation relationship that they use to reconstruct LGM-to-present elevation change. They conclude that the WAIS Divide site was 470 to 560

m higher at the LGM. Converting elevation change to thickness change, this suggests the WAIS Divide site was 470 to 775 m thicker at the LGM.

Buizert et al. (2021) similarly compare proxy-based temperature reconstructions from Antarctic ice cores to modeled LGM temperatures simulated using a variety of Antarctic ice sheet boundary conditions. They conclude that the WAIS Divide ice core site was about 310 m higher and that the interior East Antarctic ice sheet (EAIS) was about 110 m lower during the LGM. Converting to thickness, this translates to the interior WAIS being 310 to 430 m thicker at the LGM. This finding, however, is based on the average temperaure of five climate simulations and average elevation of five ice sheet reconstructions, which potentially compromises the glaciological accuracy of the ice sheet reconstructions as well as the relationship between the climate model boundary conditions (the ice sheet reconstructions) and temperature outputs.

Buizert et al. (2021) support their findings with total air content (TAC) measurements, from which they estimate a relative elevation change between interior East and West Antarctica of 420 m (full range of 280 to 590 m). Combined with their temperature-based elevation estimates for the individual ice core sites, this gives a range of 170 to 820 m thicker ice in the LGM at the WAIS Divide ice core site. Early work, including Raynaud and Whillans (1982), suggested that TAC could be used to estimate elevation because of the relationship between TAC and pressure and temperature, both of which depend, in part, on elevation. Raynaud and Whillans (1982) interpreted TAC from the Byrd ice core to indicate 200 to 250 m of increasing surface elevation at the end of the last glacial period followed by little-to-no elevation change during the Holocene. More recently, many studies have found that elevation estimates from TAC are highly uncertain because pressure can vary independently of elevation change and TAC also depends strongly on processes related to firn densification and bubble close-off (Krinner et al., 2000; Raynaud et al., 2007; Eicher et al., 2016). Buizert et al. (2021) argue that many of these complications cancel out to the first order if relative elevation changes are considered.

To model the borehole temperature profile for the WAIS Divide ice core site, a thinning

history and several other ice sheet parameters must be assumed. Cuffey et al. (2016) assume 150 m of thickening from 18 to 15 ka BP followed by 50 m of thinning and find a good fit to the borehole temperature data. They also explore several other thinning histories including one that has no thickness change and one that has a highstand in the LGM followed by thinning from 12 to 5 ka BP. They find that the timing and magnitude of the thinning affect the interpretation of the borehole temperature profile; however, they do not specify how each thinning history alters the model fit to the data.

Interpretations from Continent to Global-Scale Data and Modeling

Another approach to estimating past elevation changes is to rely on a compilation of data from around Antarctica or around the world. The two approaches I discuss here use data compilations for boundary conditions, tuning, and/or evaluation of 1) a global glacial isostatic adjustment and sea level model and 2) a contient-scale ice-flow model.

The paleo ice sheet reconstructions, ICE-5G (VM2), ICE-6G (VM5a), and ICE-7G_NA (VM7), are all derived using an inverse approach to fit a glacial isostatic adjustment and sea level model to observations of relative sea level change (Peltier, 2004; Peltier et al., 2015; Roy and Peltier, 2018). The model includes the effects of ice sheets on the Earth's rotation, shape, and gravitational field, all of which influence spatial variations in sea level. To constrain and validate the ice sheet reconstructions and resulting sea levels, Peltier (2004) relies on the best available estimates of the past extent of ice sheets and the magnitude of past eustatic sea level change as well as radio-carbon dated relative sea level curves that span the LGM to today. Peltier et al. (2015) and Roy and Peltier (2018) incorporate updated versions of those datasets along with global positioning system (GPS) data, gravity measurements from land and satellites, and glacial geologic data that indicate ice sheet thickness. Though the reconstructions are continually improving with updated and new datasets, the solutions to the inverse problem are not fully constrained. Antarctica in particular has proved difficult to reconstruct because the continent is almost entirely ice-covered and data from around the edges are not necessarily representative of the interior (Roy and Peltier, 2018).

The thinning history of the WAIS Divide ice core site has a similar shape and timing across the ICE-5G (VM2), ICE-6G (VM5a), and ICE-7G_NA (VM7) reconstructions (hereafter shortened to ICE-5G, ICE-6G, and ICE-7G, respectively). In each, the ice is much thicker from the LGM until the beginning of the Holocene when it undergoes a rapid rate of thinning (Figure 4.2). Around 4 ka BP, the ice reaches the modern thickness. The primary difference between the reconstructions is the thickness of the ice at the LGM. For ICE-5G, the ice is 880 m thicker, while for ICE-6G and ICE-7G, the ice is 620 and 600 m thicker, respectively.

Many other reconstructions of Antarctica during the last deglaciation are based on Antarctic data compilations and ice-flow models (Whitehouse et al., 2012; Briggs and Tarasov, 2013; Briggs et al., 2014; Chang et al., 2016; Pollard et al., 2016; Albrecht et al., 2020). Many of these studies rely on similar models, methods, and datasets. Using a three-dimensional model, many of these studies create an ensemble of ice-sheet simulations by varying a suite of uncertain model parameters. Each ensemble member is then given a score based on how well it matches paleo and modern data. The method for computing scores varies by study, but tends to fall within one of two categories. The most common scoring method relies on averaging mists between the model and data with varying degrees of consideration for data uncertainty, representativeness, and distribution (Whitehouse et al., 2012; Briggs and Tarasov, 2013; Briggs et al., 2014; Pollard et al., 2016; Albrecht et al., 2020), while more sophisticated approaches use Bayesian statistical techniques (e.g., Chang et al., 2016; Pollard et al., 2016).

We focus here on the results from the Pollard et al. (2016) study becuase they use two methods common to the other studies and their results agree well with the glacial geologic data from nunataks around West Antarctica (Spector et al., 2019). The score-weighted mean of the 120 best-fit ensemble members has an LGM thickness similar to today. The ice begins to thicken around 17 ka BP until it reaches a maximum thickness anomaly of 86 m at 10.6 ka BP after which it thins to near-modern ice levels by 7.6 ka BP. The best-fit ensemble, however, includes widely-varying thinning histories with thicknesses that are -100 to +200 m at the LGM and reach peaks of 0 to 420 m between 13.6 and 0 ka BP (Figure 4.2). At

least three of the ensemble members are thinner-than present from the LGM through the late Holocene, which is not a scenario we consider in this study.

4.2.3 Annual Layer Thickness Data

The WAIS Divide annual layer thickness dataset for the last 20,000 years is derived directly from the annually-resolved depth-age scale (Sigl et al., 2016). We assign an age to each layer by averaging the ages at the start and end of the layer. We then smooth the annual layer thicknesses using the same method as for the accumulation rate reconstructions: a low-pass Butterworth filter with a 1/1000 yr^{-1} cutoff frequency (Figure 4.3).

Uncertainties for the annual layer thickness data are about 1% for 15 ka BP to present and 3% for 31 to 15 ka BP (Sigl et al., 2016; Fudge et al., 2016). These uncertainties arise from the methods used to create the depth-age scale: visual and automated counting of annual cycles and tie points to other dated proxy records. About one in one hundred years are thought to be miscounted for the Holocene after combining the results of visual and automated annual layer counts based on geochemical and physical properties (Sigl et al., 2016). Prior to 15 ka BP, the number of miscounted layers likely increases as the annual cycle is increasingly difficult to decipher and the number of methods that can be used to count the layers and quantify the uncertainty is limited. Because we focus on the long timescale (>100-year) changes in the annual layer thickness data, we also consider the contribution of the tie points to the overall uncertainty. Over longer time periods, the tie points to other proxy records act to reduce the uncertainty in the depth-age scale (Sigl et al., 2016).

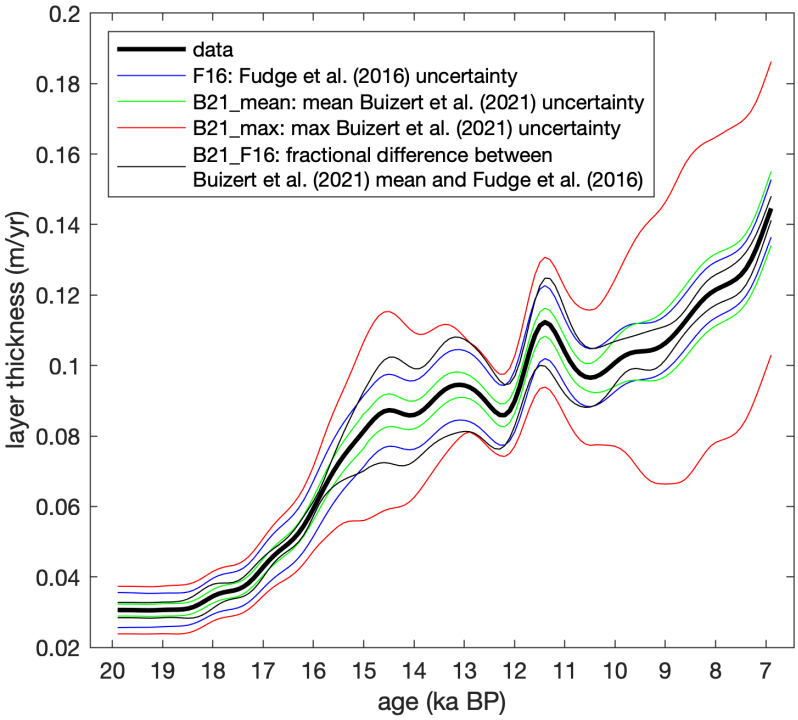

Figure 4.3: Annual layer thickness data and evaluation bounds to determine model-data fit. All evaluation bounds are based on the annual layer thickness and accumulation rate uncertainties. We test four estimates of the accumulation rate uncertainty to determine the sensitivity of our results to this choice. 'F16' are the bounds based on the uncertainty in the Fudge et al. (2016) accumulation rate reconstruction. 'B21_mean' and 'B21_max' are based on the mean and maximum percent difference between the Buizert et al. (2021) reconstruction ensemble mean and members. 'B21_F16' is based on the percent difference between the Buizert et al. (2021) ensemble mean and Fudge et al. (2016) reconstructions.

4.3 Methods

To test the glaciological consistency of the accumulation rate reconstructions and thinning histories with the annual layer thickness data, we use a simple ice-flow model that captures the key processes and is computationally inexpensive enough to allow for exploration of the uncertainties. In the following section, we describe the model, the parameter uncertainty exploration, and the metrics we use to compare the model results to the annual layer thickness data.

4.3.1 Model

We use a one-dimensional model that advects ice vertically from the surface towards the bed (WAIS Divide Project Members, 2013, personal communication with Tyler J. Fudge). At each time step a new particle (representing an ice layer of a certain age) is added to the surface. The model then calculates the vertical velocities for every particle using equation 4.1, which allows it to estimate the new position of the particles. It calculates the vertical velocities again at the estimated new position and takes the average of the two velocities. It is this average velocity that is used to compute the final position of the particle at the end of each 100-year time step. After 20,000 years, we have the simulated depth-age scale from which annual layer thicknesses can be calculated.

The vertical velocity profile ($\omega(\hat{z}, t)$) is calculated using the Lliboutry (1979) approximation:

$$\omega(\hat{z}, t) = -\dot{m}(t) - \psi(\hat{z}, t)(\dot{b}(t) - \dot{m}(t) - \dot{H}(t)) \tag{4.1}$$

where t is time, $\dot{m}$ is the basal melt rate, $\dot{H}$ is the thinning rate, $\hat{z}$ is normalized depth:

$$\hat{z} = 1 - \frac{z}{H} \tag{4.2}$$

z is elevation, H is the ice thickness, ψ is the approximated shape of the vertical velocity profile:

$$\psi = 1 - \frac{p+2}{p+1}\hat{z} + \frac{1}{p+1}\hat{z}^{p+2} \tag{4.3}$$

and p is the shape parameter that determines whether the vertical velocity flow regime is more like a divide site ($-1 < p \lesssim 1$) or a flank site ($4 \lesssim p$) (e.g., Fudge et al., 2019). At a divide, the velocity drops off quickly in the top of the ice column and more slowly at depth, while at a flank site, like the WAIS Divide ice core site, the velocity changes linearly with depth (Figure 4.4).

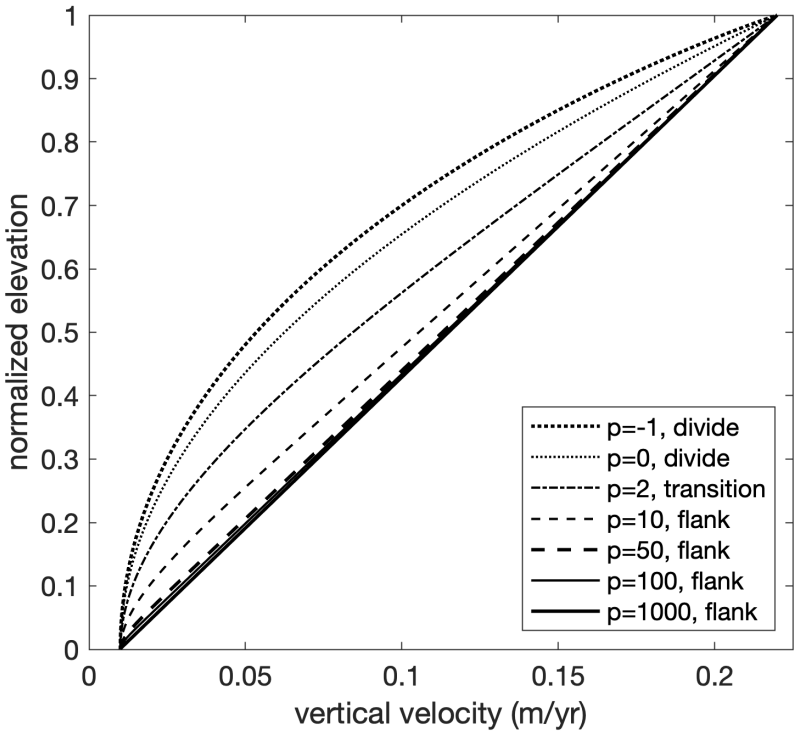

Figure 4.4: Example vertical velocity profiles for the WAIS Divide ice core site using the Lliboutry approximation (Lliboutry, 1979). The p value determines the shape of the vertical velocities with lower p values (-1 $< p \lesssim$ 1) giving more divide-like conditions, middle values (1 $\lesssim p \lesssim$ 4) giving a transitional flow regime, and higher values (4 $\lesssim p$) giving flank-flow conditions (e.g., Fudge et al., 2019).

4.3.2 Parameter Uncertainty Exploration

To capture a plausible range in the model parameters, we vary the basal melt rate and the shape of the vertical velocity profile. For the basal melt rate, we use values of 0, 0.001, 0.005, and 0.01 m/yr, the minimum and maximum values of which are based on the range in Koutnik et al. (2016). For the velocity shape parameter, p, we use values of 10, 50, 100, and 1000, which are all appropriate for a flank flow site (e.g., Fudge et al., 2019). We only test flank-flow values because the WAIS Divide ice core site is far, several ice thicknesses, from the modern divide. We do not test values less than 10 because they do not provide any good fits to the layer thickness data. We have no *a priori* expectations for how the basal

melt rate and the shape of the vertical velocity profile may have changed through time, so we assume they are constant. Uncertainty in the accumulation rates are explored using the 1,004-member ensemble (described in section 4.2.1) and is included in the evaluation bounds (described below in section 4.3.3). Uncertainty in the thinning rates are explored using the literature-informed thinning histories and variations in the maximum thickness anomaly ($maxH$) and timing (dt) described in section 4.2.2.

4.3.3 Evaluation Metrics

To determine which parameter combinations lead to simulated annual layer thicknesses that are most consistent with the data, we input every combination of the above-described parameters into the model (for a total of 1,204,800 simulations) and determine if the model output fits within pre-determined evaluation bounds for the period 20 to 7 ka BP. This evaluation time period was chosen for several reasons: 1) it is the period when much of the thinning occurs in our literature-informed thinning histories, 2) for a given accumulation rate history, the 7 to 0 ka BP period tends to be relatively insensitive to which thinning history is used, and 3) the deglacial period is the focus of this study. We also compute the root mean squared error (RMSE) between the modeled annual layer thicknesses and the data for the same time period. The RMSE is only used in the analysis of the model results and does not determine which model results are analyzed.

Evaluation bounds used to determine the ensemble of model results that provide a reasonable fit to the data. These evaluation bounds are determined by the uncertainties associated with the annual layer thickness data and the accumulation rate reconstructions (Figure 4.3). We add the two uncertainties in quadrature to create the evaluation bounds. Though the accumulation rate uncertainty is partially captured by the ensemble of 1,004 reconstructions, the uncertainty in each individual reconstruction impacts the range of initial layer thicknesses it represents. The uncertainty in the initial layer thickness translates to a proportional uncertainty in the final annual layer thickness. Thus, we can capture the accumulation rate uncertainties by including them in the evaluation bounds for the annual layer thickness data.

The accumulation rate uncertainties vary between the Fudge et al. (2016) and Buizert et al. (2021) reconstructions, so we consider four estimates of the uncertainty in order to test the sensitivity of our results to this choice. The evaluation bounds based on the Fudge et al. (2016) uncertainty, which linearly increases from 0% at the present to about 16% at 20 ka BP, are called the 'F16' bounds. For the Buizert et al. (2021) reconstruction, we find the mean and maximum percent difference between the ensemble mean and each of the ensemble members. These two bounds are called the 'B21_mean' and 'B21_max' bounds. A fourth set of bounds, called 'B21_F16', is created based on the fractional difference between the Buizert et al. (2021) ensemble mean and Fudge et al. (2016) reconstructions.

4.4 Results

4.4.1 Sensitivity to Choice of Evaluation Bounds

The primary effect of the choice of evaluation bounds is the size of the ensemble of model results that fit within the bounds (Tables 4.1 and 4.2). The B21_max bounds allow for the largest ensemble of 475,000, which is one and two orders of magnitude larger than for the F16 and B21_F16 bounds, respectively, which allow for the next largest ensembles. The B21_ens bounds lead to the smallest total ensemble size of just 127 members. The main conclusions of this work concerning the thinning histories, however, are robust to the choice of bounds. In the remaining results sections, we report our findings for the B21_max bounds, unless otherwise stated, because they are the most conservative estimate of the evaluation bounds, producing the largest ensemble.

4.4.2 Normalized Thinning Histories

We subset the ensembles of model results into one for each literature-informed thinning history, *No Thinning*, *Thinning Only*, and *Thickening-Thinning* (Tables 4.1 and 4.2). The *No Thinning* history has the largest ensemble for all four evaluation bounds. The *No Thinning* history is unaffected by the maximum thickness anomaly and timing shift parameters, but

even accounting for this, the *No Thinning* history allows for the largest number of model results to fit within the evaluation bounds. The other two thinning histories have similarly-sized ensembles despite the evaluation bounds, but in general the *Thickening-Thinning* history has the slightly larger ensemble size (with the exception of the B21_F16 bounds).

Bounds	**B21_max**			**F16**		
Thinning History	**No Thin**	**Thin Only**	**Thick-Thin**	**No Thin**	**Thin Only**	**Thick-Thin**
Ens. Size (#)	244,275	95,859	134,755	9,150	1,741	1,853
Ens. Size (%)	61	24	34	2.3	0.43	0.46
Unique ARs	946	911	931	118	75	80
Most Common AR	multiple	B21 #351	B21 #351	F16	F16	B21 #424

Table 4.1: Summary of the ensemble of model results that fit within the evaluation bounds B21_max and F16. All evaluation bounds are based on the annual layer thickness and accumulation rate uncertainties. The B21_max bounds are based on the maximum percent difference between the Buizert et al. (2021) accumulation rate reconstruction ensemble mean and members, while the F16 bounds are based on the uncertainty in the Fudge et al. (2016) reconstruction. The ensembles are separated by the literature-informed thinning histories, which are *No Thinning* (No Thin), *Thinning Only* (Thin Only), and *Thickening-Thinning* (Thick-Thin). The ensemble size is reported in both absolute size (#) and percent size (%) of the 401,600 total number of model simulations run. The last two rows give the number of unique accumulation rate reconstructions (ARs) for each ensemble and accumulation rate that occurs most frequently. The Fudge et al. (2016) accumulation rate reconstruction is indicated by F16, while individual Buizert et al. (2021) reconstructions are indicated by B21 followed by the ensemble member number.

Bounds	**B21_F16**			**B21_mean**		
Thinning History	**No Thin**	**Thin Only**	**Thick-Thin**	**No Thin**	**Thin Only**	**Thick-Thin**
Ens. Size (#)	3,025	738	565	100	11	16
Ens. Size (%)	0.75	0.18	0.14	0.025	0.0027	0.0040
Unique ARs	44	37	33	1	1	1
Most Common AR	multiple	B21 #424	B21 #427	F16	F16	F16

Table 4.2: Same as Table 4.1 but for the evaluation bounds B21_F16 and B21_mean. The B21_mean bounds are based on the mean percent difference between the Buizert et al. (2021) accumulation rate reconstruction ensemble mean and members, while the B21_F16 bounds are based on the percent difference between the Buizert et al. (2021) ensemble mean and Fudge et al. (2016) reconstructions.

4.4.3 Accumulation Rate Reconstructions

The Fudge et al. (2016) accumulation rate reconstruction appears in each ensemble no matter the evaluation bounds or the thinning history. This is because it is the only reconstruction that allows for simulated annual layer thicknesses to fit within the narrow B21_mean evaluation bounds. The other most common accumulation rate reconstructions in the ensembles are members #351, #424, and #427 from the Buizert et al. (2021) reconstructions (Figure 4.1).

The Fudge et al. (2016) accumulation rates not only show up frequently in the ensembles, but they also tend to lead to the lowest RMSEs between the simulated and data annual layer thicknesses (Figure 4.5 second row). By splitting up the RMSEs of each ensemble into five bins, we see that the Fudge et al. (2016) accumulation rates are the only ones in the lowest RMSE bin. The second-lowest RMSE bin is also dominated by the Fudge et al. (2016) reconstruction, but it also includes reconstructions from Buizert et al. (2021).

Therefore, the Fudge et al. (2016) accumulation rate reconstruction provides some of the best fits to the annual layer thickness data. This is likely because it was derived from that data. The Buizert et al. (2021) accumulation rates were similarly derived, but were adjusted to fit δ^{15}N of N_2 and Δage constraints. This does not necessarily mean the Buizert et al. (2021) reconstructions are less accurate, but instead may indicate that they are capturing processes not described by our one-dimensional model.

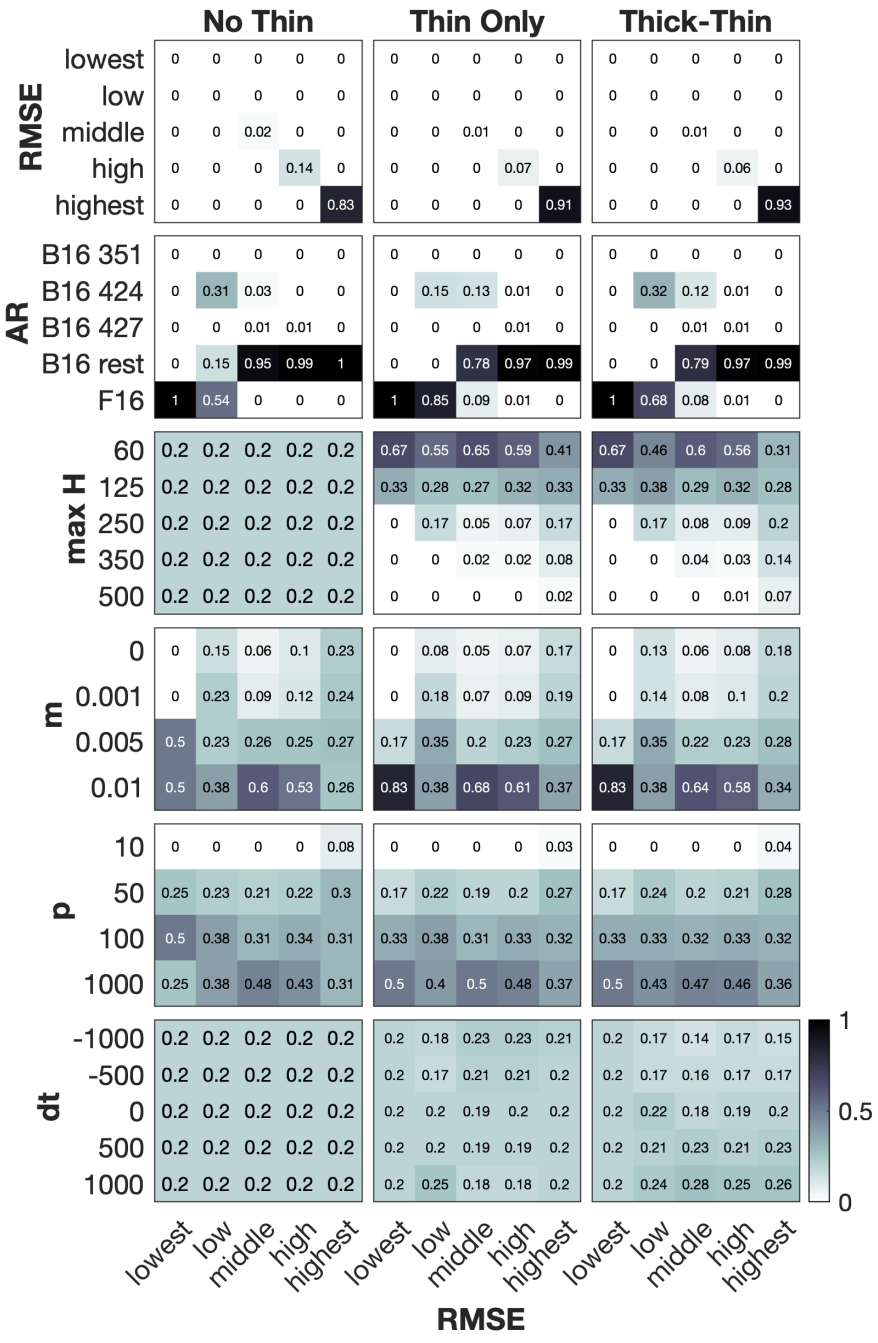
No Thin
Thin Only
Thick-Thin
RMSE
lowest 0 0 0 0 0 | 0 0 0 0 0 | 0 0 0 0 0
low 0 0 0 0 0 | 0 0 0 0 0 | 0 0 0 0 0
middle 0 0 0.02 0 0 | 0 0 0.01 0 0 | 0 0 0.01 0 0
high 0 0 0 0.14 0 | 0 0 0 0.07 0 | 0 0 0 0.06 0
highest 0 0 0 0 0.83 | 0 0 0 0 0.91 | 0 0 0 0 0.93
AR
B16 351 0 0 0 0 0 | 0 0 0 0 0 | 0 0 0 0 0
B16 424 0 0.31 0.03 0 0 | 0 0.15 0.13 0.01 0 | 0 0.32 0.12 0.01 0
B16 427 0 0 0.01 0.01 0 | 0 0 0 0.01 0 | 0 0 0.01 0.01 0
B16 rest 0 0.15 0.95 0.99 1 | 0 0 0.78 0.97 0.99 | 0 0 0.79 0.97 0.99
F16 1 0.54 0 0 0 | 1 0.85 0.09 0.01 0 | 1 0.68 0.08 0.01 0
max H
60 0.2 0.2 0.2 0.2 0.2 | 0.67 0.55 0.65 0.59 0.41 | 0.67 0.46 0.6 0.56 0.31
125 0.2 0.2 0.2 0.2 0.2 | 0.33 0.28 0.27 0.32 0.33 | 0.33 0.38 0.29 0.32 0.28
250 0.2 0.2 0.2 0.2 0.2 | 0 0.17 0.05 0.07 0.17 | 0 0.17 0.08 0.09 0.2
350 0.2 0.2 0.2 0.2 0.2 | 0 0 0.02 0.02 0.08 | 0 0 0.04 0.03 0.14
500 0.2 0.2 0.2 0.2 0.2 | 0 0 0 0 0.02 | 0 0 0 0.01 0.07
m
0 0 0.15 0.06 0.1 0.23 | 0 0.08 0.05 0.07 0.17 | 0 0.13 0.06 0.08 0.18
0.001 0 0.23 0.09 0.12 0.24 | 0 0.18 0.07 0.09 0.19 | 0 0.14 0.08 0.1 0.2
0.005 0.5 0.23 0.26 0.25 0.27 | 0.17 0.35 0.2 0.23 0.27 | 0.17 0.35 0.22 0.23 0.28
0.01 0.5 0.38 0.6 0.53 0.26 | 0.83 0.38 0.68 0.61 0.37 | 0.83 0.38 0.64 0.58 0.34
p
10 0 0 0 0 0.08 | 0 0 0 0 0.03 | 0 0 0 0 0.04
50 0.25 0.23 0.21 0.22 0.3 | 0.17 0.22 0.19 0.2 0.27 | 0.17 0.24 0.2 0.21 0.28
100 0.5 0.38 0.31 0.34 0.31 | 0.33 0.38 0.31 0.33 0.32 | 0.33 0.33 0.32 0.33 0.32
1000 0.25 0.38 0.48 0.43 0.31 | 0.5 0.4 0.5 0.48 0.37 | 0.5 0.43 0.47 0.46 0.36
dt
-1000 0.2 0.2 0.2 0.2 0.2 | 0.2 0.18 0.23 0.23 0.21 | 0.2 0.17 0.14 0.17 0.15
-500 0.2 0.2 0.2 0.2 0.2 | 0.2 0.17 0.21 0.21 0.2 | 0.2 0.17 0.16 0.17 0.17
0 0.2 0.2 0.2 0.2 0.2 | 0.2 0.2 0.19 0.2 0.2 | 0.2 0.22 0.18 0.19 0.2
500 0.2 0.2 0.2 0.2 0.2 | 0.2 0.2 0.19 0.19 0.2 | 0.2 0.21 0.23 0.21 0.23
1000 0.2 0.2 0.2 0.2 0.2 | 0.2 0.25 0.18 0.18 0.2 | 0.2 0.24 0.28 0.25 0.26
1
0.5
0
lowest low middle high highest lowest low middle high highest lowest low middle high highest
RMSE

Figure 4.5: Root mean squared errors (RMSEs) of the ensembles of model results that fit within the B21_max evaluation bounds. Each plotted value and the associated shading shows the fractional frequency of the occurance of the x- and y-values in the ensemble of results for the *No Thinning* (No Thin), *Thinning Only* (Thin Only), and *Thickening-Thinning* (Thick-Thin) thinning histories. The top row is akin to a histogram of the RMSEs in each ensemble, such that the values within each bounded box sum to one. In rows two through six, each column of each bounded box sums to one, such that the columns are interpreted as histograms of the y-values for a given range of RMSEs (the x-values). The RMSE bins are associated with the following values: lowest = (-infinity, 0.0015], low = (0.0015, 0.003], middle = (0.003, 0.0045], high = (0.0045, 0.006], and highest = (0.006, infinity). AR are the accumulation rate reconstructions, where B16 followed by a number stands for the ensemble member from Buizert et al. (2021) and F16 refers to the Fudge et al. (2016) reconstruction. $maxH$ is the maximum thickness anomaly in meters that is reached in the thinning history. m is the basal melt rate in m/yr. p is the parameter determining the shape of the vertical velocity profile, where larger values are more indicative of a flank-flow regime (Figure 4.4). dt is the shift in the thinning history timing in years, where positive values refer to a forward shift in time and negative values are a backwards shift.

4.4.4 Parameter Combinations

Though there is a lot of information contained within the size of the ensemble of results that fit within the evaluation bounds, even more can be learned by looking at the parameter combinations that go into those results. Here we show which parameter values and combinations show up most frequently in the ensembles for the three thinning histories (Figures 4.6 through 4.8) and whether certain parameter values tend to lead to a larger or smaller RMSEs (Figure 4.5).

The maximum thickness anomaly ($maxH$) exerts a strong control on whether a model result fits within the evaluation bounds for the *Thinning Only* and *Thickening-Thinning* histories (Figures 4.7 and 4.8). Lower thickness anomalies are more likely to lead to a good fit to the annual layer thickness data (Figure 4.5 third row). This finding is highlighted by the fact that the largest thickness anomaly tested (500 m) accounts for about 1.7% of the *Thinning Only* ensemble and 6.6% of the *Thickening-Thinning* ensemble. For the other evaluation bounds, the 500 m thickness anomaly only shows up in the ensemble resulting from the F16 bounds and *Thinning Only* history. Even a thickness anomaly of 350 m accounts

for only about 10% of both thinning history ensembles. This result is also supported by the *No Thinning* history having a much larger ensemble of model results that fit the evaluation bounds than the other two thinning histories, suggesting that little-to-no thickness change from the LGM to present is most consistent with the accumulation rate reconstructions and the ice-flow model.

The parameter combinations that lead to the lowest RMSEs between the model and data only include the lowest thickness anomalies (60 and 125 m; Figure 4.5 third row). Not every parameter combination with the lowest anomalies, however, leads to the lowest RMSE category. The low thickness anomalies dominate the ensemble in every way, including in every bin of the RMSE histogram.

The other parameter that also exerts a strong control over the composition of the results ensemble is the basal melt rate (Figures 4.6 through 4.8). Though the two highest melt rates (0.01 and 0.005 m/yr) are favored (except when the F16_B21 bounds are used with the *No Thinning* history), each melt rate value shows up in the ensembles except when the strictest B21_ens bounds are used. As with the thickness anomaly, the favored melt rates do not always lead to better fits (i.e., lower RMSEs), but the least favored melt rates never lead to the best fits (Figure 4.5 fourth row).

The vertical velocity shape parameter, p, also exerts some control over the ensemble with higher values (indicating strong flank flow conditions) showing up most often. Despite the fact that the lowest value of p included in this analysis is still more indicative of a flank flow than a divide flow regime, it shows up less than 7% of the time in each of the ensembles (and less than 1% of the time for all bounds except B21_mean) and leads to only high RMSEs (Figure 4.5 fifth row).

Finally, small adjustments to the timing of the thinning history have very little influence on which parameter combinations lead to model results that fit within the evaluation bounds. The *Thickening-Thinning* history ensemble includes twice as many more combinations with the thinning shifted 1,000 years later (+1,000) than with the thinning shifted 1,000 years later (-1,000). The *Thinning Only* history shows only a slight preference for the thinning to

be shifted 1,000 years later.

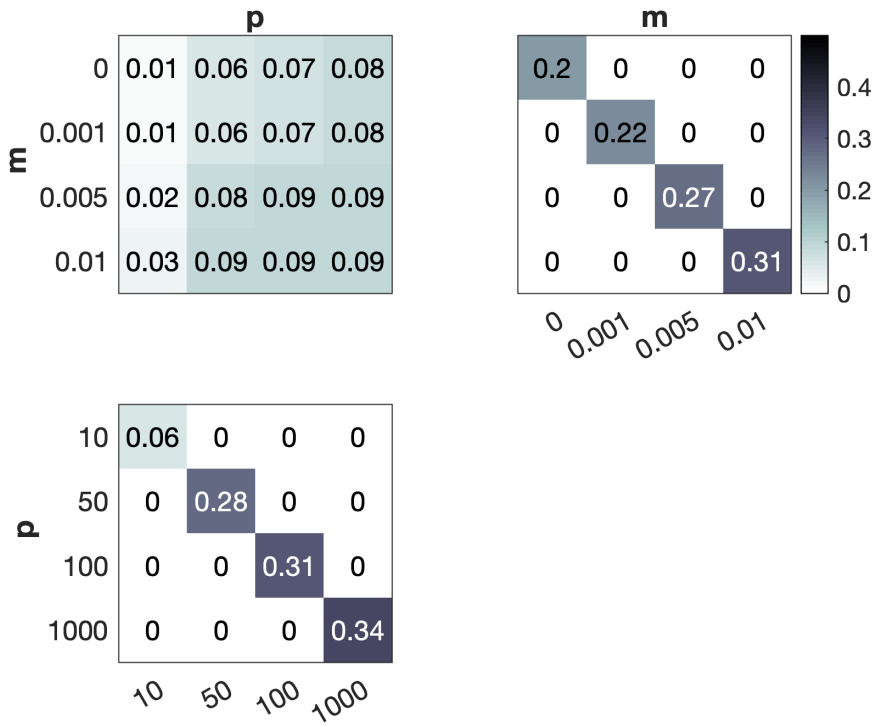

Figure 4.6: Frequency of parameter combinations for the *No Thinning* history ensemble. Each value and the associated shading shows the fractional frequency of the occurance of the x- and y-values. Each bounded box sums to one. m is the basal melt rate in m/yr. p is the parameter determining the shape of the vertical velocity profile, where larger values are more indicative of the flank-flow regime at the ice core site (Figure 4.4).

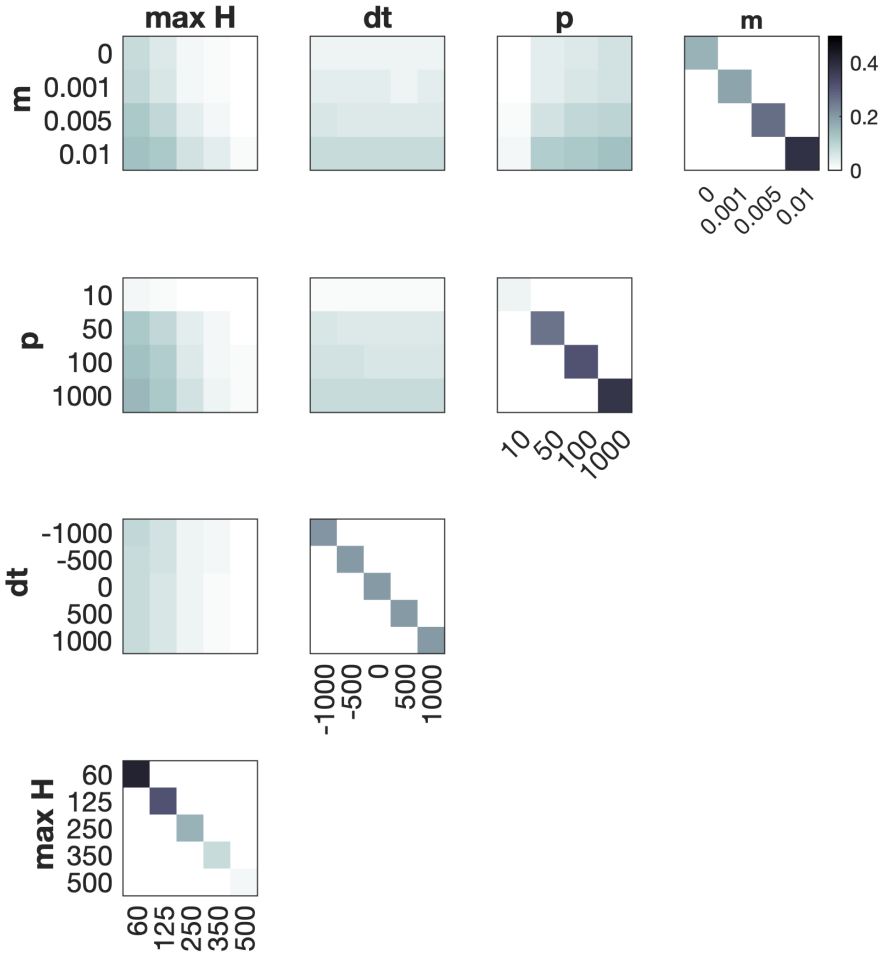

Figure 4.7: Frequency of parameter combinations for the *Thinning Only* history ensemble. Each shaded box shows the fractional frequency of the occurance of the x- and y-values. Each bounded box sums to one. $maxH$ is the maximum thickness anomaly in meters that is reached in the thinning history. m is the basal melt rate in m/yr. p is the parameter determining the shape of the vertical velocity profile, where larger values are more indicative of a flank-flow regime (Figure 4.4). dt is the shift in the thinning history timing in years, where positive values refer to a forward shift in time and negative values are a backwards shift.

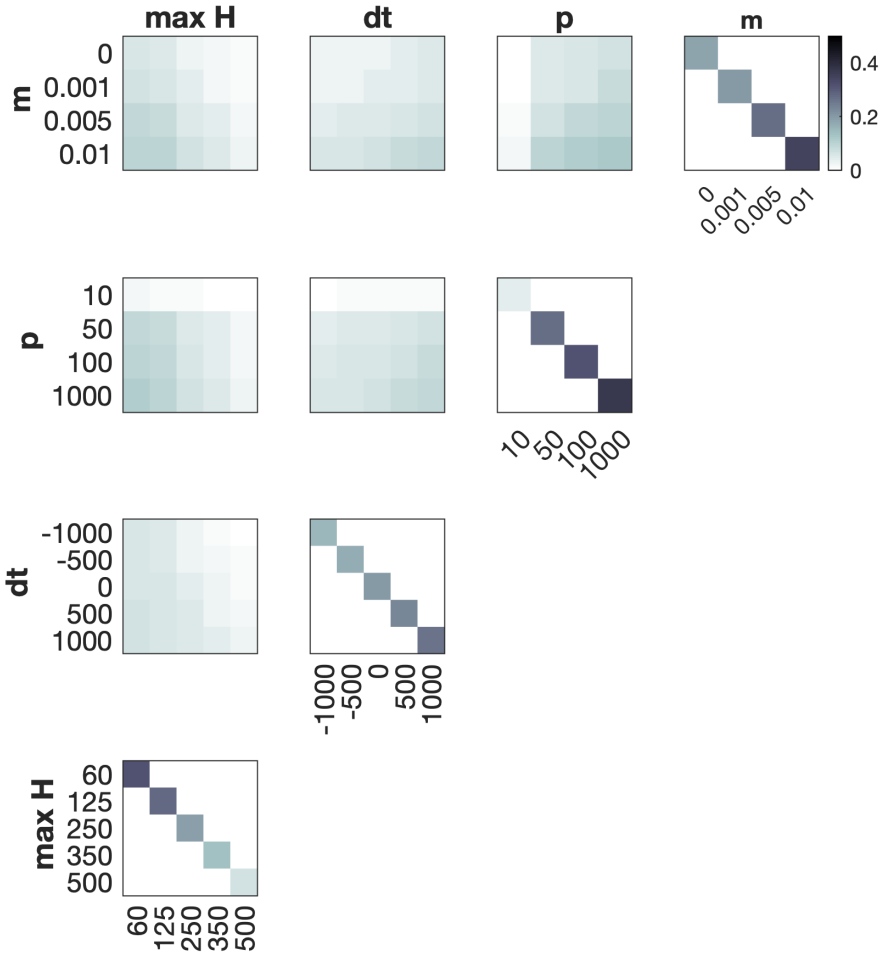

Figure 4.8: Like Figure 4.7, but for the *Thickening-Thinning* history.

4.5 Discussion

Our results indicate that the ice at the WAIS Divide ice core site was most likely less than 125 m thicker during the past 20,000 years. This conclusion is based on the consistency between the annual layer thickness data, the Fudge et al. (2016) and Buizert et al. (2021) accumulation rate reconstructions, and the one-dimensional ice-flow model. This thickness finding translates to an ice sheet elevation that was less than 90 to 125 m higher. Our results

do not differentiate between a highstand occurring during the LGM or in the early Holocene, but they do indicate that, if a large highstand occured, then it is more likely to have occured in the early Holocene than during the LGM.

If the WAIS Divide ice core site were 0 to 125 m higher at the LGM, and assuming a modern spatial lapse rate of 12°C/km (Masson-Delmotte et al., 2008), the elevation change could explain about 0 to 1.5°C of the 6 ± 2°C temperature change contrast between ice core sites in East and West Antarctica during the last deglaciation (Buizert et al., 2021). Assuming ice core sites in East Antarctica were about 100 m lower, another 1°C can be explained. This leaves a differential temperature change of 3.5 to 5°C that is not explained by the elevation changes that are most consistent with published accumulation rate reconstructions, annual layer thickness data, and our ice-flow model for the WAIS Divide ice core site. In the following, we discuss three potential explanations for these findings: the spatial heterogeneity in non-adiabatic temperature changes during the deglaciation, assumptions in the accumulation rate reconstructions being evaluatied, and assumptions in the ice-flow model. It is possible that all three of these explanations are needed to reconcile our results with Antarctic deglacial temperature changes. We also discuss future work that could be done to explore each direction.

4.5.1 Spatial Heterogeneity in Non-Adiabatic Temperature Change

If differential elevation change does not fully explain the East-West difference in deglacial temperature change, this could indicate that there is more spatial heterogeneity in the non-adiabatic temperature change than currently acknowledged in the literature and simulated by climate models. Without major elevation changes, the primary climate forcings during the last deglaciation were orbital changes and greenhouse gases (Hays et al., 1976). The influence of orbital forcings vary by latitude, while greenhouse gases are well-mixed on annual timescales, meaning that neither are expected to produce the East-West temperature difference seen in ice cores without additional influence from feedbacks. Though feedbacks may cause spatial heterogeneity in temperature change, a strong East-West asymmetry is

not seen in most climate simulations of the last deglaciation without invoking differential elevation changes (Werner et al., 2018; Buizert et al., 2021).

Future work could look for processes that are mis-represented or unaccounted for in the climate models and that would affect the modeled temperature change during the last deglaciation. As an example, Antarctic clouds are known to affect temperature in climate model simulations through their influence on the radiation balance (Lachlan-Cope, 2010). Antarctic clouds are also known to be difficult for models to capture accurately (Bromwich et al., 2012). Dütsch et al. (2019b) found that replacing a common cloud parameterization of supersaturation with respect to ice with a physics-based model led a climate model to capture the LGM-to-present change in deuterium excess in Antarctic ice cores, a proxy for the source temperature of water isotopes. Improving cloud parameterizations in climate models may not ultimately lead to a different estimate of Antarctic deglacial temperature change, but it is one example of a direction that could be explored, especially given multiple lines of evidence that the Antarctic ice sheet may not have been higher enough in the LGM to sufficiently explain the East-West temperature difference.

4.5.2 Accumulation Rate Reconstruction Assumptions

Inconsistencies between our results and the differential Antarctic temperature change could also be due to the accumulation rates, which were created with an assumption of little-to-no thinning (Buizert et al., 2015). If the ice core site was 350 to 500 m higher in the LGM, then these larger thickness changes need to be included in the creation of the accumulation rate reconstructions.

Future work investigating the accumulation rate reconstructions would ideally use methods that are independent from assumptions about ice sheet thickness or elevation. Then the independent accumulation rates and the annual layer thickness data could be used to solve for the ice-column thinning history using an inverse approach. Kahle et al. (2021) use two methods to reconstruct accumulation rates for the South Pole ice core, both of which are promising for the creation of independent reconstructions for the WAIS Divide ice core.

One method is a statistical inverse approach that relies on water isotope diffusion length, Δage, and annual layer thickness datasets. To calculate the diffusion length, an estimate of the atmospheric pressure is needed, which depends on elevation of the site. The other method reconstructs accumulation rates from a thinning function derived from δ^{15}N of N_2 (Parrenin et al., 2004). This method requires an estimate of the temperature difference between the top and bottom of the diffusive firn column. In Kahle et al. (2021), they use a one-dimensional thermomechanical ice-flow model that is forced by an accumulation rate reconstruction and presumably also assumes a history of ice-column thinning. Both of these methods thus appear to be very weakly dependent on assumptions about ice thickness and elevation, but further work would need to be done to learn about the sensitivity of the resulting accumulation rate reconstruction to these assumptions.

4.5.3 Glaciological Assumptions

Uncertainty in the assumptions in our ice-flow model is a third possible reason for why our study finds elevation changes that are too small to explain the heterogeneous nature of the deglacial temperature change. The one-dimensional model captures the key processes involved in the thinning of layers, but it does not capture all processes. There may be an assumption that, if improved, would allow for greater amounts of ice-column thinning to be consistent with the accumulation rate reconstructions and annual layer thickness data.

Future work could use higher-dimensional ice-flow models to explore the impact of assumptions made by the one-dimensional model. Because higher-dimensional models are more complex and more computationally expensive, it would be difficult to explore the full uncertainty space. To start, future work could target assumptions that are known to be inaccurate in the one-dimensional model, but whose impact on our results has not been quantified. For example, as ice flows from the divide to the ice core site the accumulation rate, vertical velocity profile, and bed topography change (Neumann et al., 2008; Conway and Rasmussen, 2009). Each of these known factors may be included in a model, as was done in Koutnik et al. (2016), to learn about their impact on the annual layer thicknesses at the ice core site.

Such work, however, would not be without its own assumptions. For example, there are minimal constraints on the spatial pattern of the basal melt rate (Neumann et al., 2008), the path of the flowline is difficult to capture since it asymptotes at the divide (Conway and Rasmussen, 2009), and the spatial pattern of flow convergence is uncertain (Koutnik et al., 2016).

For models of ice flow near the WAIS Divide ice core site, the transient nature of each variable is also largely unknown, particularly for the deglacial period. For the Holocene, many variables can reasonably be assumed to remain constant, such as the spatial pattern in the accumulation rate (Neumann et al., 2008). For the deglacial period, this assumption is much more difficult to justify given the doubling of accumulation rates (Fudge et al., 2016) and potential changes in the divide position. The divide is known to be moving today (Neumann et al., 2008; Conway and Rasmussen, 2009) and may have been influenced by the large changes at the ice sheet margin during the deglaciation. Other unknowns include the basal melt rate and flow convergence magnitudes and spatial patterns and how they changed through time. Some of these unknowns could be specifically targeted with the incorporation of internal layers into modeling studies (e.g., Koutnik et al., 2016; Sutter et al., 2021; Frémand et al., 2022). For example, layers are known to reflect the history of spatial and temporal changes in accumulation rates and divide position and can be used to evaluate whether specific histories are glaciologically consistent with the internal ice sheet structure (e.g., Neumann et al., 2008; Conway and Rasmussen, 2009; Koutnik et al., 2016). Unfortunately, reliably traced and dated layers in the vicinity of the WAIS Divide ice core are scarce, especially for the period 15 to 10 ka BP (Koutnik et al., 2016), when significant ice-column thickness changes are most likely to have occured.

4.6 Conclusion

Differential elevation change has been used to explain why the deglacial temperature change is greater at West Antarctic than at East Antarctic ice core sites (Werner et al., 2018; Buizert et al., 2021). A large elevation decrease, and an associated ice-column thinning, at the WAIS

Divide ice core site are essential to this hypothesis; however, these elevation and thickness changes remain uncertain (see Section 4.2.2). We find that the ice-column thinning histories that are most consistent with published accumulation rate reconstructions and annual layer thickness data cannot explain the difference in East-West Antarctic temperature change during the last deglaciation. We identify three factors that could explain this inconsistency: the spatial heterogeneity in non-adiabatic temperature changes during the deglaciation, assumptions in the accumulation rate reconstructions, and assumptions in the ice-flow model. Future investigations into these factors would lead to a more consistent understanding of Antarctic climate and interior ice sheet changes during the last deglaciation.

Chapter 5
CONCLUSION

In the following, I lay out my contributions to understanding polar climate and ice sheets. Specifically, I address the four questions introduced in Chapter 1 that are directly related to the body of work contained within this dissertation:

1. How does the relationship between temperature and precipitation vary in space and time across Greenland during the last glacial-interglacial transition?

2. Is climate variability stronger in northern or southern Greenland on glacial-interglacial timescales?

3. What caused the difference in East and West Antarctic temperature change over the last deglaciation?

4. What elevation was the West Antarctic ice sheet at the Last Glacial Maximum?

Though each question specifically targets one ice sheet, I show how some conclusions are more broadly applicable. I also provide recommendations for future work.

5.1 Insights into Greenland Climate During the Last Deglaciation

How does the relationship between temperature and precipitation vary in space and time across Greenland during the last glacial-interglacial transition?

In Chapter 2, I investigate the relationship between temperature and precipitation across Greenland, an analysis which is made possible by the independent reconstructions of temperature and precipitation that are spatially and temporally complete. I find that, on glacial-interglacial timescales, the relationship can be described by an exponential scaling that is

common in the literature (e.g., Greve et al., 2011). The scaling factor that determines how sensitive precipitation is to temperature, however, is spatially variable, such that the single value commonly used in the literature is not applicable for all locations around the ice sheet. I also find that, for shorter timescales, the scaling is not applicable and that the relationship between precipitation and temperature is weak. Given similar findings from the WAIS Divide ice core in Antarctica (Fudge et al., 2016), I would expect these conclusions to be generally applicable to other locations and time periods.

Is climate variability stronger in northern or southern Greenland on glacial-interglacial timescales?

The temperature reconstruction from Chapter 2 also allows me to investigate the question of spatial climate variability. For all time periods, I find stronger variability in the North. Given the data assimilation method used to reconstruct temperature, this result could be due to the influence of the proxy records, the climate model, or a combination of the two. The temperature proxy records I use are water isotopes of ice, which are known to be more variable in ice cores located farther north and less variable in cores that are farther south. The ensemble of climate simulations I use is also more variable in the north, especially the northwest, due to the disappearance of the Laurentide ice sheet. In Chapter 2, I investigate how my results might change if I include different proxy records or use a different ensemble of climate simulations. I find that the inclusion of temperature reconstructions derived from measurements of nitrogen isotopes of nitrogen gas, which are more variable towards the south, do not change my results. When I use an ensemble of climate simulations with more variability in the south, however, this results in a reconstruction with more variability in southern Greenland. This investigation shows that the reconstruction of temperature variability is more strongly influenced by the choice of climate ensemble than the choice of available proxy records. Though Chapter 2 contributes to the question of climate variability, there remains more work to be done to hone in on an answer.

5.1.1 Recommendations for Future Work

My recommendations for future work from Chapter 2 fall into two categories: 1) improvement of the paleoclimate data assimilation method for long timescales and specifically for the Greenland climate reconstructions and 2) new directions for reconstructing paleo ice sheets and climate. One improvement to the paleoclimate data assimilation method would be to assimilate more proxy records in order to put more data constraints on the reconstruction and to rely less on the prior model ensemble. Such work might aid in further addressing the question of whether climate variability is stronger in northern or southern Greenland. In Appendix A, I identify the need for higher-quality records of temperature and precipitation in southern Greenland. Such records may be obtained by drilling a new ice core at South Dome, Greenland (Osterberg et al., 2020). In addition to new records, other types of proxy records from ice cores could be included, such as nitrogen isotopes of nitrogen gas (a temperature proxy), borehole temperature profiles, and records of total air content. For any additional proxy records that are included there will also need to be development of proxy system models for each. An extension of this idea would be to include proxies from other types of paleoclimate archives, such as lake and ocean sediment records. Including these proxies would not only require new proxy system models but it would also require an update to the data assimilation method because each paleoclimate archive has a different time resolution. The theory of assimilating proxies of different time resolutions was developed by (Steiger and Hakim, 2015), but, to my knowledge, it has yet to be applied beyond idealized test cases. With the addition of proxy records, there is also the potential to reconstruct seasonal changes because many proxies are seasonal in nature (Tardif et al., 2019).

Another direction for improving paleoclimate data assimilation reconstructions is to update the prior ensemble of climate simulations. New climate simulations would benefit from having higher spatial resolutions and more up-to-date ice sheet reconstructions than the TraCE-21ka simulation (Liu et al., 2009, 2012; He et al., 2013; Osman et al., 2021). Having just one or two simulations of the past, however, does not allow for a complete assessment

of model biases (Amrhein et al., 2020; Parsons et al., 2021), so ideally there would be a large set of new simulations created using a variety of climate models. Whether or not new simulations are available, one could also work with existing simulations and update the way the ensembles are created from the climate simulations. In Chapter 2, I randomly selected ensemble members from the full 20,000 years of the climate simulation. For this long of a time period, however, the spatial covariance structure of climate is not expected to remain constant. An update of my climate reconstructions from Chapter 2 should include prior ensembles that are drawn from a smaller time window around each timestep. This would result in a transient prior ensemble that can work for offline data assimilation (also known as transient offline paleoclimate data assimilation). To my knowledge, this has been implemented for the first time in Osman et al. (2021).

Considering either the reconstructions from Chapter 2 or updated reconstructions, the use of paleoclimate data assimilation provides independent reconstructions of temperature and precipitation that can be used to force ice sheet models in lieu of a precipitation reconstruction scaled from temperature. This was done for the first time in Briner et al. (2020); however, that study did not compare the results from the independent forcings against results from using a scaled forcing. Such an investigation would help determine whether it is important to use independent reconstructions of temperature and precipitation for accurate simulations of paleo ice sheet evolution.

Another direction for future work is to expand the use of long timescale paleoclimate data assimilation. Chapter 2 applies this method to Greenland and Osman et al. (2021) apply it at a global scale. Neither study uses the full suite of available proxy records. Future studies could target global and regional questions of past climate change with updated or new reconstructions from long timescale paleoclimate data assimilation.

5.2 Insights into Antarctic Temperature and Elevation at the Last Glacial Maximum

What caused the difference in East and West Antarctic temperature change over the last deglaciation? What elevation was the West Antarctic ice sheet at the Last Glacial Maximum?

These two questions are closely tied to each other through the prevailing hypothesis that elevation change was the cause of heterogeneous temperature change in Antarctica during the last deglaciation. Chapters 3 and 4 address these questions from different angles. In Chapter 3, I interrogate a temperature-based paleoaltimetry method that is used as the justification for this theory (e.g., Steig et al., 2001; Buizert et al., 2021). Using an ensemble of climate simulations, I find that the method is prone to large uncertainties and that other methods are needed to reconstruct the past elevation of the ice sheet. Though I only examine this paleoaltimetry method for Antarctica, it is likely that this method also has large uncertainties in Greenland, which may need to be incorporated into current (Vinther et al., 2009) and future uses.

The findings from Chapter 3 led me to Chapter 4, in which I examine whether published estimates of elevation change are consistent with low-uncertainty and widely-accepted datasets that are co-located with the WAIS Divide ice core climate records. I find that, to be consistent with published annual layer thickness data and accumulation rate reconstructions, the site was likely less than 125 m thicker during the past 20,000 years. This finding implies that adiabatic-induced warming over the site may have only contributed 0 to 1.5°C to the approximately 6°C difference in temperature change between East and West Antarctic ice core sites (Buizert et al., 2021). Though this chapter does not reconstruct elevation, it shows that the scientific community has yet to converge on a history of the Antarctic ice sheet and climate that is consistent with all available datasets. In both the chapter and the following section, I provide specific paths forward for investigating which pieces of our understanding may need to be reassessed.

5.2.1 Recommendations for Future Work

A remaining question from Chapter 3 is whether the qualitative and quantitative findings of the analysis are applicable to other LGM Antarctic ice sheet configurations, the Greenland ice sheet, and other time periods, such as the Holocene or last interglacial period. This question could be addressed by performing the same analysis for climate simulations run for each of these scenarios. In future versions of this analysis, investigators could also consider filtering or weighting the model simulations by how well they are able to simulate near-surface processes, which may make the estimates of method uncertainty more accurate.

Though the temperature-based paleoaltimetry method is traditionally used between two proxy locations, it would be interesting to investigate whether a larger network of proxies would reduce the method uncertainty. Having a network of proxy records also opens up other possibilities for reconstructing past elevation. For example, one could consider using formal data assimilation methods, such as the Kalman filter or variational methods. The use of data assimilation methods can help to extract more information from proxy records and can also allow for the incorporation of a broader network of types of proxies in a physically consistent way (Perkins and Hakim, 2021).

The conclusions in Chapter 4 provide a natural set of next steps to investigate why published datasets and reconstructions do not lead to a glaciologically consistent history of the Antarctic ice sheet and climate. There are three ways that we could revise our understanding to bring them into alignment. One direction to investigate is whether climate models are missing or mis-representing a process that would lead to more spatial variability in non-adiabatic temperature change during the last deglaciation. Mis-representations in climate models that strongly affect simulations of the polar regions have been found previously (e.g., Dütsch et al., 2019a). Another direction to investigate is the assumptions that go into the accumulation rate reconstructions. The results of Chapter 4 are perhaps unsurprising upon noting that the published accumulation rates are reconstructed with an assumption of little-to-no elevation change at the WAIS Divide ice core site (Buizert et al., 2015). If larger

thickness changes occurred, then either this needs to be accounted for in reconstructing accumulation rates or a method of reconstruction that is independent of the elevation and thinning histories must be used (e.g., Kahle et al., 2021). A third direction to investigate is the ice-flow model used to determine whether pairs of thinning histories and accumulation rate reconstructions are consistent with the annual layer thickness data. The model we use incorporates the most dominant processes, but it ignores two- and three-dimensional effects, which can influence locations away from divides, such as the WAIS Divide ice core site. The use of higher-dimensional models would allow for the incorporation of more datasets that may further constrain the problem, such as dated internal layers (Koutnik et al., 2016). More complex models, however, would make uncertainty analyses more difficult due to the increased computational expense.

BIBLIOGRAPHY

Ackert, R. P., Barclay, D. J., Borns, H. W., Calkin, P. E., Kurz, M. D., Fastook, J. L., and Steig, E. J. (1999). Measurements of past ice sheet elevations in interior West Antarctica. *Science*, 286(5438):276–280.

Ackert, R. P., Mukhopadhyay, S., Parizek, B. R., and Borns, H. W. (2007). Ice elevation near the West Antarctic Ice Sheet divide during the last glaciation. *Geophysical Research Letters*, 34(21).

Ackert, R. P., Mukhopadhyay, S., Pollard, D., DeConto, R. M., Putnam, A. E., and Borns, H. W. (2011). West Antarctic Ice Sheet elevations in the Ohio Range: geologic constraints and ice sheet modeling prior to the last highstand. *Earth and Planetary Science Letters*, 307(1-2):83–93.

Ackert, R. P., Putnam, A. E., Mukhopadhyay, S., Pollard, D., DeConto, R. M., Kurz, M. D., and Borns, H. W. (2013). Controls on interior West Antarctic Ice Sheet Elevations: inferences from geologic constraints and ice sheet modeling. *Quaternary Science Reviews*, 65:26–38.

Albrecht, T., Winkelmann, R., and Levermann, A. (2020). Glacial-cycle simulations of the Antarctic Ice Sheet with the Parallel Ice Sheet Model (PISM)–Part 2: Parameter ensemble analysis. *The Cryosphere*, 14(2):633–656.

Alley, R. B., Andrews, J. T., Brigham-Grette, J., Clarke, G., Cuffey, K. M., Fitzpatrick, J., Funder, S., Marshall, S., Miller, G., Mitrovica, J., Muhs, D., Otto-Bliesner, B., Polyak, L., and White, J. (2010). History of the Greenland Ice Sheet: Paleoclimatic insights. *Quaternary Science Reviews*, 29(15-16):1728–1756.

Alley, R. B., Meese, D., Shuman, C., Gow, A., Taylor, K. C., Grootes, P., White, J., Ram, M., Waddington, E., Mayewski, P., and Zielinski, G. (1993). Abrupt increase in Greenland snow accumulation at the end of the Younger Dryas event. *Nature*, 362(6420):527.

Alley, R. B., Shuman, C., Meese, D., Gow, A., Taylor, K., Cuffey, K., Fitzpatrick, J., Grootes, P., Zielinski, G., Ram, M., Spinelli, G., and Elder, B. (1997). Visual-stratigraphic dating of the GISP2 ice core: Basis, reproducibility, and application. *Journal of Geophysical Research: Oceans*, 102(C12):26367–26381.

Amrhein, D. E., Hakim, G. J., and Parsons, L. A. (2020). Quantifying structural uncertainty in paleoclimate data assimilation with an application to the last millennium. *Geophysical Research Letters*, 47(22):e2020GL090485.

Andersen, K. K., Azuma, N., Barnola, J.-M., Bigler, M., Biscaye, P., Caillon, N., Chappellaz, J., Clausen, H. B., Dahl-Jensen, D., Fischer, H., Flckiger, J., Fritzsche, D., Fujii, Y., Goto-Azuma, K., Grønvold, K., Gundestrup, N. S., Hansson, M., Huber, C., Hvidberg, C. S., Johnsen, S. J., Jonsell, U., Jouzel, J., Kipfstuhl, S., Landais, A., Leuenberger, M., Lorrain, R., Masson-Delmotte, V., Miller, H., Motoyama, H., Narita, H., Popp, T., Rasmussen, S. O., Raynaud, D., Röthlisberger, R., Ruth, U., Samyn, D., Schwander, J., Shoji, H., Siggard-Andersen, M. L., Steffensen, J. P., Stocker, T., Sveinbjörnsdottir, A. E., Svensson, A., Takata, M., Tison, J. L., Thorsteinsson, T., Watanabe, O., Wilhelms, F., and White, J. (2004). High-resolution record of Northern Hemisphere climate extending into the last interglacial period. *Nature*, 431(7005):147–151.

Andersen, K. K., Svensson, A., Johnsen, S. J., Rasmussen, S. O., Bigler, M., Röthlisberger, R., Ruth, U., Siggaard-Andersen, M.-L., Steffensen, J. P., Dahl-Jensen, D., Vinther, B. M., and Clausen, H. B. (2006). The Greenland ice core chronology 2005, 15–42 ka. Part 1: Constructing the time scale. *Quaternary Science Reviews*, 25(23-24):3246–3257.

Anderson, J. L. and Anderson, S. L. (1999). A Monte Carlo implementation of the nonlin-

ear filtering problem to produce ensemble assimilations and forecasts. *Monthly Weather Review*, 127(12):2741–2758.

Armengaud, A., Koster, R. D., Jouzel, J., and Ciais, P. (1998). Deuterium excess in Greenland snow: Analysis with simple and complex models. *Journal of Geophysical Research: Atmospheres*, 103(D8):8947–8953.

Axelrod, D. I. (1965). A method for determining the altitudes of Tertiary floras. *Paleobotanist*, 14:144–171.

Badgeley, J. A., Steig, E. J., Hakim, G. J., and Fudge, T. J. (2020). Greenland temperature and precipitation over the last 20 000 years using data assimilation. *Climate of the Past*, 16(4):1325–1346.

Bender, M., Sowers, T., Dickson, M.-L., Orchardo, J., Grootes, P., Mayewski, P. A., and Meese, D. A. (1994). Climate correlations between Greenland and Antarctica during the past 100 000 years. *Nature*, 372(6507):663.

Bindschadler, R. A., Nowicki, S., Abe-Ouchi, A., Aschwanden, A., Choi, H., Fastook, J., Granzow, G., Greve, R., Gutowski, G., Herzfeld, U., Jackson, C., Johnson, J., Khroulev, C., Levermann, A., Lipscomb, W., Martin, M., Morlighem, M., Parizek, B., Pollard, D., Price, S., Ren, D., Saito, F., Sato, T., Seddik, H., Seroussi, H., Takahashi, K., Walker, R., and Wang, W. (2013). Ice-sheet model sensitivities to environmental forcing and their use in projecting future sea level (the SeaRISE project). *Journal of Glaciology*, 59(214):195–224.

Bintanja, R., van de Wal, R. S., and Oerlemans, J. (2005). Modelled atmospheric temperatures and global sea levels over the past million years. *Nature*, 437(7055):125–128.

Box, J. E. (2013). Greenland ice sheet mass balance reconstruction. Part II: Surface mass balance (1840–2010). *Journal of Climate*, 26(18):6974–6989.

Braconnot, P., Harrison, S. P., Kageyama, M., Bartlein, P. J., Masson-Delmotte, V., Abe-Ouchi, A., Otto-Bliesner, B., and Zhao, Y. (2012). Evaluation of climate models using palaeoclimatic data. *Nature Climate Change*, 2(6):417.

Braconnot, P., Harrison, S. P., Otto-Bliesner, B., Abe-Ouchi, A., Jungclaus, J., and Peterschmitt, J.-Y. (2011). The paleoclimate modeling intercomparison project contribution to CMIP5. *CliVAR Exchanges*, 56(16):15–19.

Brady, E., Stevenson, S., Bailey, D., Liu, Z., Noone, D., Nusbaumer, J., Otto-Bliesner, B., Tabor, C., Tomas, R., Wong, T., Zhang, J., and Zhu, J. (2019). The connected isotopic water cycle in the Community Earth System Model version 1. *Journal of Advances in Modeling Earth Systems*, 11(8):2547–2566.

Briggs, R. D., Pollard, D., and Tarasov, L. (2014). A data-constrained large ensemble analysis of Antarctic evolution since the Eemian. *Quaternary Science Reviews*, 103:91–115.

Briggs, R. D. and Tarasov, L. (2013). How to evaluate model-derived deglaciation chronologies: a case study using Antarctica. *Quaternary Science Reviews*, 63:109–127.

Briner, J. P., Cuzzone, J. K., Badgeley, J. A., Young, N. E., Steig, E. J., Morlighem, M., Schlegel, N.-J., Hakim, G. J., Schaefer, J. M., Johnson, J. V., Lesnek, A., Thomas, E., Allan, E., Bennike, O., Cluett, A., Csatho, B., de Vernal, A., Downs, J., Larour, E., and Nowicki, S. (2020). Rate of mass loss from the Greenland Ice Sheet will exceed Holocene values this century. *Nature*, 586(7827):70–74.

Bromwich, D. H., Nicolas, J. P., Hines, K. M., Kay, J. E., Key, E. L., Lazzara, M. A., Lubin, D., McFarquhar, G. M., Gorodetskaya, I. V., Grosvenor, D. P., Lachlan-Cope, T., and van Lipzig, P. (2012). Tropospheric clouds in Antarctica. *Reviews of Geophysics*, 50(1).

Buchardt, S. L., Clausen, H. B., Vinther, B. M., and Dahl-Jensen, D. (2012). Investigating the past and recent δ^{18}O-accumulation relationship seen in Greenland ice cores. *Climate of the Past*, 8(6):2053.

Buizert, C., Cuffey, K., Severinghaus, J., Baggenstos, D., Fudge, T., Steig, E., Markle, B., Winstrup, M., Rhodes, R. H., Brook, E. J., Sowers, T., Clow, G., Cheng, H., Edwards, R., Sigl, M., McConnell, J., and Taylor, K. (2015). The WAIS Divide deep ice core WD2014 chronology–Part 1: Methane synchronization (68–31 ka BP) and the gas age–ice age difference. *Climate of the Past*, 11(2):153–173.

Buizert, C., Fudge, T., Roberts, W. H., Steig, E. J., Sherriff-Tadano, S., Ritz, C., Lefebvre, E., Edwards, J., Kawamura, K., Oyabu, I., Motoyama, H., Kahle, E., Jones, T., Abe-Ouchi, A., Obase, T., Martin, C., Corr, H., Severinghaus, J., Beaudette, R., Epifanio, J., Brook, E., Martin, K., Chappellaz, J., Aoki, S., Nakazawa, T., Sowers, T., Alley, R., Ahn, J., Sigl, M., Severi, M., Dunbar, N., Svensson, A., Fegyveresi, J., He, C., Liu, Z., Zhu, J., Otto-Bliesner, B., Lipenkov, V., Kageyama, M., and Schwander, J. (2021). Antarctic surface temperature and elevation during the Last Glacial Maximum. *Science*, 372(6546):1097–1101.

Buizert, C., Gkinis, V., Severinghaus, J. P., He, F., Lecavalier, B. S., Kindler, P., Leuenberger, M., Carlson, A. E., Vinther, B., Masson-Delmotte, V., White, J., Liu, Z., Otto-Bliesner, B., and Brook, E. (2014). Greenland temperature response to climate forcing during the last deglaciation. *Science*, 345(6201):1177–1180.

Buizert, C., Keisling, B., Box, J., He, F., Carlson, A., Sinclair, G., and DeConto, R. (2018). Greenland-wide seasonal temperatures during the last deglaciation. *Geophysical Research Letters*, 45(4):1905–1914.

Cauquoin, A., Werner, M., and Lohmann, G. (2019). Water isotopes-climate relationships for the mid-holocene and preindustrial period simulated with an isotope-enabled version of MPI-ESM. *Climate of the Past*, 15(6):1913–1937.

Chang, W., Haran, M., Applegate, P., and Pollard, D. (2016). Calibrating an ice sheet model using high-dimensional binary spatial data. *Journal of the American Statistical Association*, 111(513):57–72.

Clark, P. U., Dyke, A. S., Shakun, J. D., Carlson, A. E., Clark, J., Wohlfarth, B., Mitrovica, J. X., Hostetler, S. W., and McCabe, A. M. (2009). The last glacial maximum. *science*, 325(5941):710–714.

Clark, P. U. and Mix, A. C. (2002). Ice sheets and sea level of the Last Glacial Maximum. *Quaternary Science Reviews*, 21(1-3):1–7.

Clow, G., Cuffey, K., and Waddington, E. (2012). High heat-flow beneath the central portion of the West Antarctic Ice Sheet. In *AGU Fall Meeting Abstracts*, volume 2012, pages C31A–0577.

Conway, H., Hall, B., Denton, G., Gades, A., and Waddington, E. (1999). Past and future grounding-line retreat of the West Antarctic Ice Sheet. *Science*, 286(5438):280–283.

Conway, H. and Rasmussen, L. (2009). Recent thinning and migration of the Western Divide, central West Antarctica. *Geophysical Research Letters*, 36(12).

Cook, E. R., Meko, D. M., Stahle, D. W., and Cleaveland, M. K. (1999). Drought reconstructions for the continental United States. *Journal of Climate*, 12(4):1145–1162.

Cuffey, K. M. and Clow, G. D. (1997). Temperature, accumulation, and ice sheet elevation in central Greenland through the last deglacial transition. *Journal of Geophysical Research: Oceans*, 102(C12):26383–26396.

Cuffey, K. M., Clow, G. D., Alley, R. B., Stuiver, M., Waddington, E. D., and Saltus, R. W. (1995). Large arctic temperature change at the Wisconsin-Holocene glacial transition. *Science*, 270(5235):455–458.

Cuffey, K. M., Clow, G. D., Steig, E. J., Buizert, C., Fudge, T., Koutnik, M., Waddington, E. D., Alley, R. B., and Severinghaus, J. P. (2016). Deglacial temperature history of West Antarctica. *Proceedings of the National Academy of Sciences*, 113(50):14249–14254.

Cuffey, K. M. and Steig, E. J. (1998). Isotopic diffusion in polar firn: Implications for interpretation of seasonal climate parameters in ice-core records, with emphasis on central greenland. *Journal of Glaciology*, 44(147):273–284.

Cuzzone, J. K., Schlegel, N.-J., Morlighem, M., Larour, E., Briner, J. P., Seroussi, H., and Caron, L. (2019). The impact of model resolution on the simulated Holocene retreat of the southwestern Greenland ice sheet using the Ice Sheet System Model (ISSM). *The Cryosphere*, 13(3):879–893.

Dahl-Jensen, D., Gundestrup, N., Gogineni, S. P., and Miller, H. (2003). Basal melt at NorthGRIP modeled from borehole, ice-core and radio-echo sounder observations. *Annals of Glaciology*, 37:207–212.

Dahl-Jensen, D., Johnsen, S., Hammer, C., Clausen, H., and Jouzel, J. (1993). Past accumulation rates derived from observed annual layers in the GRIP ice core from Summit, Central Greenland. In *Ice in the climate system*, pages 517–532. Springer.

Dahl-Jensen, D., Mosegaard, K., Gundestrup, N., Clow, G. D., Johnsen, S. J., Hansen, A. W., and Balling, N. (1998). Past temperatures directly from the Greenland ice sheet. *Science*, 282(5387):268–271.

Dansgaard, W. (1964). Stable isotopes in precipitation. *Tellus*, 16:436–468.

Dansgaard, W., Clausen, H., Gundestrup, N., Hammer, C., Johnsen, S., Kristinsdottir, P., and Reeh, N. (1982). A new Greenland deep ice core. *Science*, 218(4579):1273–1277.

Dansgaard, W. and Johnsen, S. (1969). A flow model and a time scale for the ice core from Camp Century, Greenland. *Journal of Glaciology*, 8(53):215–223.

Dütsch, M., Blossey, P. N., Steig, E. J., and Nusbaumer, J. M. (2019a). Non-equilibrium fractionation during ice cloud formation in iCAM5: Evaluating the common parameterization of supersaturation as a linear function of temperature. *Journal of Advances in Modeling Earth Systems*, 11(11):3777–3793.

Dütsch, M., Blossey, P. N., Steig, E. J., and Nusbaumer, J. M. (2019b). Nonequilibrium fractionation during ice cloud formation in iCAM5: Evaluating the common parameterization of supersaturation as a linear function of temperature. *Journal of Advances in Modeling Earth Systems*, 11(11):3777–3793.

Edwards, T., Fettweis, X., Gagliardini, O., Gillet-Chaulet, F., Goelzer, H., Gregory, J., Hoffman, M., Huybrechts, P., Payne, A., Perego, M., Price, S., Quiquet, A., and Ritz, C. (2014). Probabilistic parameterisation of the surface mass balance–elevation feedback in regional climate model simulations of the Greenland ice sheet. *The Cryosphere*, 8(1):181–194.

Eicher, O., Baumgartner, M., Schilt, A., Schmitt, J., Schwander, J., Stocker, T. F., and Fischer, H. (2016). Climatic and insolation control on the high-resolution total air content in the NGRIP ice core. *Climate of the Past*, 12(10):1979–1993.

Eyring, V., Bony, S., Meehl, G. A., Senior, C. A., Stevens, B., Stouffer, R. J., and Taylor, K. E. (2016). Overview of the Coupled Model Intercomparison Project Phase 6 (CMIP6) experimental design and organization. *Geoscientific Model Development*, 9(5):1937–1958.

Farnsworth, A., Valdes, P. J., Spicer, R. A., Ding, L., Witkowski, C., Lauretano, V., Su, T., Li, S., Li, S., and Zhou, Z. (2021). Paleoclimate model-derived thermal lapse rates: Towards increasing precision in paleoaltimetry studies. *Earth and Planetary Science Letters*, 564:116903.

Fisher, D. A., Reeh, N., and Clausen, H. (1985). Stratigraphic noise in time series derived from ice cores. *Annals of Glaciology*, 7:76–83.

Forest, C. E., Molnar, P., and Emanuel, K. A. (1995). Palaeoaltimetry from energy conservation principles. *Nature*, 374(6520):347–350.

Forest, C. E., Wolfe, J. A., Molnar, P., and Emanuel, K. A. (1999). Paleoaltimetry incorpo-

rating atmospheric physics and botanical estimates of paleoclimate. *Geological Society of America Bulletin*, 111(4):497–511.

Fox-Kemper, B., Hewitt, H., Xiao, C., Aalgeirsdttir, G., Drijfhout, S., Edwards, T., Golledge, N., Hemer, M., Kopp, R., Krinner, G., Mix, A., Notz, D., Nowicki, S., Nurhati, I., Ruiz, L., Salle, J.-B., Slangen, A., and Yu, Y. (2021). Ocean, cryosphere and sea level change. in climate change 2021: The physical science basis. contribution of working group i to the sixth assessment report of the intergovernmental panel on climate change. Technical report, Cambridge, United Kingdom and New York, NY, USA.

Frémand, A. C., Bodart, J. A., Jordan, T. A., Ferraccioli, F., Robinson, C., Corr, H. F., Peat, H. J., Bingham, R. G., and Vaughan, D. G. (2022). British Antarctic Surveys aerogeophysical data: Releasing 25 years of airborne gravity, magnetic, and radar datasets over Antarctica. *Earth System Science Data Discussions*, pages 1–49.

Fudge, T., Biyani, S. C., Clemens-Sewall, D., and Hawley, R. L. (2019). Constraining geothermal flux at coastal domes of the Ross Ice Sheet, Antarctica. *Geophysical Research Letters*, 46(22):13090–13098.

Fudge, T., Markle, B. R., Cuffey, K. M., Buizert, C., Taylor, K. C., Steig, E. J., Waddington, E. D., Conway, H., and Koutnik, M. (2016). Variable relationship between accumulation and temperature in West Antarctica for the past 31,000 years. *Geophysical Research Letters*, 43(8):3795–3803.

Gierz, P., Werner, M., and Lohmann, G. (2017). Simulating climate and stable water isotopes during the Last Interglacial using a coupled climate-isotope model. *Journal of Advances in Modeling Earth Systems*, 9(5):2027–2045.

Gillet-Chaulet, F., Hindmarsh, R. C., Corr, H. F., King, E. C., and Jenkins, A. (2011). In-situ quantification of ice rheology and direct measurement of the Raymond Effect at Summit, Greenland using a phase-sensitive radar. *Geophysical Research Letters*, 38(24).

Gkinis, V., Simonsen, S. B., Buchardt, S. L., White, J., and Vinther, B. M. (2014). Water isotope diffusion rates from the NorthGRIP ice core for the last 16,000 years–Glaciological and paleoclimatic implications. *Earth and Planetary Science Letters*, 405:132–141.

Goehring, B. M., Balco, G., Todd, C., Moening-Swanson, I., and Nichols, K. (2019). Late-glacial grounding line retreat in the northern Ross Sea, Antarctica. *Geology*, 47(4):291–294.

Greve, R. (1997). Application of a polythermal three-dimensional ice sheet model to the Greenland ice sheet: response to steady-state and transient climate scenarios. *Journal of Climate*, 10(5):901–918.

Greve, R., Saito, F., and Abe-Ouchi, A. (2011). Initial results of the SeaRISE numerical experiments with the models SICOPOLIS and IcIES for the Greenland ice sheet. *Annals of Glaciology*, 52(58):23–30.

Grootes, P. M. and Stuiver, M. (1986). Ross Ice Shelf oxygen isotopes and West Antarctic climate history. *Quaternary Research*, 26(1):49–67.

Grootes, P. M. and Stuiver, M. (1987). Ice sheet elevation changes from isotope profiles. *International Association of Hydrological Sciences Publication*, 170:269–281.

Grootes, P. M. and Stuiver, M. (1997). Oxygen 18/16 variability in Greenland snow and ice with 10^{-3}-to 10^{5}-year time resolution. *Journal of Geophysical Research: Oceans*, 102(C12):26455–26470.

Guillevic, M., Bazin, L., Landais, A., Kindler, P., Orsi, A., Masson-Delmotte, V., Blunier, T., Buchardt, S. L., Capron, E., Leuenberger, M., Martinerie, P., Prié, F., and Vinther, B. M. (2013). Spatial gradients of temperature, accumulation and δ^{18}O-ice in Greenland over a series of Dansgaard-Oeschger events. *Climate of the Past*, 9(3).

Gundestrup, N. and Hansen, B. L. (1984). Bore-hole survey at Dye 3, south Greenland. *Journal of Glaciology*, 30(106):282–288.

Hakim, G. J. (2019). Source code for the Last Millennium Reanalysis (LMR) project, available at: https://github.com/modons/lmr.

Hakim, G. J., Emile-Geay, J., Steig, E. J., Noone, D., Anderson, D. M., Tardif, R., Steiger, N., and Perkins, W. A. (2016). The last millennium climate reanalysis project: Framework and first results. *Journal of Geophysical Research: Atmospheres*, 121(12):6745–6764.

Hall, B. L., Denton, G. H., Heath, S. L., Jackson, M. S., and Koffman, T. N. (2015). Accumulation and marine forcing of ice dynamics in the western Ross Sea during the last deglaciation. *Nature Geoscience*, 8(8):625–628.

Haran, T., Bohlander, J., Fahnestock, M., Painter, T., and Scambos, T. (2014). MODIS Mosaic of Antarctica 2008-2009 (MOA2009) Image Map.

Harrison, S., Bartlein, P., Brewer, S., Prentice, I., Boyd, M., Hessler, I., Holmgren, K., Izumi, K., and Willis, K. (2014). Climate model benchmarking with glacial and mid-Holocene climates. *Climate Dynamics*, 43(3-4):671–688.

Hawkins, E. and Sutton, R. (2009). The potential to narrow uncertainty in regional climate predictions. *Bulletin of the American Meteorological Society*, 90(8):1095–1108.

Hays, J. D., Imbrie, J., and Shackleton, N. J. (1976). Variations in the Earth's orbit: Pacemaker of the Ice Ages: For 500 000 years, major climatic changes have followed variations in obliquity and precession. *science*, 194(4270):1121–1132.

He, F., Shakun, J. D., Clark, P. U., Carlson, A. E., Liu, Z., Otto-Bliesner, B. L., and Kutzbach, J. E. (2013). Northern Hemisphere forcing of Southern Hemisphere climate during the last deglaciation. *Nature*, 494(7435):81–85.

Hillenbrand, C.-D., Bentley, M. J., Stolldorf, T. D., Hein, A. S., Kuhn, G., Graham, A. G., Fogwill, C. J., Kristoffersen, Y., Smith, J. A., Anderson, J. B., Larter, R., Melles, M., Hodgson, D., Mulvaney, R., and Sugden, D. (2014). Reconstruction of changes in the

Weddell Sea sector of the Antarctic Ice Sheet since the Last Glacial Maximum. *Quaternary Science Reviews*, 100:111–136.

Houtekamer, P. L., Mitchell, H. L., Pellerin, G., Buehner, M., Charron, M., Spacek, L., and Hansen, B. (2005). Atmospheric data assimilation with an ensemble Kalman filter: Results with real observations. *Monthly weather review*, 133(3):604–620.

Hurrell, J. W., Hack, J. J., Shea, D., Caron, J. M., and Rosinski, J. (2008). A new sea surface temperature and sea ice boundary dataset for the Community Atmosphere Model. *Journal of Climate*, 21(19):5145–5153.

Huybers, P. and Wunsch, C. (2004). A depth-derived Pleistocene age model: Uncertainty estimates, sedimentation variability, and nonlinear climate change. *Paleoceanography*, 19(1).

Huybrechts, P. (2002). Sea-level changes at the LGM from ice-dynamic reconstructions of the Greenland and Antarctic ice sheets during the glacial cycles. *Quaternary Science Reviews*, 21(1-3):203–231.

Huybrechts, P., Letreguilly, A., and Reeh, N. (1991). The Greenland ice sheet and greenhouse warming. *Palaeogeography, Palaeoclimatology, Palaeoecology*, 89(4):399–412.

Ivy-Ochs, S. and Kober, F. (2008). Surface exposure dating with cosmogenic nuclides. *E&G Quaternary Science Journal*, 57(1/2):179–209.

Jacobel, R. W., Welch, B. C., Steig, E. J., and Schneider, D. P. (2005). Glaciological and climatic significance of Hercules Dome, Antarctica: An optimal site for deep ice core drilling. *Journal of Geophysical Research: Earth Surface*, 110(F1).

Johnsen, S., Dansgaard, W., and White, J. (1989). The origin of Arctic precipitation under present and glacial conditions. *Tellus B: Chemical and Physical Meteorology*, 41(4):452–468.

Johnsen, S. J., Clausen, H. B., Dansgaard, W., Gundestrup, N. S., Hammer, C. U., Andersen, U., Andersen, K. K., Hvidberg, C. S., Dahl-Jensen, D., Steffensen, J. P., Shoji, H., Sveinbjörnsdóttir, Á. E., White, J., Jouzel, J., and Fisher, D. (1997). The δ18O record along the Greenland Ice Core Project deep ice core and the problem of possible Eemian climatic instability. *Journal of Geophysical Research: Oceans*, 102(C12):26397–26410.

Johnson, J. A., Kuhl, T., Boeckmann, G., Gibson, C., Jetson, J., Meulemans, Z., Slawny, K., and Souney, J. M. (2021). Drilling operations for the South Pole Ice core (SPICEcore) project. *Annals of Glaciology*, 62(84):75–88.

Jouzel, J., Alley, R. B., Cuffey, K., Dansgaard, W., Grootes, P., Hoffmann, G., Johnsen, S. J., Koster, R., Peel, D., Shuman, C., Stievenard, M., Stuiver, M., and White, J. (1997). Validity of the temperature reconstruction from water isotopes in ice cores. *Journal of Geophysical Research: Oceans*, 102(C12):26471–26487.

Jouzel, J., Vimeux, F., Caillon, N., Delaygue, G., Hoffmann, G., Masson-Delmotte, V., and Parrenin, F. (2003). Magnitude of isotope/temperature scaling for interpretation of central Antarctic ice cores. *Journal of Geophysical Research: Atmospheres*, 108(D12).

Kageyama, M., Albani, S., Braconnot, P and, H. S., Hopcroft, P., Ivanovic, RF and, L. F., Marti, O., Peltier, W., Peterschmitt, J.-Y., Roche, D., Tarasov, L., Zhang, X., Brady, E., Haywood, A., LeGrande, A., Lunt, D., Mahowald, N., Mikolajewicz, U., Nisancioglu, K., Otto-Bliesner, B., Renssen, H., Tomas, R., Zhang, Q., Abe-Ouchi, A., Bartlein, PJ and, C. J., Li, Q., Lohmann, G., Ohgaito, R., Shi, X., Volodin, E., Yoshida, K., Zhang, X., and Zheng, W. (2017). The PMIP4 contribution to CMIP6–Part 4: Scientific objectives and experimental design of the PMIP4-CMIP6 Last Glacial Maximum experiments and PMIP4 sensitivity experiments. *Geoscientific Model Development*, 10(11):4035–4055.

Kahle, E. C., Steig, E. J., Jones, T. R., Fudge, T., Koutnik, M. R., Morris, V. A., Vaughn, B. H., Schauer, A. J., Stevens, C. M., Conway, H., Waddington, E., Buizert, C., Epifanio, J., and White, J. (2021). Reconstruction of temperature, accumulation rate, and layer

thinning from an ice core at South Pole, using a statistical inverse method. *Journal of Geophysical Research: Atmospheres*, 126(13):e2020JD033300.

Kalnay, E., Kanamitsu, M., Kistler, R., Collins, W., Deaven, D., Gandin, L., Iredell, M., Saha, S., White, G., Woollen, J., Zhu, Y., Chelliah, M., Ebisuzaki, W., Higgins, W., Janowiak, J., Mo, K., Ropelewski, C., Wang, J., Leetmaa, A., Reynolds, R., Jenne, R., and Joseph, D. (1996). The NCEP/NCAR 40-year reanalysis project. *Bulletin of the American meteorological Society*, 77(3):437–472.

Kapsner, W., Alley, R. B., Shuman, C., Anandakrishnan, S., and Grootes, P. (1995). Dominant influence of atmospheric circulation on snow accumulation in Greenland over the past 18,000 years. *Nature*, 373(6509):52–54.

Kaufman, D., Ager, T., Anderson, N., Anderson, P., Andrews, J., Bartlein, P., Brubaker, L., Coats, L., Cwynar, L., Duvall, M., Dyke, A., Edwards, M., Eisner, W., Gajewski, K., Geirsdttir, A., Hu, F., Jennings, A., Kaplan, M., Kerwin, M., Lozhkin, A., MacDonald, G., Miller, G., Mock, C., Oswald, W., Otto-Bliesner, B., Porinchu, D., Rhland, K., Smol, J., Steig, E., and Wolfe, B. (2004). Holocene thermal maximum in the western Arctic (0–180 W). *Quaternary Science Reviews*, 23(5-6):529–560.

Khan, S. A., Aschwanden, A., Bjørk, A. A., Wahr, J., Kjeldsen, K. K., and Kjær, K. H. (2015). Greenland ice sheet mass balance: A review. *Reports on progress in physics*, 78(4):046801.

Kindler, P., Guillevic, M., Baumgartner, M. F., Schwander, J., Landais, A., and Leuenberger, M. (2014). Temperature reconstruction from 10 to 120 kyr b2k from the NGRIP ice core. *Climate of the Past*, 10(2):887–902.

Kobashi, T., Menviel, L., Jeltsch-Thömmes, A., Vinther, B. M., Box, J. E., Muscheler, R., Nakaegawa, T., Pfister, P. L., Döring, M., Leuenberger, M., Wanner, H., and Ohmura, A.

(2017). Volcanic influence on centennial to millennial Holocene Greenland temperature change. *Scientific reports*, 7(1441).

Koutnik, M. R., Fudge, T., Conway, H., Waddington, E. D., Neumann, T. A., Cuffey, K. M., Buizert, C., and Taylor, K. C. (2016). Holocene accumulation and ice flow near the West Antarctic Ice Sheet Divide ice core site. *Journal of Geophysical Research: Earth Surface*, 121(5):907–924.

Krinner, G., Raynaud, D., Doutriaux, C., and Dang, H. (2000). Simulations of the Last Glacial Maximum ice sheet surface climate: Implications for the interpretation of ice core air content. *Journal of Geophysical Research: Atmospheres*, 105(D2):2059–2070.

Krinner, G. and Werner, M. (2003). Impact of precipitation seasonality changes on isotopic signals in polar ice cores: A multi-model analysis. *Earth and Planetary Science Letters*, 216(4):525–538.

Lachlan-Cope, T. (2010). Antarctic clouds. *Polar Research*, 29(2):150–158.

Langen, P., Mottram, R., Christensen, J., Boberg, F., Rodehacke, C., Stendel, M., Van As, D., Ahlstrøm, A., Mortensen, J., Rysgaard, S., Petersen, D., Svendsen, K., Aðalgeirsdóttir, G., and Cappelen, J. (2015). Quantifying energy and mass fluxes controlling Godthåbsfjord freshwater input in a 5-km simulation (1991–2012). *Journal of Climate*, 28(9):3694–3713.

Langen, P. L., Fausto, R. S., Vandecrux, B., Mottram, R. H., and Box, J. E. (2017). Liquid water flow and retention on the Greenland ice sheet in the regional climate model HIRHAM5: Local and large-scale impacts. *Frontiers in Earth Science*, 4(110).

Larter, R. D., Anderson, J. B., Graham, A. G., Gohl, K., Hillenbrand, C.-D., Jakobsson, M., Johnson, J. S., Kuhn, G., Nitsche, F. O., Smith, J. A., Witus, A., Bentley, M., Dowdeswell, J., Ehrmann, W., Klages, J., Lindow, J., Cofaigh, C., and Speigel, C. (2014). Reconstruction of changes in the Amundsen Sea and Bellingshausen Sea sector of the

West Antarctic ice sheet since the last glacial maximum. *Quaternary Science Reviews*, 100:55–86.

Lasher, G. E., Axford, Y., McFarlin, J. M., Kelly, M. A., Osterberg, E. C., and Berkelhammer, M. B. (2017). Holocene temperatures and isotopes of precipitation in Northwest Greenland recorded in lacustrine organic materials. *Quaternary Science Reviews*, 170:45–55.

Latif, M. and Keenlyside, N. S. (2011). A perspective on decadal climate variability and predictability. *Deep Sea Research Part II: Topical Studies in Oceanography*, 58(17-18):1880–1894.

Lecavalier, B. S., Fisher, D. A., Milne, G. A., Vinther, B. M., Tarasov, L., Huybrechts, P., Lacelle, D., Main, B., Zheng, J., Bourgeois, J., and Dyke, A. (2017). High Arctic Holocene temperature record from the Agassiz ice cap and Greenland ice sheet evolution. *Proceedings of the National Academy of Sciences*, 114(23):5952–5957.

Lecavalier, B. S., Milne, G. A., Simpson, M. J., Wake, L., Huybrechts, P., Tarasov, L., Kjeldsen, K. K., Funder, S., Long, A. J., Woodroffe, S., Dyke, A., and Larsen, N. (2014). A model of Greenland ice sheet deglaciation constrained by observations of relative sea level and ice extent. *Quaternary Science Reviews*, 102:54–84.

Lesnek, A. J. and Briner, J. P. (2018). Response of a land-terminating sector of the western Greenland Ice Sheet to early Holocene climate change: Evidence from ^{10}Be dating in the Søndre Isortoq region. *Quaternary Science Reviews*, 180:145–156.

Lesnek, A. J., Briner, J. P., Young, N. E., and Cuzzone, J. K. (2020). Maximum southwest Greenland Ice Sheet recession in the early Holocene. *Geophysical Research Letters*, 47(1):e2019GL083164.

Liu, Z., Carlson, A. E., He, F., Brady, E. C., Otto-Bliesner, B. L., Briegleb, B. P., Wehrenberg, M., Clark, P. U., Wu, S., Cheng, J., Zhang, J., Noone, D., and Zhu, J. (2012).

Younger Dryas cooling and the Greenland climate response to CO_2. *Proceedings of the National Academy of Sciences*, 109(28):11101–11104.

Liu, Z., Otto-Bliesner, B., He, F., Brady, E., Tomas, R., Clark, P., Carlson, A., Lynch-Stieglitz, J., Curry, W., Brook, E., Erickson, D., Jacob, R., Kutzbach, J., and Cheng, J. (2009). Transient simulation of last deglaciation with a new mechanism for Bølling-Allerød warming. *Science*, 325(5938):310–314.

Lliboutry, L. (1979). A critical review of analytical approximate solutions for steady state velocities and temperatures in cold ice-sheets. *Gletscherkd. Glazialgeol.*, 15(2):135–148.

Lythe, M. B. and Vaughan, D. G. (2001). BEDMAP: A new ice thickness and subglacial topographic model of Antarctica. *Journal of Geophysical Research: Solid Earth*, 106(B6):11335–11351.

Marshall, S. J. and Cuffey, K. M. (2000). Peregrinations of the Greenland Ice Sheet divide in the last glacial cycle: Implications for central Greenland ice cores. *Earth and Planetary Science Letters*, 179(1):73–90.

Martinerie, P., Lipenkov, V. Y., Raynaud, D., Chappellaz, J., Barkov, N., and Lorius, C. (1994). Air content paleo record in the Vostok ice core (Antarctica): A mixed record of climatic and glaciological parameters. *Journal of Geophysical Research: Atmospheres*, 99(D5):10565–10576.

Masson-Delmotte, V., Buiron, D., Ekaykin, A., Frezzotti, M., Gallée, H., Jouzel, J., Krinner, G., Landais, A., Motoyama, H., Oerter, H., Pol, K., Pollard, D., Ritz, C., Schlosser, E., Sime, L., Sodemann, H., Stenni, B., Uemura, R., and Vimeux, F. (2011). A comparison of the present and last interglacial periods in six Antarctic ice cores. *Climate of the Past*, 7(2):397–423.

Masson-Delmotte, V., Hou, S., Ekaykin, A., Jouzel, J., Aristarain, A., Bernardo, R., Bromwich, D., Cattani, O., Delmotte, M., Falourd, S., Frezzotti, M., Gallée, H., Genoni,

L., Isaksson, E., Landaisa, A., Helsen, M., Hoffmann, G., Lopez, J., Morgan, V., Motoyama, H., Noone, D., Oerter, H., Petit, J., Royer, A., Uemura, R., Schmidt, G., Schlosser, E., Simões, J., Steig, E., Stenni, B., Stievenard, M., van den Broeke, M., van de Wall, R., ven de Berg, W., Vimeux, F., and White, J. (2008). A review of Antarctic surface snow isotopic composition: Observations, atmospheric circulation, and isotopic modeling. *Journal of climate*, 21(13):3359–3387.

Masson-Delmotte, V., Kageyama, M., Braconnot, P., Charbit, S., Krinner, G., Ritz, C., Guilyardi, E., Jouzel, J., Abe-Ouchi, A., Crucifix, M., Gladstone, R., Hewitt, C., Kitoh, A., LeGrande, A., Marti, O., Merkel, U., Motoi, T., Ohgaito, R., Otto-Bliesner, B., Peltier, W., Ross, I., Valdes, P., Vettoretti, G., Weber, S., Wolk, F., and Yu, Y. (2006). Past and future polar amplification of climate change: climate model intercomparisons and ice-core constraints. *Climate Dynamics*, 26(5):513–529.

McFarlin, J. M., Axford, Y., Osburn, M. R., Kelly, M. A., Osterberg, E. C., and Farnsworth, L. B. (2018). Pronounced summer warming in northwest Greenland during the Holocene and Last Interglacial. *Proceedings of the National Academy of Sciences*, 115(25):6357–6362.

Meese, D. A., Gow, A., Grootes, P., Stuiver, M., Mayewski, P. A., Zielinski, G., Ram, M., Taylor, K., and Waddington, E. (1994). The accumulation record from the GISP2 core as an indicator of climate change throughout the Holocene. *Science*, 266(5191):1680–1682.

Meyer, H. W. (2007). A review of paleotemperature–lapse rate methods for estimating paleoelevation from fossil floras. *Reviews in Mineralogy and Geochemistry*, 66(1):155–171.

Montagnat, M., Azuma, N., Dahl-Jensen, D., Eichler, J., Fujita, S., Gillet-Chaulet, F., Kipfstuhl, S., Samyn, D., Svensson, A., and Weikusat, I. (2014). Fabric along the NEEM ice core, Greenland, and its comparison with GRIP and NGRIP ice cores. *The Cryosphere*, 8(4):1129–1138.

Morlighem, M., Rignot, E., Binder, T., Blankenship, D., Drews, R., Eagles, G., Eisen, O.,

Ferraccioli, F., Forsberg, R., Fretwell, P., Goel, V., Greenbaum, J., Gudmundsson, H., Guo, J., Helm, V., Hofstede, C., Howat, I., Humbert, A., Jokat, W., Karlsson, N., Lee, W., Matsuoka, K., Millan, R., Mouginot, J., Paden, J., Pattyn, F., Roberts, J., Rosier, S., Ruppel, A., Seroussi, H., Smith, E., Steinhage, D., Sun, B., van den Broeke, M., van Ommen, T., van Wessem, M., and Young, D. (2020). Deep glacial troughs and stabilizing ridges unveiled beneath the margins of the Antarctic ice sheet. *Nature Geoscience*, 13(2):132–137.

Morlighem, M., Williams, C. N., Rignot, E., An, L., Arndt, J. E., Bamber, J. L., Catania, G., Chauché, N., Dowdeswell, J. A., Dorschel, B., Fenty, I., Hogan, K., Howat, I., Hubbard, A., Jakobsson, M., Jordan, T., Kjeldsen, K., Millan, R., Mayer, L., Mouginot, J., Noël, B., O'Cofaigh, C., Palmer, S., Rysgaard, S., Seroussi, H., Siegert, M., Slabon, P., Straneo, F., van den Broeke, M., Weinrebe, W., Wood, M., and Zinglersen, K. (2017). BedMachine v3: Complete bed topography and ocean bathymetry mapping of Greenland from multibeam echo sounding combined with mass conservation. *Geophysical research letters*, 44(21):11–051.

Nash, J. and Sutcliffe, J. (1970). River forcasting using conceptual models, 1. a discussion of principles. *J. Hydrol*, 10:280–290.

NEEM Community Members (2013). Eemian interglacial reconstructed from a Greenland folded ice core. *Nature*, 493(7433):489–494.

Neumann, T., Conway, H., Price, S., Waddington, E., Catania, G., and Morse, D. (2008). Holocene accumulation and ice sheet dynamics in central West Antarctica. *Journal of Geophysical Research: Earth Surface*, 113(F2).

Nielsen, L. T., Aðalgeirsdóttir, G., Gkinis, V., Nuterman, R., and Hvidberg, C. S. (2018). The effect of a Holocene climatic optimum on the evolution of the Greenland ice sheet during the last 10 kyr. *Journal of Glaciology*, 64(245):477–488.

Nusbaumer, J., Wong, T. E., Bardeen, C., and Noone, D. (2017). Evaluating hydrological processes in the Community Atmosphere Model Version 5 (CAM5) using stable isotope ratios of water. *Journal of Advances in Modeling Earth Systems*, 9(2):949–977.

Nye, J. (1963). Correction factor for accumulation measured by the thickness of the annual layers in an ice sheet. *Journal of Glaciology*, 4(36):785–788.

Okazaki, A. and Yoshimura, K. (2017). Development and evaluation of a system of proxy data assimilation for paleoclimate reconstruction. *Climate of the Past*, 13(4).

Okazaki, A. and Yoshimura, K. (2019). Global evaluation of proxy system models for stable water isotopes with realistic atmospheric forcing. *Journal of Geophysical Research: Atmospheres*, 124(16):8972–8993.

Osman, M. B., Tierney, J. E., Zhu, J., Tardif, R., Hakim, G. J., King, J., and Poulsen, C. J. (2021). Globally resolved surface temperatures since the Last Glacial Maximum. *Nature*, 599(7884):239–244.

Osterberg, E., Badgeley, J., Buizert, C., D'Andrilli, J., Fudge, T., Jones, T. R., Kreutz, K., Petrenko, V., Pettit, E., and Winski, D. (2020). IDP Ice Core Working Group (IDP-ICWG): Ice core research priorities in Greenland. Technical report, Virtual.

PAGES 2k-PMIP3 group (2015). Continental-scale temperature variability in PMIP3 simulations and PAGES 2k regional temperature reconstructions over the past millennium. *Climate of the Past*, 11(12):1673–1699.

Parrenin, F., Masson-Delmotte, V., Köhler, P., Raynaud, D., Paillard, D., Schwander, J., Barbante, C., Landais, A., Wegner, A., and Jouzel, J. (2013). Synchronous change of atmospheric CO_2 and Antarctic temperature during the last deglacial warming. *Science*, 339(6123):1060–1063.

Parrenin, F., Rémy, F., Ritz, C., Siegert, M. J., and Jouzel, J. (2004). New modeling of the Vostok ice flow line and implication for the glaciological chronology of the Vostok ice core. *Journal of Geophysical Research: Atmospheres*, 109(D20).

Parsons, L. A., Amrhein, D. E., Sanchez, S. C., Tardif, R., Brennan, M. K., and Hakim, G. J. (2021). Do multi-model ensembles improve reconstruction skill in paleoclimate data assimilation? *Earth and Space Science*, 8(4):e2020EA001467.

Pausata, F. S. and Löfverström, M. (2015). On the enigmatic similarity in Greenland δ18O between the Oldest and Younger Dryas. *Geophysical Research Letters*, 42(23):10–470.

Peltier, W. R. (2004). Global glacial isostasy and the surface of the ice-age earth: the ICE-5G (VM2) model and GRACE. *Annu. Rev. Earth Planet. Sci.*, 32:111–149.

Peltier, W. R., Argus, D., and Drummond, R. (2015). Space geodesy constrains ice age terminal deglaciation: The global ICE-6G_C (VM5a) model. *Journal of Geophysical Research: Solid Earth*, 120(1):450–487.

Perkins, W. and Hakim, G. (2021). Coupled atmosphere–ocean reconstruction of the last millennium using online data assimilation. *Paleoceanography and Paleoclimatology*, 36(5):e2020PA003959.

Pettit, E. C., Jacobson, H. P., and Waddington, E. D. (2003). Effects of basal sliding on isochrones and flow near an ice divide. *Annals of Glaciology*, 37:370–376.

Pollard, D., Chang, W., Haran, M., Applegate, P., and DeConto, R. (2016). Large ensemble modeling of the last deglacial retreat of the West Antarctic Ice Sheet: Comparison of simple and advanced statistical techniques. *Geoscientific Model Development*, 9(5):1697–1723.

Pollard, D. and DeConto, R. (2012). Description of a hybrid ice sheet-shelf model, and application to Antarctica. *Geoscientific Model Development*, 5(5):1273–1295.

Randall, D. A. (2009). The moist adiabatic lapse rate.

Rasmussen, S. O., Abbott, P., Blunier, T., Bourne, A., Brook, E. J., Buchardt, S. L., Buizert, C., Chappellaz, J., Clausen, H. B., Cook, E., Dahl-Jensen, D., Davies, S., Guillevic, M., Kipfstuhl, S., Laepple, T., Seierstad, I., Severinghaus, J., Steffensen, J., Stowasser, C., Svensson, A., Vallelonga, P., Vinther, B., Wilhelms, F., and Winstrup, M. (2013). A first chronology for the North Greenland Eemian Ice Drilling (NEEM) ice core. *Climate of the Past*, 9(6).

Rasmussen, S. O., Andersen, K. K., Svensson, A., Steffensen, J., Vinther, B. M., Clausen, H. B., Siggaard-Andersen, M.-L., Johnsen, S. J., Larsen, L. B., Dahl-Jensen, D., Bigler, M., Röthlisberger, R., Fischer, H., Goto-Azuma, K., Hansson, M., and Ruth, U. (2006). A new Greenland ice core chronology for the last glacial termination. *Journal of Geophysical Research: Atmospheres*, 111(D6).

Rasmussen, S. O., Bigler, M., Blockley, S. P., Blunier, T., Buchardt, S. L., Clausen, H. B., Cvijanovic, I., Dahl-Jensen, D., Johnsen, S. J., Fischer, H., Gkinis, V., Guillevic, M., Hoek, W. Z., Lowe, J. J., Pedro, J. B., Popp, T., Seierstad, I. K., Steffensen, J. P., Svensson, A. M., Vallelonga, P., Vinther, B. M., Walker, M. J., Wheatley, J. J., and Winstrup, M. (2014). A stratigraphic framework for abrupt climatic changes during the Last Glacial period based on three synchronized Greenland ice-core records: Refining and extending the intimate event stratigraphy. *Quaternary Science Reviews*, 106:14–28.

Raymond, C. F. (1983). Deformation in the vicinity of ice divides. *Journal of Glaciology*, 29(103):357–373.

Raynaud, D., Lipenkov, V., Lemieux-Dudon, B., Duval, P., Loutre, M.-F., and Lhomme, N. (2007). The local insolation signature of air content in Antarctic ice: A new step toward an absolute dating of ice records. *Earth and Planetary Science Letters*, 261(3-4):337–349.

Raynaud, D. and Whillans, I. (1982). Air content of the Byrd core and past changes in the West Antarctic ice sheet. *Annals of Glaciology*, 3:269–273.

Raynaud, D., L.-B. (1979). Total gas content and surface elevation of polar ice sheets. *Nature*, 281:289–291.

Reeh, N. and Fisher, D. (1983). Noise in accumulation rate and δ^{18}O time series as determined from comparison of adjacent Greenland and Devon Island ice cap cores. *Ottawa, Polar Continental Shelf Project (Internal Report).*

Reeh, N., Johnsen, S., Dahl-Jensen, D., Langway, C., Oeschger, H., and Dansgaard, W. (1985). Dating the Dye 3 deep ice core by flow model calculations. *Greenland ice core: geophysics, geochemistry and the environment*, 33:57–65.

Rignot, E., Casassa, G., Gogineni, P., Krabill, W., Rivera, A., and Thomas, R. (2004). Accelerated ice discharge from the Antarctic Peninsula following the collapse of Larsen B ice shelf. *Geophysical research letters*, 31(18).

Robin, G. d. Q. (1977). Ice cores and climatic change. *Philosophical Transactions of the Royal Society of London. B, Biological Sciences*, 280(972):143–168.

Roe, G. H. and Lindzen, R. S. (2001). The mutual interaction between continental-scale ice sheets and atmospheric stationary waves. *Journal of Climate*, 14(7):1450–1465.

Ross, N., Siegert, M., Woodward, J., Smith, A. M., Corr, H. F., Bentley, M., Hindmarsh, R. C., King, E. C., and Rivera, A. (2011). Holocene stability of the Amundsen-Weddell ice divide, West Antarctica. *Geology*, 39(10):935–938.

Rowley, D. B. (2007). Stable isotope-based paleoaltimetry: Theory and validation. *Reviews in Mineralogy and Geochemistry*, 66(1):23–52.

Roy, K. and Peltier, W. (2018). Relative sea level in the western mediterranean basin: a regional test of the ICE-7G_NA (VM7) model and a constraint on late Holocene Antarctic deglaciation. *Quaternary Science Reviews*, 183:76–87.

Schaefer, J. M., Finkel, R. C., Balco, G., Alley, R. B., Caffee, M. W., Briner, J. P., Young, N. E., Gow, A. J., and Schwartz, R. (2016). Greenland was nearly ice-free for extended periods during the Pleistocene. *Nature*, 540(7632):252–255.

Schneider von Deimling, T., Ganopolski, A., Held, H., and Rahmstorf, S. (2006). How cold was the last glacial maximum? *Geophysical Research Letters*, 33(14).

Schoof, C. (2007). Ice sheet grounding line dynamics: Steady states, stability, and hysteresis. *Journal of Geophysical Research: Earth Surface*, 112(F3).

Schüpbach, S., Fischer, H., Bigler, M., Erhardt, T., Gfeller, G., Leuenberger, D., Mini, O., Mulvaney, R., Abram, N. J., Fleet, L., Frey, M. M., Thomas, E., Svensson, A., Dahl-Jensen, D., Kettner, E., Kjaer, H., Seierstad, I., Steffensen, J. P., Rasmussen, S. O., Vallelonga, P., Winstrup, M., Wegner, A., Twarloh, B., Wolff, K., Schmidt, K., Goto-Azuma, K., Kuramoto, T., Hirabayashi, M., Uetake, J., Zheng, J., Bourgeois, J., Fisher, D., Zhiheng, D., Xiao, C., Legrand, M., Spolaor, A., Gabrieli, J., Barbante, C., Kang, J.-H., Hur, S. D., Hong, S. B., Hwang, H. J., Hong, S., Hansson, M., Iizuka, Y., Oyabu, I., Muscheler, R., Adolphi, F., Maselli, O., McConnell, J., and Wolff, E. W. (2018). Greenland records of aerosol source and atmospheric lifetime changes from the Eemian to the Holocene. *Nature communications*, 9(1476).

Severinghaus, J. P. and Brook, E. J. (1999). Abrupt climate change at the end of the last glacial period inferred from trapped air in polar ice. *Science*, 286(5441):930–934.

Severinghaus, J. P., Sowers, T., Brook, E. J., Alley, R. B., and Bender, M. L. (1998). Timing of abrupt climate change at the end of the Younger Dryas interval from thermally fractionated gases in polar ice. *Nature*, 391(6663):141–146.

Sigl, M., Fudge, T. J., Winstrup, M., Cole-Dai, J., Ferris, D., McConnell, J. R., Taylor, K. C., Welten, K. C., Woodruff, T. E., Adolphi, F., Bisiauz, M., Brook, E., Buizert, C., Caffee, M., Dunbar, N., Edwards, R., Geng, L., Iverson, N., Koffman, B., Layman, L., Maselli,

O., McGwire, K., Muscheler, R., Nishiizumi, K., Pasteris, D., Rhodes, R., and Sowers, T. (2016). The WAIS Divide deep ice core WD2014 chronology–part 2: Annual-layer counting (0–31 ka BP). *Climate of the Past*, 12(3):769–786.

Simpson, M. J., Milne, G. A., Huybrechts, P., and Long, A. J. (2009). Calibrating a glaciological model of the Greenland ice sheet from the Last Glacial Maximum to present-day using field observations of relative sea level and ice extent. *Quaternary Science Reviews*, 28(17-18):1631–1657.

Souney, J. M., Twickler, M. S., Aydin, M., Steig, E. J., Fudge, T., Street, L. V., Nicewonger, M. R., Kahle, E. C., Johnson, J. A., Kuhl, T. W., Casey, K., Fegyveresi, J., Nunn, R., and Hargreaves, G. (2021). Core handling, transportation and processing for the South Pole ice core (SPICEcore) project. *Annals of Glaciology*, 62(84):118–130.

Spector, P., Stone, J., Cowdery, S. G., Hall, B., Conway, H., and Bromley, G. (2017). Rapid early-Holocene deglaciation in the Ross Sea, Antarctica. *Geophysical Research Letters*, 44(15):7817–7825.

Spector, P., Stone, J., and Goehring, B. (2019). Thickness of the divide and flank of the West Antarctic Ice Sheet through the last deglaciation. *The Cryosphere*, 13(11):3061–3075.

Steig, E. J. (1997). How well can we parameterize past accumulation rates in polar ice sheets? *Annals of Glaciology*, 25:418–422.

Steig, E. J., Fastook, J. L., Zweck, C., Goodwin, I. D., Licht, K. J., White, J. W., and Ackert, R. P. (2001). West Antarctic ice sheet elevation changes. *The West Antarctic ice sheet: behavior and environment*, 77:75–90.

Steig, E. J., Grootes, P. M., and Stuiver, M. (1994). Seasonal precipitation timing and ice core records. *Science*, 266(5192):1885–1887.

Steig, E. J., Huybers, K., Singh, H. A., Steiger, N. J., Ding, Q., Frierson, D. M., Popp, T., and White, J. W. (2015). Influence of West Antarctic ice sheet collapse on Antarctic surface climate. *Geophysical Research Letters*, 42(12):4862–4868.

Steiger, N. and Hakim, G. (2015). Multi-time scale data assimilation for atmosphere-ocean state estimates. *Clim. Past Discuss*, 11(4):3729–3757.

Steiger, N. J., Steig, E. J., Dee, S. G., Roe, G. H., and Hakim, G. J. (2017). Climate reconstruction using data assimilation of water isotope ratios from ice cores. *Journal of Geophysical Research: Atmospheres*, 122(3):1545–1568.

Stenni, B., Masson-Delmotte, V., Selmo, E., Oerter, H., Meyer, H., Röthlisberger, R., Jouzel, J., Cattani, O., Falourd, S., Fischer, H., Hoffmann, G., Iacumin, P., Johnsen, S., Minster, B., and Udisti, R. (2010). The deuterium excess records of EPICA Dome C and Dronning Maud Land ice cores (East Antarctica). *Quaternary Science Reviews*, 29(1-2):146–159.

Stone, J. O., Balco, G. A., Sugden, D. E., Caffee, M. W., Sass III, L. C., Cowdery, S. G., and Siddoway, C. (2003). Holocene deglaciation of Marie Byrd land, west Antarctica. *Science*, 299(5603):99–102.

Stuiver, M. and Grootes, P. M. (2000). GISP2 oxygen isotope ratios. *Quaternary Research*, 53(3):277–284.

Sutter, J., Fischer, H., and Eisen, O. (2021). Investigating the internal structure of the Antarctic ice sheet: The utility of isochrones for spatiotemporal ice-sheet model calibration. *The Cryosphere*, 15(8):3839–3860.

Svensson, A., Andersen, K. K., Bigler, M., Clausen, H. B., Dahl-Jensen, D., Davies, S. M., Johnsen, S. J., Muscheler, R., Rasmussen, S. O., Röthlisberger, R., Steffensen, J., and Vinther, B. (2006). The Greenland ice core chronology 2005, 15–42 ka. Part 2: Comparison to other records. *Quaternary Science Reviews*, 25(23-24):3258–3267.

Tardif, R., Hakim, G. J., Perkins, W. A., Horlick, K. A., Erb, M. P., Emile-Geay, J., Anderson, D. M., Steig, E. J., and Noone, D. (2019). Last Millennium Reanalysis with an expanded proxy database and seasonal proxy modeling. *Climate of the Past*, 15(4):1251–1273.

Taylor, K. E., Stouffer, R. J., and Meehl, G. A. (2012). An overview of CMIP5 and the experiment design. *Bulletin of the American meteorological Society*, 93(4):485–498.

Teutschbein, C. and Seibert, J. (2012). Bias correction of regional climate model simulations for hydrological climate-change impact studies: Review and evaluation of different methods. *Journal of hydrology*, 456:12–29.

The RAISED Consortium (2014). A community-based geological reconstruction of Antarctic Ice Sheet deglaciation since the Last Glacial Maximum. *Quaternary Science Reviews*, 100:1–9.

Thorsteinsson, T., Waddington, E., Taylor, K., Alley, R. B., and Blankenship, D. D. (1999). Strain-rate enhancement at Dye 3, Greenland. *Journal of Glaciology*, 45(150):338–345.

Tierney, J. E., Zhu, J., King, J., Malevich, S. B., Hakim, G. J., and Poulsen, C. J. (2020). Glacial cooling and climate sensitivity revisited. *Nature*, 584(7822):569–573.

Todd, C., Stone, J., Conway, H., Hall, B., and Bromley, G. (2010). Late Quaternary evolution of Reedy Glacier, Antarctica. *Quaternary Science Reviews*, 29(11-12):1328–1341.

U.S. Geological Survey (1996). GTOPO30.

Vinther, B. M., Buchardt, S. L., Clausen, H. B., Dahl-Jensen, D., Johnsen, S. J., Fisher, D., Koerner, R., Raynaud, D., Lipenkov, V., Andersen, K. K., Blunier, T., Rasmussen, S., Steffensen, J., and Svensson, A. (2009). Holocene thinning of the Greenland ice sheet. *Nature*, 461(7262):385–388.

Vinther, B. M., Clausen, H. B., Fisher, D., Koerner, R., Johnsen, S. J., Andersen, K. K., Dahl-Jensen, D., Rasmussen, S. O., Steffensen, J. P., and Svensson, A. (2008). Synchronizing ice cores from the Renland and Agassiz ice caps to the Greenland Ice Core Chronology. *Journal of Geophysical Research: Atmospheres*, 113(D8).

Vinther, B. M., Clausen, H. B., Johnsen, S. J., Rasmussen, S. O., Andersen, K. K., Buchardt, S. L., Dahl-Jensen, D., Seierstad, I. K., Siggaard-Andersen, M.-L., Steffensen, J., Svensson, A., Olsen, J., and Heinemeier, J. (2006). A synchronized dating of three greenland ice cores throughout the Holocene. *Journal of Geophysical Research: Atmospheres*, 111(D13).

Vizcaino, M., Mikolajewicz, U., Ziemen, F., Rodehacke, C. B., Greve, R., and Van Den Broeke, M. R. (2015). Coupled simulations of Greenland Ice Sheet and climate change up to ad 2300. *Geophysical Research Letters*, 42(10):3927–3935.

WAIS Divide Project Members (2013). Onset of deglacial warming in West Antarctica driven by local orbital forcing. *Nature*, 500(7463):440–444.

Wallace, J. M. and Hobbs, P. V. (2006). *Atmospheric science: An introductory survey*, volume 92. Elsevier.

Werner, M., Jouzel, J., Masson-Delmotte, V., and Lohmann, G. (2018). Reconciling glacial Antarctic water stable isotopes with ice sheet topography and the isotopic paleothermometer. *Nature communications*, 9(1):1–10.

Werner, M., Mikolajewicz, U., Heimann, M., and Hoffmann, G. (2000). Borehole versus isotope temperatures on Greenland: Seasonality does matter. *Geophysical Research Letters*, 27(5):723–726.

Whillans, I. M., Jezek, K., Drew, A., and Gundestrup, N. (1984). Ice flow leading to the deep core hole at Dye 3, Greenland. *Annals of Glaciology*, 5:185–190.

Whitaker, J. S. and Hamill, T. M. (2002). Ensemble data assimilation without perturbed observations. *Monthly Weather Review*, 130(7):1913–1924.

Whitehouse, P. L., Bentley, M. J., and Le Brocq, A. M. (2012). A deglacial model for Antarctica: geological constraints and glaciological modelling as a basis for a new model of Antarctic glacial isostatic adjustment. *Quaternary Science Reviews*, 32:1–24.

Young, N. E. and Briner, J. P. (2015). Holocene evolution of the western Greenland Ice Sheet: Assessing geophysical ice-sheet models with geological reconstructions of ice-margin change. *Quaternary Science Reviews*, 114:1–17.

Young, N. E., Briner, J. P., Miller, G. H., Lesnek, A. J., Crump, S. E., Thomas, E. K., Pendleton, S. L., Cuzzone, J., Lamp, J., Zimmerman, S., Caffee, M., and Schaefer, J. (2020). Deglaciation of the Greenland and Laurentide ice sheets interrupted by glacier advance during abrupt coolings. *Quaternary Science Reviews*, 229:106091.

Young, N. E., Lesnek, A. J., Cuzzone, J. K., Briner, J. P., Badgeley, J. A., Balter-Kennedy, A., Graham, B. L., Cluett, A., Lamp, J. L., Schwartz, R., Tuna, T., Bard, E., Caffee, M. W., Zimmerman, S. R. H., and Schaefer, J. M. (2021). In situ cosmogenic ^{10}Be–^{14}C–^{26}Al measurements from recently deglaciated bedrock as a new tool to decipher changes in Greenland Ice Sheet size. *Climate of the Past*, 17(1):419–450.

Zhu, J., Liu, Z., Brady, E., Otto-Bliesner, B., Zhang, J., Noone, D., Tomas, R., Nusbaumer, J., Wong, T., Jahn, A., and Tabor, C. (2017). Reduced ENSO variability at the LGM revealed by an isotope-enabled Earth system model. *Geophysical Research Letters*, 44(13):6984–6992.

Zwally, H. J. and Fiegles, S. (1994). Extent and duration of Antarctic surface melting. *Journal of Glaciology*, 40(136):463–475.

Appendix A

SUPPLEMENTARY INFORMATION FOR "GREENLAND TEMPERATURE AND PRECIPITATION OVER THE LAST 20,000 YEARS USING DATA ASSIMILATION"

A.1 Prior Ensemble Considerations

Here we elaborate on the pros and cons of four prior ensemble options we considered before deciding on the one that we use in this study (#4).

1. For offline data assimilation (i.e., no information passed between assimilation time steps), a justifiable method for choosing the prior ensemble would be to use a 100-member ensemble of 20,000-year climate simulations. These climate simulations would be TraCE-21ka-like (i.e., results from fully-coupled GCMs at T31 resolution or higher), and have varied initial conditions, boundary conditions, and model physics. The prior ensemble for any assimilation time step would be taken from the same time step in the climate simulations, which would lead to a prior ensemble that varies smoothly in time and is a justifiable initial guess for the climate evolution over the past 20,000 years. Though this option is simple, it is not feasible because the computational cost of running even one TraCE-21ka-like simulation remains near computational limits.

2. Given that there is only one TraCE-21ka-like simulation, another method would be to select states from TraCE-21ka that are closest in time to the reconstruction time step. For example, if we were reconstructing the 50-year average centered on the year 5,000 CE, then we would select the 100 states from TraCE-21ka that are closest in time to 5,000 CE. Given that we are working with 50-year averages, this means we would select all the states between 7,500 and 2,500 CE. This method, which we call the "running-window" method, provides a prior that varies smoothly in time and is a justifiable initial estimate for the

climate evolution.

For the running-window method, the variance of the prior ensemble would tend to be small. A prior with small variance would lead to underweighting of the proxy records during assimilation. To avoid this issue, we could use the well-accepted approach of inflating the prior variance (Anderson and Anderson, 1999). However, the use of inflation adds an additional tunable parameter; in this case, it would add an additional parameter per time step. Although inflation can, in principle, be constrained using the ensemble calibration ratio (computed for excluded proxies), we have too few proxy records to meaningfully constrain this parameter without overfitting.

In addition to estimating numerous inflation factors, the running-window method limits us to one estimate of the spatial covariance structure per time step. Thus, we have no way to quantify the uncertainty associated with the prior covariance structure. This could be fixed by expanding the running window and randomly selecting multiple prior ensembles; however, if the running window is expanded enough to create meaningfully different prior ensembles, then Holocene states will leak into glacial prior ensembles (and *vice versa*) and the method essentially becomes the method we use in the paper.

3. To reduce the number of inflation parameters, we could split TraCE-21ka into several distinct time periods. From these time periods, we would randomly select prior ensembles that are only used for the reconstruction of associated assimilation time steps. For example, if we split TraCE-21ka into glacial, transitional, and Holocene periods, then we'd make a glacial prior ensemble that is only used to reconstruct the glacial, a transitional prior ensemble that is only used to reconstruct the transition, and a Holocene prior ensemble that is only used to reconstruct the Holocene. This reduces the number of inflation factors we must estimate to a total of three. A disadvantage, however, is that this makes the prior discontinuous in time, which frequently leads to a discontinuous reconstruction. To adjust the reconstruction and make it continuous requires another source of information. Such post-processing adds an extra layer of complexity.

4. The method used in our study ensures a continuous reconstruction and removes the

need for inflation factors. This method uses the same prior ensemble for all time steps (thus it is continuous) and the includes both glacial and Holocene states, which provides enough variance to appropriately weight the proxy records (thus no inflation is needed). Though the time-invariant prior is a poor estimate of the climate evolution over the last 20,000 years, the proxy records are given enough weight to result in a posterior that captures the large climate changes. In addition, we can quantify the uncertainty associated with the spatial covariance pattern by producing multiple posterior ensembles that each stem from a different prior ensemble. In the paper, we use ten different prior ensembles to quantify this uncertainty. Overall, this method is both feasible and simple, thus providing a first step in developing paleoclimate data assimilation for applications on glacial-interglacial timescales.

In this study, one state in a 100-member prior ensemble is an average over 50 years of the model data; these 100 states are selected randomly from the full length of the simulation. This implies that both glacial and Holocene states are likely to be contained within the same prior ensemble that is used to reconstruct all time steps over the last 20,000 years. A prior ensemble could in principle contain only Holocene states; however, this is not the case for any of the ten prior ensembles we use in the paper. Thus, in reconstructing a time step in the glacial, for example, both glacial and Holocene states are part of the prior ensemble.

A.2 Accumulation Records

Our aim is to develop simple, reproducible accumulation histories that are independent of temperature and water isotope assumptions and span the probable range of uncertainty. We use existing estimates for two sites (GISP2 and NEEM), but for three other sites (GRIP, NGRIP, and Dye3) we use one-dimensional ice-flow modeling to estimate the thinning function and convert measured layer-thickness into accumulation. Each core requires different ice-flow assumptions due to the different glaciological settings. Below we first describe the modeling approach used and then describe the reasoning for the ice-flow parameters chosen for each core.

A.2.1 Model

We use a transient, one-dimensional, ice-flow model to calculate the cumulative vertical strain, termed the thinning function. We represent the vertical velocity profile using the Dansgaard and Johnsen (1969) formulation both because of its ubiquity in calculations of thinning for Greenland ice cores (Dahl-Jensen et al., 2003; Rasmussen et al., 2013; Dahl-Jensen et al., 1993) and it's simplicity:

$$w(z) = -(\dot{b} - \dot{m} - \dot{H})\psi(z) - \dot{m} \tag{A.1}$$

where z is the height above the bed in ice-equivalent meters (i.e. the firn has been compacted to ice), $\dot{b}$ is the accumulation rate, $\dot{m}$ is the melt rate, $\dot{H}$ is the rate of ice-thickness change, and $\psi(z)$ is the vertical velocity shape function computed as:

$$\psi(z) = \frac{f_B z + \frac{1}{2}(1 - f_B)\frac{z^2}{h}}{H - \frac{1}{2}h(1 - f_B)} \text{ for } h \geq z > 0 \tag{A.2}$$

$$\psi(z) = \frac{z - \frac{1}{2}h(1 - f_B)}{H - \frac{1}{2}h(1 - f_B)} \text{ for } H \geq z > h \tag{A.3}$$

following Dahl-Jensen et al. (2003) where h is the distance above bedrock of the Dansgaard and Johnsen (1969) kink height, f_B is the fraction of the horizontal surface velocity due to sliding over the bed, and H is the ice thickness. We assume no ice thickness change, $\dot{H} = 0$, and the f_B and $\dot{m}$ are constant in time with $\dot{b}(t)$ and $h(t)$ being functions of time.

The model is initially run with a constant accumulation history at the modern accumulation rate, and a thinning function is produced. The thinning function is then used with the measured layer thickness to infer a temporally-variable accumulation history. The model is then run with the temporally-variable accumulation history to produce an updated thinning function. This thinning function is then used with the measured layer thickness to infer the final accumulation history. The solution converges without additional iterations needed.

A.2.2 NEEM

We use the accumulation reconstruction for the NEEM ice core from Rasmussen et al. (2013). Through the use of several different reconstruction methods, they developed a mean accu-

mulation record with a two standard-deviation uncertainty envelope. We use their mean as our "moderate" record for the main reanalysis, the high end of their uncertainty envelope as our "high" estimate, and the low end of their uncertainty envelope as our "low" estimate.

A.2.3 GISP2

The GISP2 ice core is located about 26 km from the ice divide at Summit, Greenland. The upper column of ice experiences vertical strain rates associated with flank flow, while ice close to the bed originated near the ice divide where vertical strain rates differ (Cuffey and Clow, 1997). The last 20,000 years of time is contained within the top two-thirds of the total ice thickness leading to a greater certainty in the vertical strain rates required to convert measured layer thickness into accumulation.

We use the accumulation reconstruction for the GISP2 ice core from Cuffey and Clow (1997) that coincides with their simulated 100 km retreat of the ice-sheet margin over the last 14,000 years. This reconstruction contains some uncertainty due to the vertical strain rates and margin-retreat scenario, but it is only weakly sensitive to changes in either one (Cuffey and Clow, 1997). Given these low uncertainties, we use this single accumulation record for our main, high, and low scenarios.

The Cuffey and Clow (1997) accumulation reconstruction is on an earlier depth-age scale (Alley et al., 1993; Meese et al., 1994; Bender et al., 1994). We transfer it onto the GICC05 depth-age scale by interpolating the GICC05 ages onto the accumulation depths and recalculating accumulation using:

$$A_{new} = A_{old}\frac{\lambda_{new}}{\lambda_{old}} \tag{A.4}$$

where A is accumulation, λ is the layer thickness, 'old' refers to the original depth-age scale from Cuffey and Clow (1997) and 'new' refers to the GICC05 depth-age scale. This approach accounts for errors in the depth-age scale while assuming the thinning function, with respect to depth, remains the same as the original record.

A.2.4 GRIP

The GRIP ice core was drilled about 2 km from the true summit of Greenland. The basal temperature is well below freezing (Dahl-Jensen et al., 1998) and thus the melting term in the vertical velocity calculation can be neglected. Despite no Raymond arch being imaged with ice penetrating radar, phase sensitive radar (Gillet-Chaulet et al., 2011) revealed a vertical velocity profile influenced by the divide (i.e., the Raymond effect, Raymond, 1983). This indicates that the present divide position has not been stable long enough for a Raymond arch to develop (Marshall and Cuffey, 2000). The englacial vertical velocity profiles of Gillet-Chaulet et al. (2011) are not at the GRIP site and cannot directly inform our choice of profile. Because GRIP is not directly beneath the ice divide and the divide position has likely not been stable, we use a vertical velocity profile that is transitional between a typical flank profile and a divide profile; this is represented with a Dansgaard-Johnsen kink height of 0.4, which we use from 5 ka to present. Prior to 5 ka, we use a typically flank flow value of 0.1 assuming that the divide position is more than one ice thickness (3 km) away. The onset of divide flow at 5 ka is guided by 1) the inference of Vinther et al. (2009) of small surface elevation change around Greenland after 5 ka suggesting the ice sheet had reached a more stable configuration and 2) the duration of divide flow that could exist without a Raymond arch becoming visible. We use this as our moderate accumulation history and note that it is not sensitive to 1,000 year changes in the onset times of the divide flow.

The divide-like vertical velocity profiles causes more vertical strain near the surface of the ice sheet. Thus, an accumulation reconstruction that uses divide-like flow produces higher accumulation values. To develop the high and low scenarios, we use the divide-like kink height of 0.4 and the flank-like kink height of 0.1, respectively.

A.2.5 NGRIP

The NGRIP ice-core site is located approximately 300 km north of GRIP along the central ridge of the Greenland ice sheet, where the high geothermal flux leads to a significant basal

melt rate of approximately 7.7 mm a^{-1} (Dahl-Jensen et al., 2003). This melt rate should be included in the vertical velocity profile even though its primary influence is near the bed; the melting also suggests the possibility that basal sliding contributes to the surface horizontal velocity. Dahl-Jensen et al. (2003) found an optimal fit to the depth-age relationship with the parameters $h = 0.45$, $f_B = 0.135$, $\dot{m} = 7.7$mm a^{-1}, and $\dot{b} = 0.19$ m a^{-1}. Gkinis et al. (2014) used the diffusion length of water isotopes to infer that these parameters produce too much thinning in the early Holocene, and suggested a linear correction of 25% less thinning to a depth of 2,000 m. A kink height of 0.45 is typically appropriate for ice-flow that is experiencing divide-like flow conditions. It would be unusual to have divide-like flow in a location with significant melt, as the Raymond effect is suppressed by basal sliding (Raymond, 1983; Pettit et al., 2003). We find that a kink-height of 0.2 reproduces the thinning function inferred by Gkinis et al. (2014) quite closely and is more easily interpreted dynamically because this value is expected for a site experiencing typical non-divide flow. The inverse method for inferring optimal model parameters as used by Dahl-Jensen et al. (2003) could be led astray by the assumption of direct scaling between accumulation and water isotopes.

For all scenarios, we use a melt rate of 7.7 mm a^{-1}. There may be small variations in the basal melt rate due to changes in the surface temperature and accumulation forcing and flow over bedrock with a different geothermal flux (Dahl-Jensen et al., 2003); however, any variations in the basal melt rate have a limited impact on the thinning inferred for the upper portion of the ice column. We use a kink height of 0.2 for our moderate scenario. For the high scenario, we use the original values of Dahl-Jensen et al. (2003). For the low scenario, we use a kink height of 0, which is equivalent to using a basal sliding fraction of 1, essentially the Nye model (Nye, 1963).

A.2.6 Dye3

As discussed in the main text, reconstructing the accumulation rate at Dye3 is significantly more challenging than for the other interior ice-core sites. Ice of 20 ka age is much closer

to the bed at Dye3 than at the central Greenland core locations, and has been strained to less than 10% of its original thickness. Complicating matters further, Dye3 was drilled at a site where the current surface velocity is 11 m yr^{-1}; the early Holocene ice has thus flowed many tens of kilometers (Whillans et al., 1984), possibly through significant accumulation variations (Reeh et al., 1985). Dye3 also has a more pronounced difference in ice fabric between the Holocene and glacial ice (Thorsteinsson et al., 1999; Montagnat et al., 2014). To develop the thinning function, we first compute the vertical velocity profile based on the horizontal strain measured with borehole tilt observations (Gundestrup and Hansen, 1984). These produced an accumulation history with an accumulation rate at the onset of the Holocene (11.7 ka) that is less than half of the modern accumulation rate. We consider this to be a low estimate, as the current velocity profile is strongly influenced by the location of the transition between the glacial and Holocene ice. We create a moderate scenario by approximately matching the accumulation rate around 7 ka with the past 1 ka accumulation rate; this uses a kink height of 0.2 which is typical for flank sites. We create a high scenario where we set the accumulation history at 11 ka approximately equal to the past 1 ka. The resulting accumulation histories vary significantly more than those for the interior cores because of the much greater uncertainty in the flow model.

We have not attempted to correct the accumulation history for advection because of the large uncertainties in both the flow path and the pattern of accumulation in the past. We note that we have low confidence in the Dye3 accumulation reconstructions; we include them because they are the only information from southern Greenland.

A.3 Extension of the Dye3 Depth-Age Scale to 20 ka

Here we explain the method we use to determine a Dye3 depth-age scale from 11.7 ka to 20 ka. Following the cross-correlation maximization procedure from Huybers and Wunsch (2004), we match the δ^{18}O record from Dye3 to the δ^{18}O record from NGRIP during this time interval. First we pick approximate tie points between the two δ^{18}O records. We emphasize placing tie points in the middle of high-magnitude, abrupt signals, such as the warming into

the Bolling-Allerod, because these sigmals are most likely to be coherent across the ice sheet. Next we pick signals found in both δ^{18}O records regardless of magnitude and rate of change. We interpolate the depth-age scale between all the picked signals, including the tie points. We do this to achieve a close initial alignment of the two records, which gives us an initial correlation coefficient of 0.69 between the Dye3 and NGRIP δ^{18}O records. We then use the algorithm developed by Huybers and Wunsch (2004) to adjust the Dye3 depth-age scale to achieve a better alignment between these records. As input into the algorithm, we provide an age uncertainty estimate for each tie point and the amount of compression or extension each section between tie points is allowed to undergo. This latter constraint prevents both tie points from crossing and unrealistic changes in the implied accumulation rates. The updated depth-age scale output by this procedure gives a slightly higher correlation coefficient of 0.71.

A.4 Importance of Including a Southern Greenland Ice Core

The Dye3 ice core is an important source of information for capturing southern Greenland climate. For example, we find that posterior ensemble mean compares quite well to independent (excluded) proxy records in central-northern Greenland, like NGRIP δ^{18}O; however, the equivalent for Dye3 shows a worse comparison, especially in the glacial (Figure A.1). This implies that the northern ice cores are uninformative for southern Greenland climate and/or the prior covariance structure does not properly convey information from northern ice cores to southern Greenland. The former demonstrates a need for data in southern Greenland, while the latter suggests a need for more climate-model simulations.

To evaluate whether each ice core is informative for southern Greenland climate, we compute the difference in evaluation metrics – correlation coefficient (Δ r), coefficient of efficiency (Δ CE), and root mean squared error (Δ RMSE) – between two sets of iterations when evaluated against Dye3, the only southern Greenland ice-core record. These two sets of iterations are: 1) ten iterations that exclude one proxy record, and 2) ten iterations that include all proxy records. We subtract the latter (all records) from the former (excluding one record), such that if the excluded proxy record is informative of southern Greenland climate,

then the difference will be negative for r and CE and positive for RMSE.

To test the extent to which information from each core is spread to southern Greenland, we compute the change in ensemble variance (Δ variance) in southern Greenland for each set of iterations and average over time. To compute Δ variance, we divide by the iterations that include all proxy records, such that the result is fractional change in variance with a larger values indicating that more information is spread from the proxy record to southern Greenland. For this analysis, we focus on the change in variance for a region around Kangerlussuaq (65°N to 68.7°N and 48.5°W to 52.5°W), which does not overlap the location of Dye3.

We compute each "Δ" value as a mean over the Holocene to create a fair comparison between the proxy records that span different time periods; however, the implications of this analysis are insensitive to averaging over just the Holocene or the full 20,000 years.

Our reconstruction of southern Greenland temperature and precipitation generally improves with the inclusion of any of these ice-core records; however, it improves the most with the inclusion of the Dye3 records (Figure A.2). In addition, the Dye3 records result in the greatest change in ensemble variance in the Kangerlussuaq region (Figure A.2).

A.5 Improvement of the Reanalysis Over the Prior Ensemble and TraCE-21ka

In Section 2.3.2, we present an evaluation of our main reanalysis using independent proxies and based on four skill metrics, correlation coefficient (r), coefficient of efficiency (CE), root mean square error (RMSE), and ensemble calibration ratio (ECR). Each of these skill metrics is described in detail in Section 2.2.3. We evaluate over three time periods, the full overlap of the reanalysis and the proxy record, a late-glacial period (20-15 ka), and period in the Holocene (8-3 ka). The computed skill metrics for the posterior ensemble are shown in Figures 2.6 and 2.7. We compare these evaluation metrics to those of the prior ensemble (Figures A.6 and A.7) and TraCE-21ka (Figures A.8 and A.9). The skill metrics for TraCE-21ka are shown in Figures A.10 and A.11.

A.6 Methods for the O8, N3O5, and N3O5_BA Experiments

The O8 experiment method differs from that for the main temperature reanalysis in the following way: it assimilates all eight δ^{18}O proxy records with the first 100-member prior ensemble, which results in just one iteration and a 100-member reanalysis ensemble.

The N3O5 experiment is similar to the O8 experiment except that it assimilates the three δ^{15}N-derived temperature records from Buizert et al. (2014) in place of the δ^{18}O records at the GIPS2, NEEM, and NGRIP sites. The temperature records are for the period 20 to 10 ka. To compute anomalies, we subtract site temperatures from the Box (2013) temperature reconstruction averaged over the reference period, 1850-2000 CE. To assimilate the δ^{15}N-derived temperature records we apply a direct-comparison proxy system model (PSM) (as is done for the main precipitation reanalysis) between the record and the simulated temperature at the model grid-cell closest to the ice-core site. For the δ^{15}N-derived temperature error variance, we use the reported variance values averaged across all time steps from the Buizert et al. (2014) supplementary information table. This gives error variance values of 6.35, 5.41, and 6.56 $^{\circ}C^2$ for the GISP2, NEEM, and NGRIP, records respectively.

The N3O5_BA experiment differs from the N3O5 experiment with respect to the prior ensemble. For the N3O5_BA experiment, we use a 100-member prior ensemble of 10-year averages (as opposed to 50-year averages) that is selected from the 1,000 years that surround the Bølling-Allerød warming (14.6 ka). This time period was selected to have a covariance pattern that shows greater variability at lower latitudes in Greenland, a pattern that is inferred from the δ^{15}N-derived temperature records (Guillevic et al., 2013; Buizert et al., 2014).

Figures A.12 and A.13 show results from these three experiments for the warming out of the Younger Dryas and the warming into the Bølling-Allerød, respectively. The reconstructed climate-change patterns for these two events are nearly identical, but we show them both for completeness. The conclusions from these two events are qualitatively the same as those discussed in the main paper for the cooling into the Younger Dryas (Section 2.4.2 Figure

2.12).

A comparison of results from our main reanalysis and Buizert et al. (2014) at each ice-core site can be found in Table A.5 for each of the three abrupt temperature events.

A.7 Figures

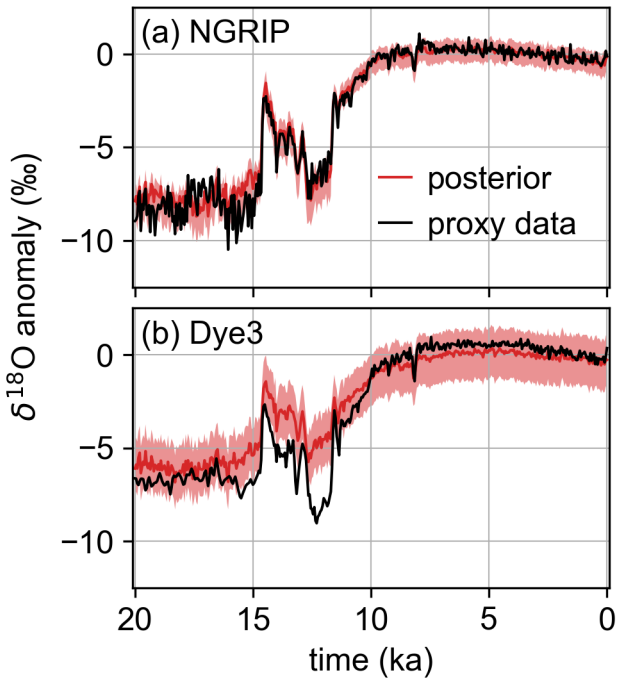

Figure A.1: Comparison of the posterior (red) ensemble mean and 5^{th} to 95^{th} percentile shading to excluded proxy records (black) for (a) the NGRIP δ^{18}O record and (b) the Dye3 δ^{18}O record. We find that the proxy network is able to better capture northern-central proxy records like NGRIP than the southern Greenland record, Dye3, especially in the glacial period.

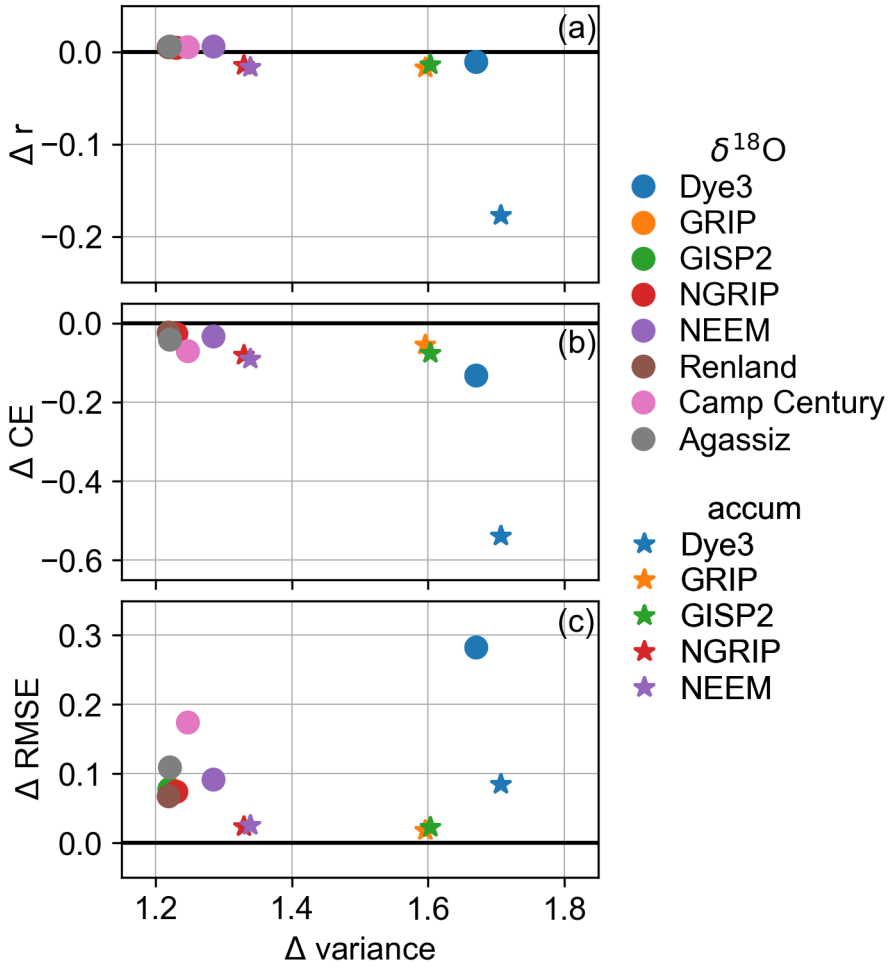

Figure A.2: Relative importance of each ice-core record for reconstructing southern Greenland climate. On the absicissa is the change in posterior ensemble variance (Δ variance) in the Kangerlussuaq region, which indicates how much information is spread from a proxy record to that region. Higher values indicate more information has reached the region. On the ordinates are changes to skill metrics at the Dye3 ice-core site, which indicate whether proxy records are valuable for reconstructing southern Greenland climate. (a) shows results for the correlation coefficient (r), (b) shows results for the coefficient of efficiency (CE), and (c) shows results for the root mean square error (RMSE). Negative values of r and CE and positive values of RMSE indicate that the proxy record improves the reconstruction at the Dye3 site. The proxy record under consideration is indicated by colors (for the site) and symbols (for the proxy variable). Note that Δ RMSE values are in units of ‰ for δ^{18}O and are unitless for accumulation.

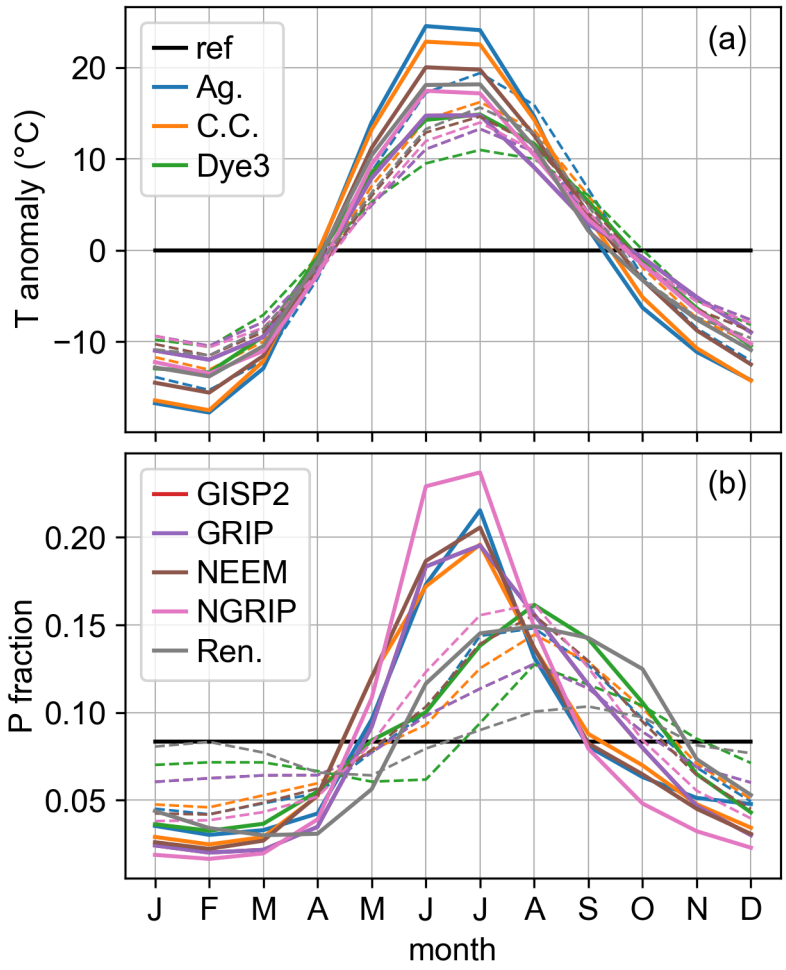

Figure A.3: A comparison of TraCE-21ka glacial and Holocene seasonality at each ice-core site considered in this study. The mean glacial (20 to 15 ka) seasonality is shown as solid lines and the mean Holocene (5 to 0 ka) seasonality is shown as dashed lines. Panel (a) shows the monthly temperature anomaly referenced to the annual mean. Panel (b) shows the fraction of total annual temperature that fell each month. For both panels, the reference line (black) shows no seasonal cycle. Both the magnitude and the timing of the seasonal cycle change between the glacial and the Holocene, with the glacial generally showing a stronger seasonal cycle and an earlier summer peak. ref = reference line, Ag. = Agassiz, C.C. = Camp Century, and Ren. = Renland.

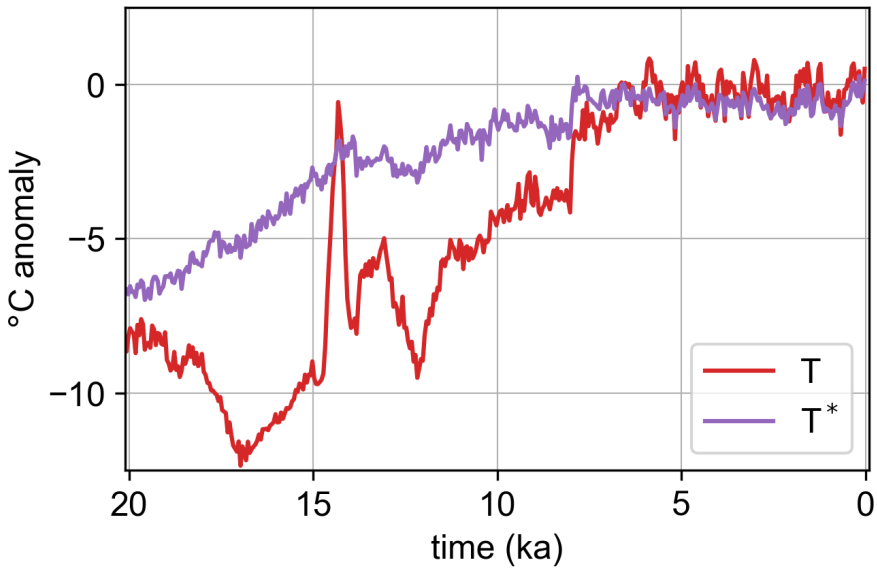

Figure A.4: Temperature (T) and temperature weighted by monthly precipitation (T*) from TraCE-21ka at Summit, Greenland. Both variables are shown as anomalies with respect to 1850-2000 CE and have been averaged to 50-year resolution. T* was computed before the anomaly was taken.

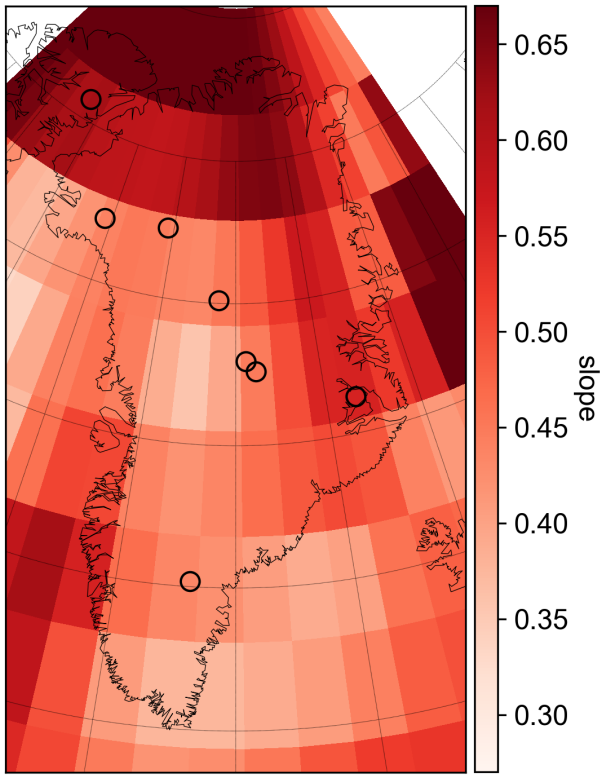

Figure A.5: Slope (°C ‰$^{-1}$) of the linear δ^{18}O-temperature relationship for each grid cell of the prior ensemble. The δ^{18}O-temperature relationship between grid cells is not shown. This is an example from one of the prior ensembles. For reference, open circles show the locations of ice-core records used in this study.

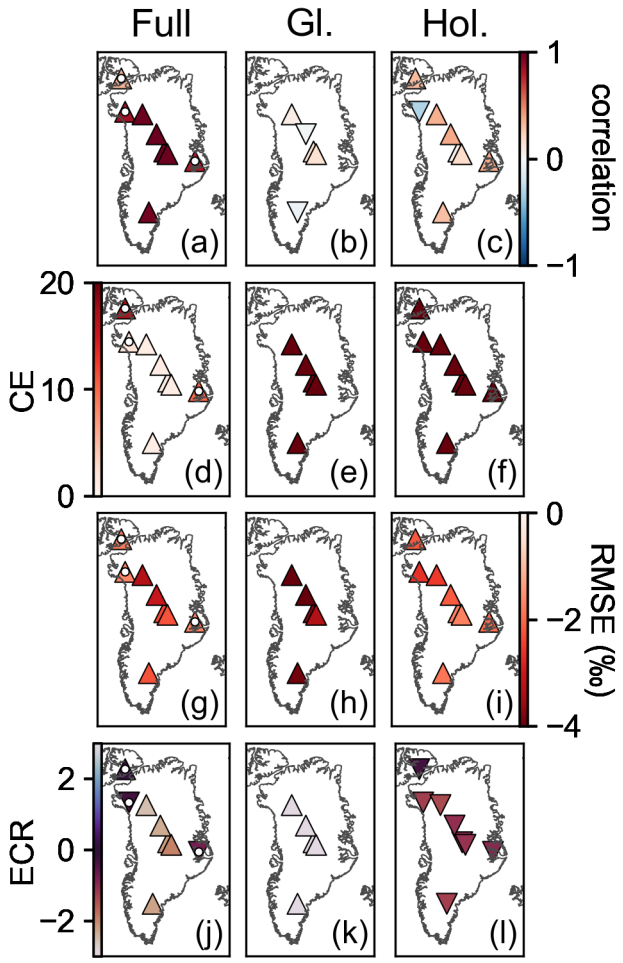

Figure A.6: Change in skill metrics from the prior to posterior ensemble averaged over iterations and time for the temperature reanalysis. The first column (panels (a), (d), (g), and (j)) shows the skill-metric change for the full overlap (Full) between the proxy record and reanalysis. A white dot indicates evaluation against proxy records that overlap only the Holocene (11.7-0 ka). The middle column (panels (b), (e), (h), and (k)) shows the skill-metric change for a period in the glacial (Gl.) (20-15 ka), while the right column (panels (c), (f), (i), and (l)) is for a period in the Holocene (Hol.) (8-3 ka). The first row (panels (a)-(c)) reports the change in correlation coefficient, the second row (panels (d)-(f)) the coefficient of efficiency (CE), the third (panels (g)-(i)) the root mean square error (RMSE), and the fourth row (panels (j)-(l)) the ensemble calibration ratio (ECR). Triangle symbols pointing up indicate that the posterior ensemble evaluates better than the prior ensemble for that location and statistic. Triangle symbols pointing down indicate the opposite. We define better evaluation as correlation coefficient closer to 1, CE closer to 1, RMSE closer to 0, and ECR closer to 1.

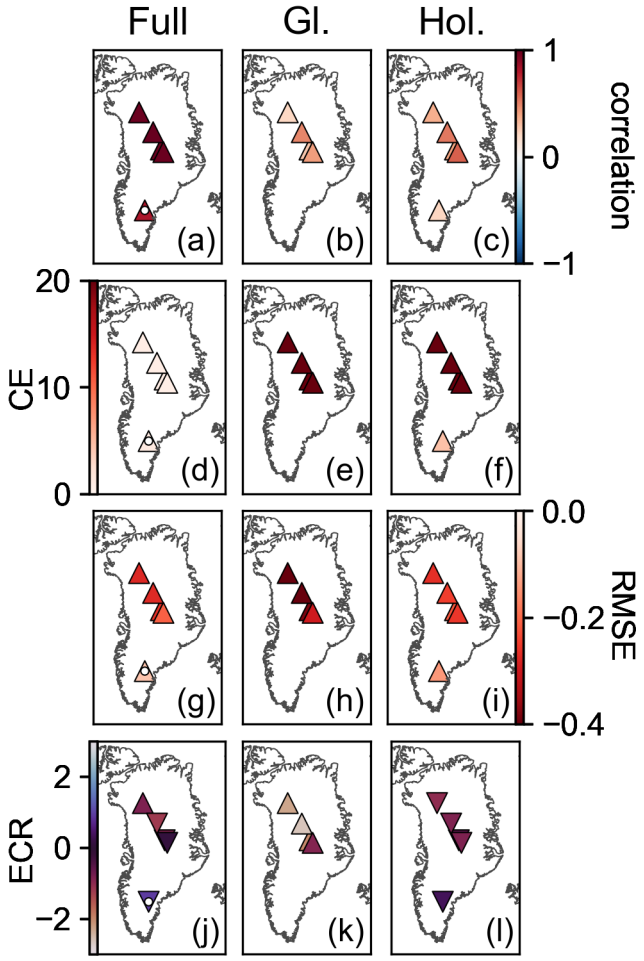

Figure A.7: Change in skill metrics from the prior to posterior ensemble averaged over iterations and time for the precipitation reanalysis. The first column (panels (a), (d), (g), and (j)) shows the skill-metric change for the full overlap (Full) between the proxy record and reanalysis. A white dot indicates evaluation against proxy records that overlap only the Holocene (11.7-0 ka). The middle column (panels (b), (e), (h), and (k)) shows the skill-metric change for a period in the glacial (Gl.) (20-15 ka), while the right column (panels (c), (f), (i), and (l)) is for a period in the Holocene (Hol.) (8-3 ka). The first row (panels (a)-(c)) reports the change in correlation coefficient, the second row (panels (d)-(f)) the coefficient of efficiency (CE), the third (panels (g)-(i)) the root mean square error (RMSE), and the fourth row (panels (j)-(l)) the ensemble calibration ratio (ECR). Triangle symbols pointing up indicate that the posterior ensemble evaluates better than the prior ensemble for that location and statistic. Triangle symbols pointing down indicate the opposite. We define better evaluation as correlation coefficient closer to 1, CE closer to 1, RMSE closer to 0, and ECR closer to 1.

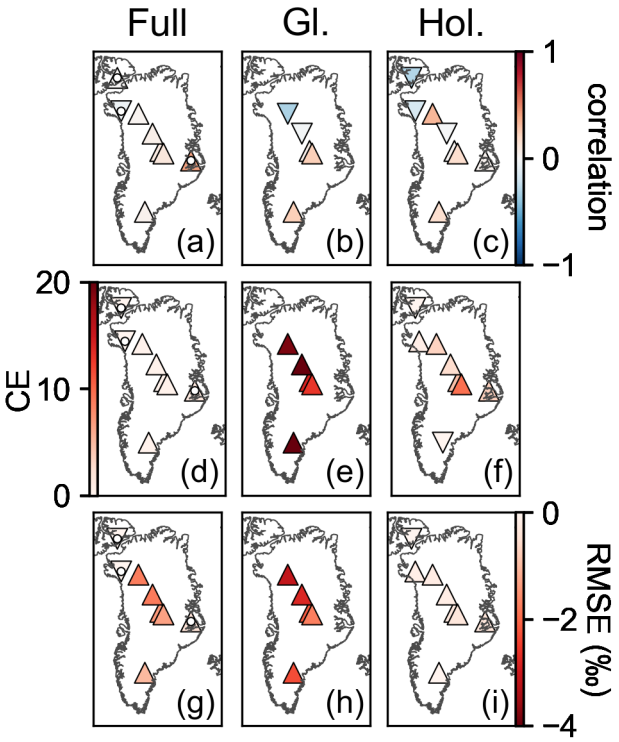

Figure A.8: Change in skill metrics from TraCE-21ka to posterior ensemble averaged over iterations and time for the temperature reanalysis. The first column (panels (a), (d), (g), and (j)) shows the skill-metric change for the full overlap (Full) between the proxy record and reanalysis. A white dot indicates evaluation against proxy records that overlap only the Holocene (11.7-0 ka). The middle column (panels (b), (e), (h), and (k)) shows the skill-metric change for a period in the glacial (Gl.) (20-15 ka), while the right column (panels (c), (f), (i), and (l)) is for a period in the Holocene (Hol.) (8-3 ka). The first row (panels (a)-(c)) reports the change in correlation coefficient, the second row (panels (d)-(f)) the coefficient of efficiency (CE), the third (panels (g)-(i)) the root mean square error (RMSE), and the fourth row (panels (j)-(l)) the ensemble calibration ratio (ECR). Triangle symbols pointing up indicate that the posterior ensemble evaluates better than the prior ensemble for that location and statistic. Triangle symbols pointing down indicate the opposite. We define better evaluation as correlation coefficient closer to 1, CE closer to 1, RMSE closer to 0, and ECR closer to 1.

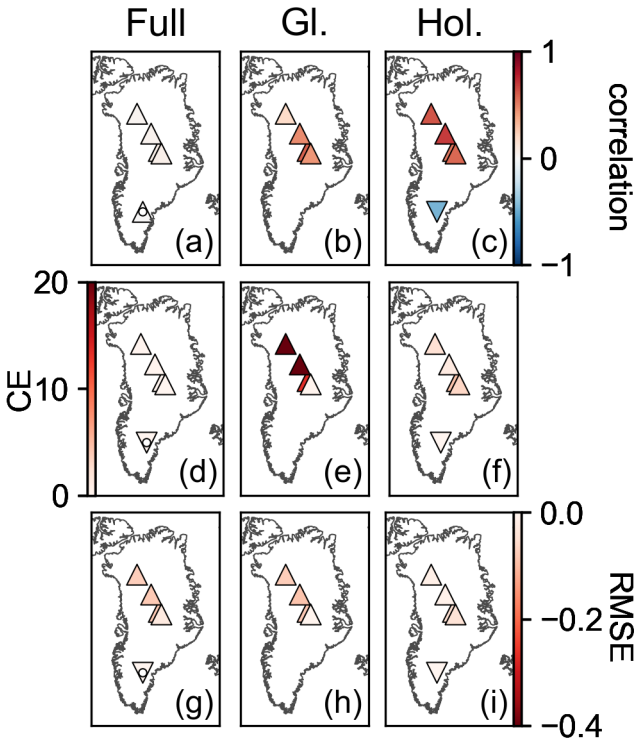

Figure A.9: Change in skill metrics from TraCE-21ka to posterior ensemble averaged over iterations and time for the precipitation reanalysis. The first column (panels (a), (d), (g), and (j)) shows the skill-metric change for the full overlap (Full) between the proxy record and reanalysis. A white dot indicates evaluation against proxy records that overlap only the Holocene (11.7-0 ka). The middle column (panels (b), (e), (h), and (k)) shows the skill-metric change for a period in the glacial (Gl.) (20-15 ka), while the right column (panels (c), (f), (i), and (l)) is for a period in the Holocene (Hol.) (8-3 ka). The first row (panels (a)-(c)) reports the change in correlation coefficient, the second row (panels (d)-(f)) the coefficient of efficiency (CE), the third (panels (g)-(i)) the root mean square error (RMSE), and the fourth row (panels (j)-(l)) the ensemble calibration ratio (ECR). Triangle symbols pointing up indicate that the posterior ensemble evaluates better than the prior ensemble for that location and statistic. Triangle symbols pointing down indicate the opposite. We define better evaluation as correlation coefficient closer to 1, CE closer to 1, RMSE closer to 0, and ECR closer to 1.

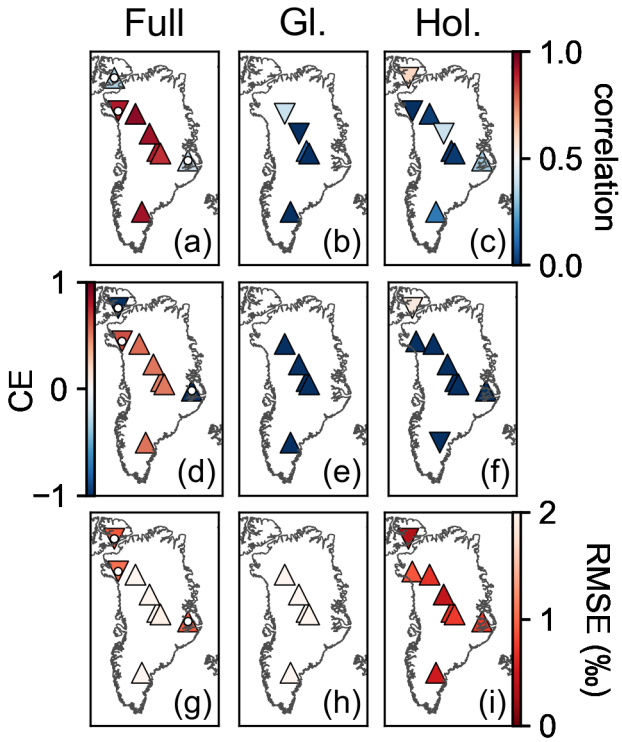

Figure A.10: Temperature skill metrics for the TraCE-21ka simulation. The first column (panels (a), (d), (g), and (j)) shows the skill metrics for the full overlap (Full) between the proxy record and TraCE-21ka. A white dot indicates evaluation against proxy records that overlap only the Holocene (11.7-0 ka). The middle column (panels (b), (e), (h), and (k)) shows the skill metrics for a period in the glacial (Gl.) (20-15 ka), while the right column (panels (c), (f), (i), and (l)) is for a period in the Holocene (Hol.) (8-3 ka). The first row (panels (a)-(c)) reports the correlation coefficient, the second row (panels (d)-(f)) the coefficient of efficiency (CE), the third (panels (g)-(i)) the root mean square error (RMSE), and the fourth row (panels (j)-(l)) the ensemble calibration ratio (ECR). Triangle symbols pointing up indicate that the posterior ensemble of our main reanalysis evaluates better than TraCE-21ka for that location and statistic. Triangle symbols pointing down indicate the opposite. We define better evaluation as correlation coefficient closer to 1, CE closer to 1, RMSE closer to 0, and ECR closer to 1.

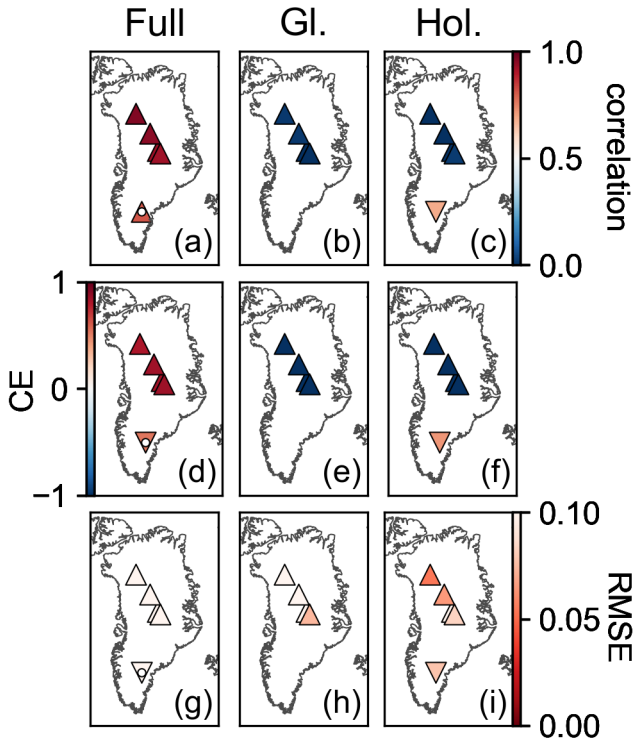

Figure A.11: Precipitation skill metrics for the TraCE-21ka simulation. The first column (panels (a), (d), (g), and (j)) shows the skill metrics for the full overlap (Full) between the proxy record and TraCE-21ka. A white dot indicates evaluation against proxy records that overlap only the Holocene (11.7-0 ka). The middle column (panels (b), (e), (h), and (k)) shows the skill metrics for a period in the glacial (Gl.) (20-15 ka), while the right column (panels (c), (f), (i), and (l)) is for a period in the Holocene (Hol.) (8-3 ka). The first row (panels (a)-(c)) reports the correlation coefficient, the second row (panels (d)-(f)) the coefficient of efficiency (CE), the third (panels (g)-(i)) the root mean square error (RMSE), and the fourth row (panels (j)-(l)) the ensemble calibration ratio (ECR). Triangle symbols pointing up indicate that the posterior ensemble of our main reanalysis evaluates better than TraCE-21ka for that location and statistic. Triangle symbols pointing down indicate the opposite. We define better evaluation as correlation coefficient closer to 1, CE closer to 1, RMSE closer to 0, and ECR closer to 1.

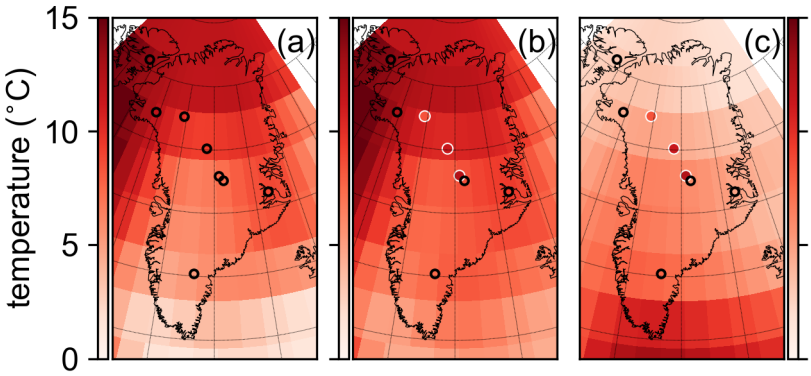

Figure A.12: Spatial pattern of the abrupt warming event out of the Younger Dryas. Panel (a) shows results from experiment O8, assimilating all eight δ^{18}O records, panel (b) shows results from experiment N3O5, assimilating all three δ^{15}N-derived temperature records and the remaining five δ^{18}O records (those that do not overlap with the δ^{15}N sites), and panel (c) shows results from experiment N3O5_BA, which is similar to the N3O5 experiment except the prior ensemble is selected from the 1,000 years surrounding the Bølling-Allerød warming. Unfilled black circles show locations of assimilated δ^{18}O records, while filled circles with white outlines show locations of assimilated δ^{15}N-derived temperature records. Filled circles in panels (b) and (c) show the δ^{15}N-derived temperature values as reported by Buizert et al. (2014) on the same color scale as the rest of the panel. The temporal definition of this event is the same as defined in Buizert et al. (2014).

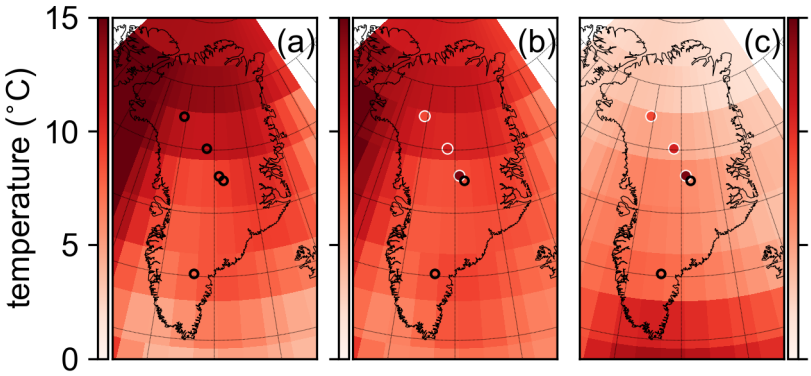

Figure A.13: Spatial pattern of the abrupt warming event into the Bølling-Allerød. Panel (a) shows results from experiment O8, assimilating all eight δ^{18}O records, panel (b) shows results from experiment N3O5, assimilating all three δ^{15}N-derived temperature records and the remaining five δ^{18}O records (those that do not overlap with the δ^{15}N sites), and panel (c) shows results from experiment N3O5_BA, which is similar to the N3O5 experiment except the prior ensemble is selected from the 1,000 years surrounding the Bølling-Allerød warming. Unfilled black circles show locations of assimilated δ^{18}O records, while filled circles with white outlines show locations of assimilated δ^{15}N-derived temperature records. Filled circles in panels (b) and (c) show the δ^{15}N-derived temperature values as reported by Buizert et al. (2014) on the same color scale as the rest of the panel. The temporal definition of this event is the same as defined in Buizert et al. (2014).

A.8 Tables

Table A.1: The mean slope for the linear δ^{18}O-temperature relationship used for the main reconstruction in this study (black, "main") and the mean slope for the relationship used in the S4 sensitivity experiment in this study (red, "S4"). We also include estimates from previous work, inlcuding, slopes found by Buizert et al. (2014) (purple, "B14") as seen in their Figure 3 for five discontinuous time periods between 20 and 10 ka; slopes found by Guillevic et al. (2013) (green, "G13") from their Table 3 for Dansgaard-Oeschger events 8, 9, and 10; slopes found by Kindler et al. (2014) (blue, "K14") from their Figure 5 and estimated from their Figure 6 for 120 to 10 ka; and slopes found by Cuffey and Clow (1997) (orange, "C97") for time periods between 50 and 0.5 ka. The cores are arraged from North (top) to South (bottom).

Core Name	**Slope Range (°C ‰$^{-1}$)**	**Slope Average (°C ‰$^{-1}$)**
Agassiz	main: 0.618 - 0.656	0.640
	S4: 0.412 - 0.437	0.425
Camp Century	main: 0.439 - 0.468	0.456
	S4: 0.293 - 0.312	0.304
NEEM	main: 0.450 - 0.480	0.465
	S4: 0.300 - 0.320	0.310
	B14: 0.25 - 0.76	0.50
	G13: 0.51 - 0.63	0.57
NGRIP	main: 0.454 - 0.489	0.470
	S4: 0.303 - 0.326	0.313
	B14: 0.29 - 0.41	0.36
	G13: 0.34 - 0.47	0.42
	K14: 0.3 - 0.57	0.52
GISP2	main: 0.442 - 0.493	0.467
	S4: 0.294 - 0.329	0.311
	B14: 0.11 - 0.30	0.25
	G13: 0.38	
	C97: 0.251 - 0.465	0.324
GRIP	main: 0.442 - 0.493	0.467
	S4: 0.294 - 0.329	0.311
	G13: 0.49	
Renland	main: 0.546 - 0.595	0.571
	S4: 0.364 - 0.397	0.381
Dye3	main: 0.424 - 0.475	0.444
	S4: 0.283 - 0.317	0.296

Table A.2: Comparison of abrupt climate transitions in our main reconstruction and sensitivity reconstructions, S1, S2, S3, and S4 for the Agassiz, Camp Century, NEEM, and NGRIP cores. We use the same time definitions as in Buizert et al. (2014). Note that the main reconstruction and S4 do not warm as rapidly out of the Younger Dryas as S1, S2, and S3. Thus, our use of a single time definition may not allow us capture the full transition for all of these reconstructions. BA = Bølling-Allerød and YD = Younger Dryas.

Core Name	**Reconstruction Name**	**BA warming (°C)**	**YD cooling (°C)**	**YD warming (°C)**
Agassiz	Main (δ^{18}O= $0.67T^*$)	12.83	-9.10	11.64
	S1 (δ^{18}O= $0.67T$)	8.67	-5.16	7.78
	S2 (δ^{18}O= $0.5T$)	11.20	-6.96	10.50
	S3 (δ^{18}O= $0.335T$)	15.41	-9.99	14.84
	S4 (δ^{18}O= $0.67T^*$, stronger P seasonality)	15.49	-11.05	13.06
Camp Century	Main	11.71	-8.51	10.53
	S1	8.04	-4.94	7.13
	S2	10.40	-6.60	9.65
	S3	14.34	-9.41	13.71
	S4	14.07	-10.36	11.46
NEEM	Main	10.17	-7.53	9.10
	S1	7.11	-4.51	6.34
	S2	9.22	-5.99	8.33
	S3	12.74	-8.47	12.16
	S4	12.18	-9.20	9.71
NGRIP	Main	9.62	-7.17	8.57
	S1	6.76	-4.33	6.03
	S2	8.77	-5.73	8.14
	S3	12.13	-8.09	11.57
	S4	11.52	-8.77	9.07

Table A.3: Same as A.2, but for the GISP2, GRIP, Renland, and Dye3 cores.

Core Name	**Reconstruction Name**	**BA warming (°C)**	**YD cooling (°C)**	**YD warming (°C)**
GISP2	Main	7.78	-6.03	6.88
	S1	5.66	-3.88	5.18
	S2	7.39	-5.06	6.92
	S3	10.26	-7.03	9.81
	S4	9.27	-7.41	7.03
GRIP	Main	7.78	-6.03	6.88
	S1	5.66	-3.88	5.18
	S2	7.39	-5.06	6.92
	S3	10.26	-7.03	9.81
	S4	9.27	-7.41	7.03
Renland	Main	8.51	-6.27	7.77
	S1	5.93	-3.78	5.39
	S2	7.70	-5.02	7.22
	S3	10.64	-7.08	10.22
	S4	10.15	-7.62	8.53
Dye3	Main	6.45	-5.64	5.41
	S1	5.33	-4.34	5.26
	S2	7.05	-5.45	6.84
	S3	9.92	-7.29	9.60
	S4	7.62	-7.10	4.79

Table A.4: Scaling factors (β) for the temperature-precipitation relationship in the Kangerlussuaq region. The results for the main reanalysis are in bold.

Temperature scenario	**Precipitation scenario**	**No Filtering**	**Low-Pass (5,000 years^{-1})**	**High-Pass (5,000 years^{-1})**
Main	Low	0.09	0.09	0.04
Main	**Moderate**	**0.08**	**0.08**	**0.04**
Main	High	0.08	0.08	0.05
S1	Low	0.12	0.11	0.05
S1	Moderate	0.11	0.11	0.06
S1	High	0.11	0.11	0.07
S2	Low	0.09	0.09	0.04
S2	Moderate	0.09	0.08	0.04
S2	High	0.09	0.08	0.05
S3	Low	0.06	0.06	0.03
S3	Moderate	0.06	0.06	0.03
S3	High	0.06	0.06	0.04
S4	Low	0.07	0.07	0.03
S4	Moderate	0.07	0.07	0.03
S4	High	0.07	0.07	0.04

Table A.5: Comparison of abrupt climate transitions in our main reconstruction (black) and from Buizert et al. (2014) (purple values in the second row for NEEM, NGRIP, and GISP2). Uncertainties are given as standard deviations. We use the published values and uncertainties from Buizert et al. (2014). We use the same time definitions as in Buizert et al. (2014).

Core Name	**Bølling-Allerød warming**	**Younger Dryas cooling**	**Younger Dryas warming**
Agassiz	12.83 ± 3.49	-9.10 ± 3.65	11.64 ± 3.46
Camp Century	11.71 ± 3.23	-8.51 ± 3.42	10.53 ± 3.24
NEEM	10.17 ± 3.01 8.9 ± 1.2	-7.53 ± 3.2 -4.8 ± 0.6	9.10 ± 3.05 8.4 ± 1.5
NGRIP	9.62 ± 2.90 10.8 ± 1.0	-7.17 ± 3.09 -10.9 ± 1.0	8.57 ± 2.95 11.4 ± 1.6
GISP2	7.78 ± 2.77 14.4 ± 0.95	-6.03 ± 2.96 -9.2 ± 0.45	6.88 ± 2.84 12.4 ± 1.7
GRIP	7.78 ± 2.77	-6.03 ± 2.96	6.88 ± 2.84
Renland	8.51 ± 2.55	-6.27 ± 2.70	7.77 ± 2.57
Dye3	6.45 ± 3.84	-5.64 ± 4.10	5.41 ± 3.96

Appendix B

SUPPLEMENTARY INFORMATION FOR "UNCERTAINTY IN RECONSTRUCTING PALEO-ELEVATION OF THE ANTARCTIC ICE SHEET FROM TEMPERATURE-SENSITIVE ICE CORE RECORDS"

B.1 Introduction

In this supporting information, we expand on the assumptions behind the dry and moist temperature decompoisitions. To do this, we start with a more detailed derivation of the equations. Then we discuss the assumptions that ultimately explain much of the residual that results from applying these decompositions to climate simulations.

B.2 Derivation of Temperature Decompositions

The following is an expanded derivation of the dry and moist temperature decompositions.

From the first law of thermodynamics, the internal energy of an air parcel is given by:

$$du = d\omega - dq \tag{B.1}$$

where u is the internal energy, ω is the work done, and q is the added heat.

Following Wallace and Hobbs (2006), $dw = -\alpha dp$ and $du = c_p dT$, where α is specific volume, p is pressure, c_p is heat capacity at constant pressure, and T is temperature. Assuming hydrostatic balance ($-\alpha dp = gdz$), equation B.1 can be written as:

$$dq = c_p dT + gdz \tag{B.2}$$

where g is acceleration due to gravity and z is the elevation above a reference height, such as modern sea level. Assuming that heat is added or removed from the air parcel via a

reversible process, dq can be written as:

$$dq = c_p T \frac{d\theta}{\theta} \tag{B.3}$$

where θ is the potential temperature:

$$\theta = T \frac{p_0}{p}^{R_d/c_p} \tag{B.4}$$

and where R_d is the gas constant of dry air and p_0 is a reference pressure, usually 1000 hPa. Equation B.3 ignores the influence of latent heating, a topic which we return to shortly.

Combining equations B.2 and B.3 and rearranging results in:

$$dT = -\Gamma_d dz + \frac{T}{\theta} d\theta \tag{B.5}$$

Returning to the topic of water vapor, internal latent heating can be included with an additional term in equation B.3:

$$dq = c_p T \frac{d\theta}{\theta} - L_v dw_s \tag{B.6}$$

where L_v is the latent heat of vaporization and w_s is the saturation mixing ratio:

$$w_s = \frac{100q}{\mathrm{RH}(1-q)} \tag{B.7}$$

and where q is the specific humidity and RH is the relative humidity. This way of including latent heating requires the assumption that any condensation remains in the air parcel.

Combining equations B.6 and B.2 and following Randall (2009) gives,

$$dT = -\Gamma_m dz + \left[1 + \frac{L_v w_s}{R_d T}\right]^{-1} \frac{\Gamma_s}{\Gamma_d} \frac{T}{\theta} d\theta \tag{B.8}$$

where Γ_m is the moist adiabatic lapse rate:

$$\Gamma_m = \Gamma_d \frac{1 + \frac{L_v w_s}{R_d T}}{1 + \frac{\epsilon L_v^2 w_s}{c_p R_d T^2}} \tag{B.9}$$

and where ϵ is the ratio of the gas constant for water vapor to the gas constant for dry air.

B.3 Extended Discussion of Decomposition Residual

Here we extend the discussion of the residual that arises when applying the temperature decompositions to the ensemble of model simulations.

Though there are likely other contributors to the residual, the main source arises from the fact that the paleoaltimetry application of the first law of thermodynamics is not quite Lagrangian nor Eularian, as described in section 2 of the paper. This causes a reduced accuracy of the hydrostatic approximation when applied to paleoclimate timescales. The temperature decompositions (equations 3.2 and B.8) invoke the hydrostatic approximation, $-\alpha dp = gdz$, where α is the specific volume and p is pressure. This relationship applies to an atmosphere in hydrostatic equilibrium, an appropriate assumption for each individual climate simulation. The issue arises when applying the hydrostatic equation to two different atmospheric equilibriums (in this case, the LGM and PI).

When raising or lowering an air parcel in a hydrostatic atmosphere,

$$\frac{dp}{dz} = -g/\alpha \tag{B.10}$$

For paleoaltimetry applications, equation B.10 is assumed to expand as follows:

$$\frac{p_{\mathrm{PI}_{\mathrm{surf}}} - p_{\mathrm{LGM}_{\mathrm{surf}}}}{z_{\mathrm{PI}}(p_{\mathrm{PI}_{\mathrm{surf}}}) - z_{\mathrm{LGM}}(p_{\mathrm{LGM}_{\mathrm{surf}}})} = -g/\alpha_{\mathrm{LGM}} \tag{B.11}$$

Each pressure refers to either the pressure at the PI ice sheet surface during the PI simulation ($p_{\mathrm{PI}_{\mathrm{surf}}}$) or the pressure of the LGM ice sheet surface during the LGM simulation ($p_{\mathrm{LGM}_{\mathrm{surf}}}$). The subscripts on z indicate which pressure-elevation equilibrium is being referenced, which is necessary because the equilibriums may differ for the LGM and PI. Following our conventions from section 3.2 in the paper, α is taken from the LGM atmosphere. For equation B.11 to be true, the LGM-to-PI change in elevation and pressure must be consistent with the LGM pressure-elevation curve, such that:

$$z_{\mathrm{PI}}(p_{\mathrm{PI}_{\mathrm{surf}}}) = z_{\mathrm{LGM}}(p_{\mathrm{PI}_{\mathrm{surf}}}) \tag{B.12}$$

The equivalence in equation B.12 cannot be assessed in the climate simulations because they do not provide pressures below the surface of the LGM ice sheet. A similar equivalence, however, can be assessed at most locations in the simulations:

$$z_{\mathrm{LGM}}(p_{\mathrm{LGM_{surf}}}) = z_{\mathrm{PI}}(p_{\mathrm{LGM_{surf}}}) \tag{B.13}$$

For most locations in most of the simulations we look at, equation B.13 is false (Figure B.3). The impact of this faulty assumption on our decomposition can be estimated with equations B.13 and B.11. We find that, for most of the ensemble members, this assumption accounts for most or all of the residual (Figure B.4).

B.4 Figures

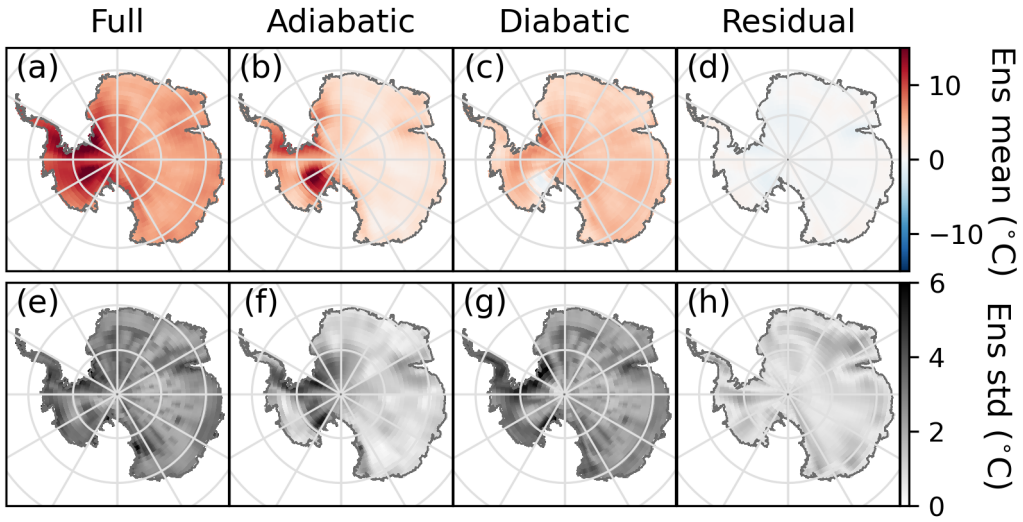

Figure B.1: Antarctic temperature decomposition as calculated with the moist adiabatic lapse rate (equation B.8). Panels (a)–(d) are ensemble means and panels (e)–(h) are standard deviations (std). Panels (a) and (e) show results for the full temperature change (PI minus LGM), panels (b) and (f) are for the adiabatic component, panels (c) and (g) are for the diabatic component, and panels (d) and (h) are for the residual.

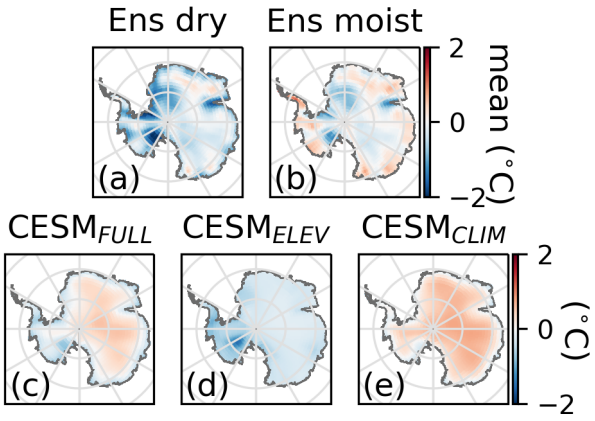

Figure B.2: Residual of the temperature decomposition. Panel (a) shows the ensemble mean residual for the dry temperature decomposition and panel (b) shows the same but for the moist temperature decomposition. Panels (c)–(e) are the residual for the dry temperature decomposition applied to $\text{CESM}_{\text{full}}$, $\text{CESM}_{\text{ELEV}}$, and $\text{CESM}_{\text{CLIM}}$, respectively. Panels (a) is the same as figure 2d, panel (b) is the same as Figure B.1d, and panels (c)–(e) are the same as figure 2l, p, and t, but with more appropriate color scales.

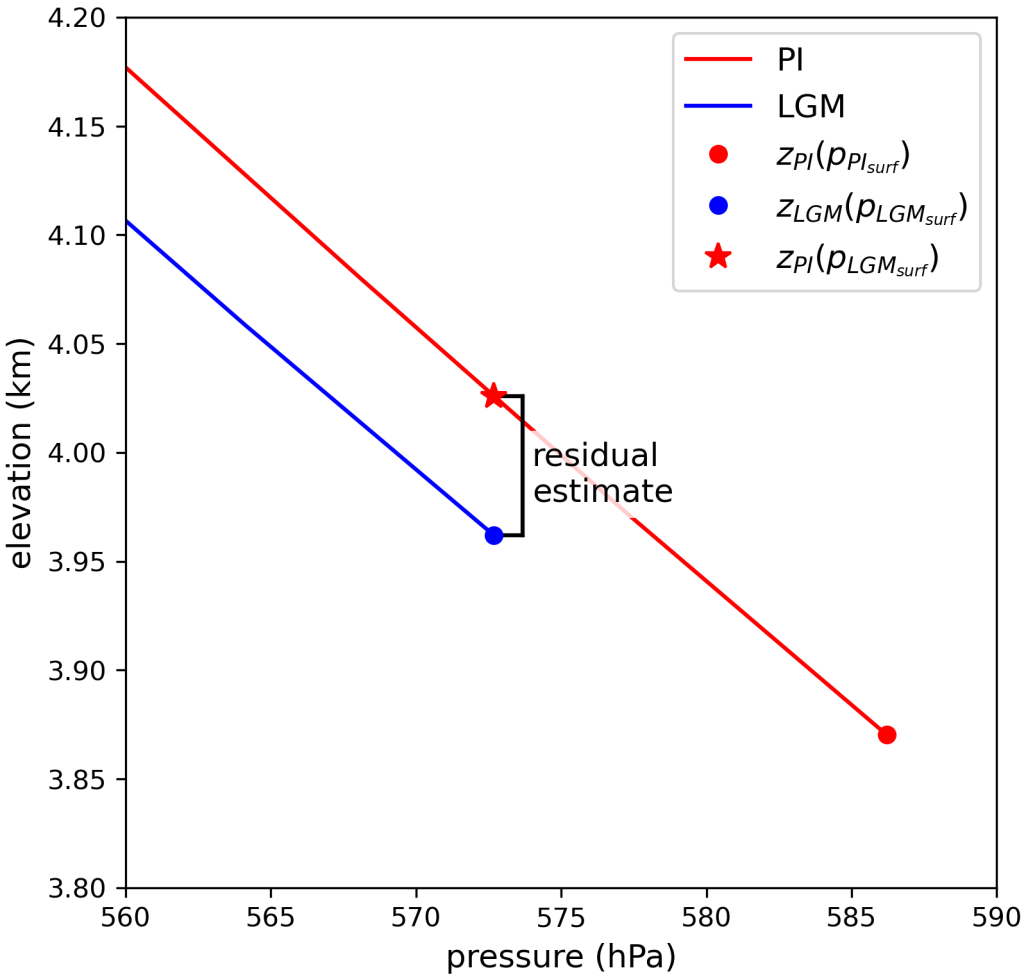

Figure B.3: Estimated residual resulting from assuming the same atmospheric pressure-elevation cureve in the Last Glacial Maximum (LGM) and the pre-Industrial (PI). The red curve shows the pre-Industrial pressure-elevation curve with the PI surface pressure and elevation shown by the red dot. The blue curve and dot are from the LGM. The red star shows the type of assumption we make when applying the hydrostatic approximation to changes between two very different atmospheric states. The residual can be well-estimated from this assumption for most of the models (Figure B.4).

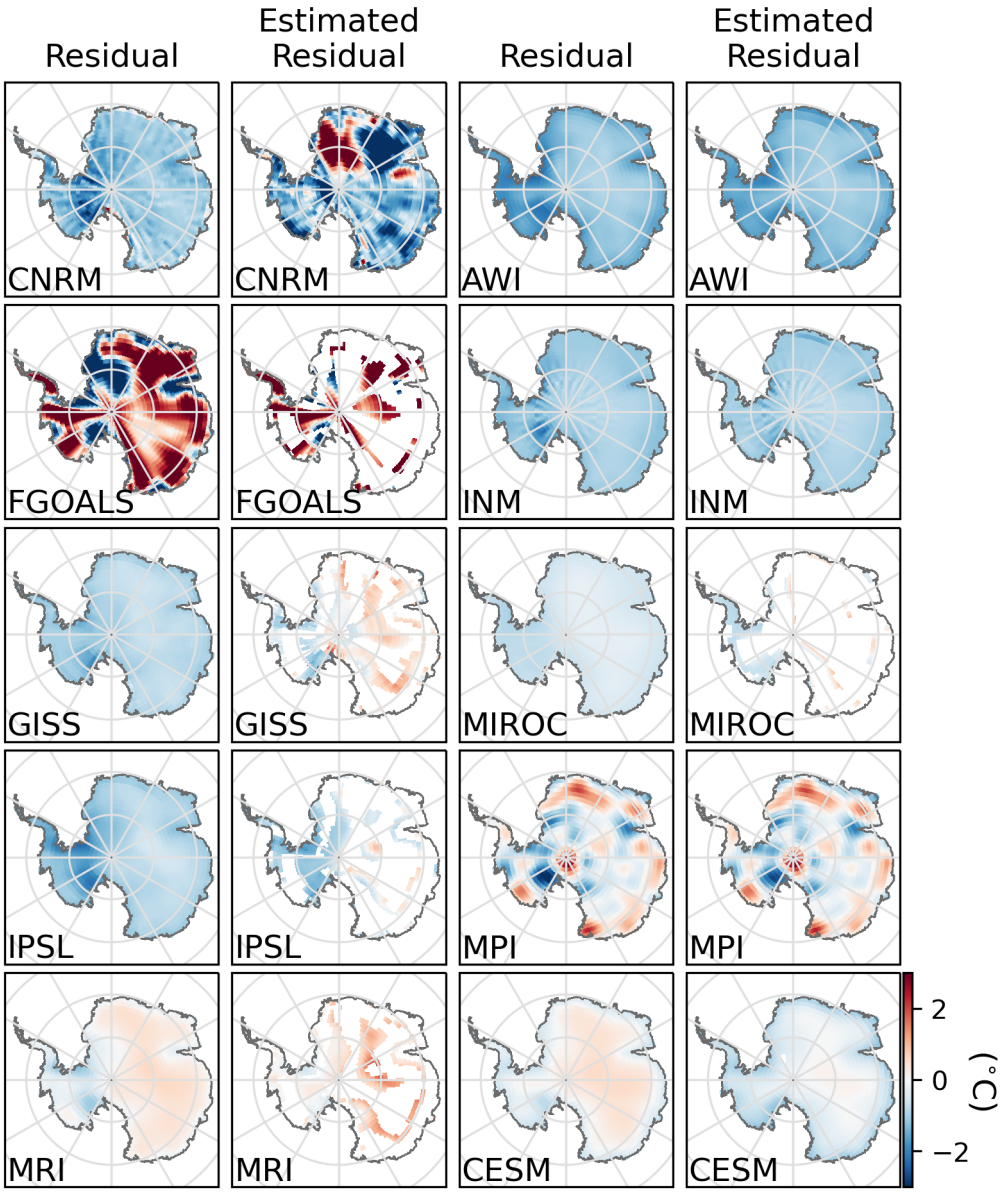

Figure B.4: Attribution of the residual resulting from application of the dry temperature decomposition to climate simulations. For each model in the ensemble, the residual is plotted along with an estimate of the residual. We find that the residual is related to the similarity of the atmospheric pressure-elevation curve between the Last Glacial Maximum and pre-Industrial periods.

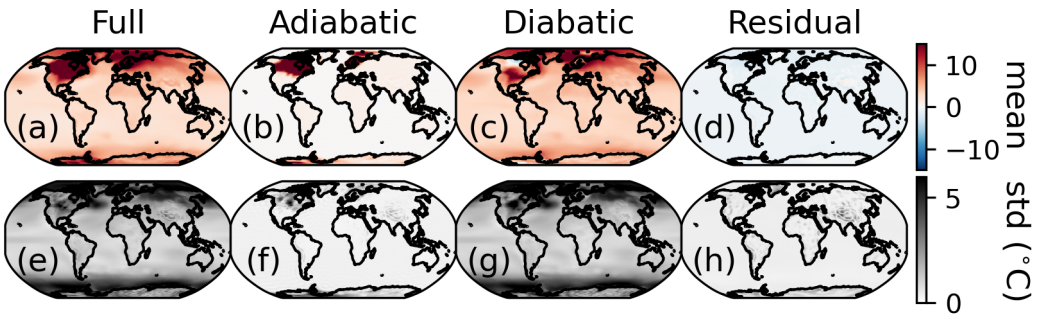

Figure B.5: Global temperature decomposition as calculated with the dry adiabatic lapse rate (equation 3.2). Panels (a)–(d) are ensemble means and panels (e)–(h) are standard deviations (std). Panels (a) and (e) show results for the full temperature change (PI minus LGM), panels (b) and (f) are for the adiabatic component, panels (c) and (g) are for the diabatic component, and panels (d) and (h) are for the residual. The residual is consistently small across the globe; however, outside of the polar regions, the residual is similar in magnitude to the adiabatic and diabatic terms. Thus, in low and mid-latitudes the residual is likely to have a proportionally greater influence on the error of relative elevation estimates.

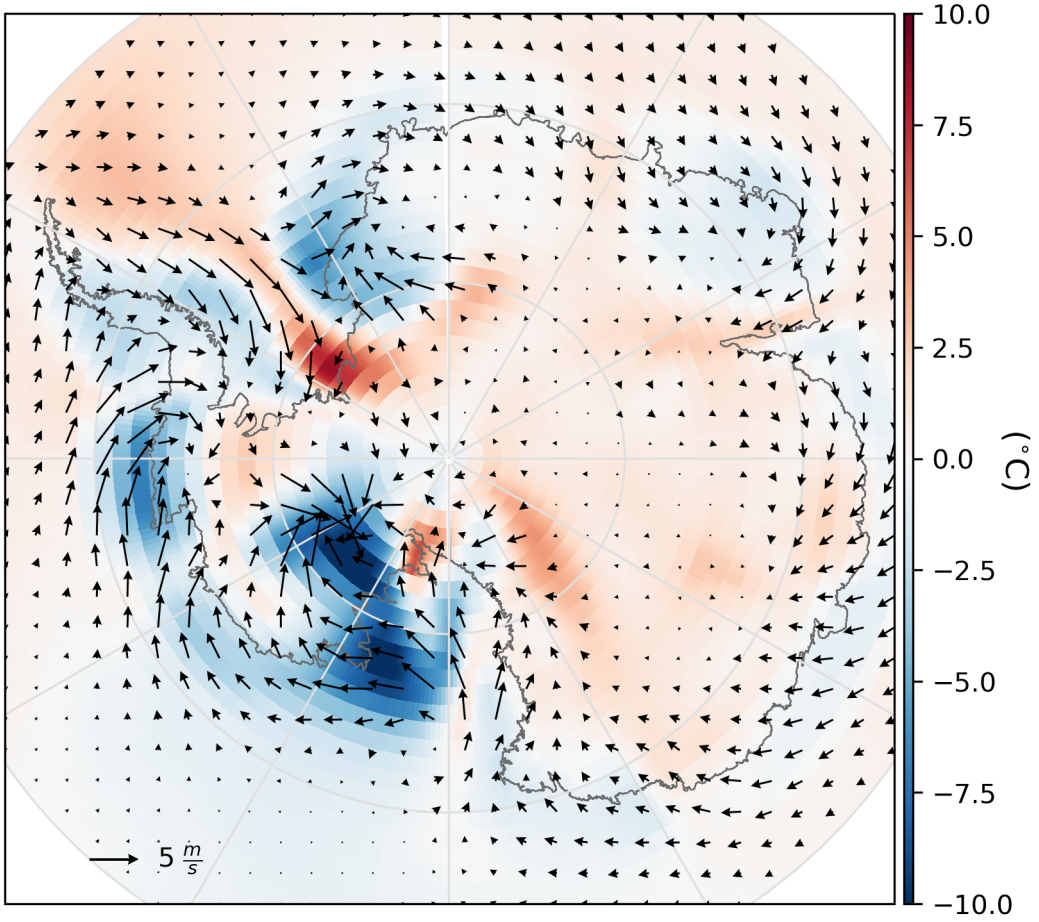

Figure B.6: Circulation changes caused by elevation change in the CESM ensemble member. Arrows indicate the direction and magnitude of the change in the lowest level winds from the CESM$_E$*LEV* simulation. Colors show the diabatic temperature change from the same simulation. The diabatic temperature change pattern is similar to the potential temperature change modeled by Steig et al. (2015) for a lowering of West Antarctica. Also similarly, the winds show an increase in cyclonic cirulation over West Antarctica. These wind and diabatic temperature changes are connected through conservation of poential vorticity as the air column is stretched (Steig et al., 2015).

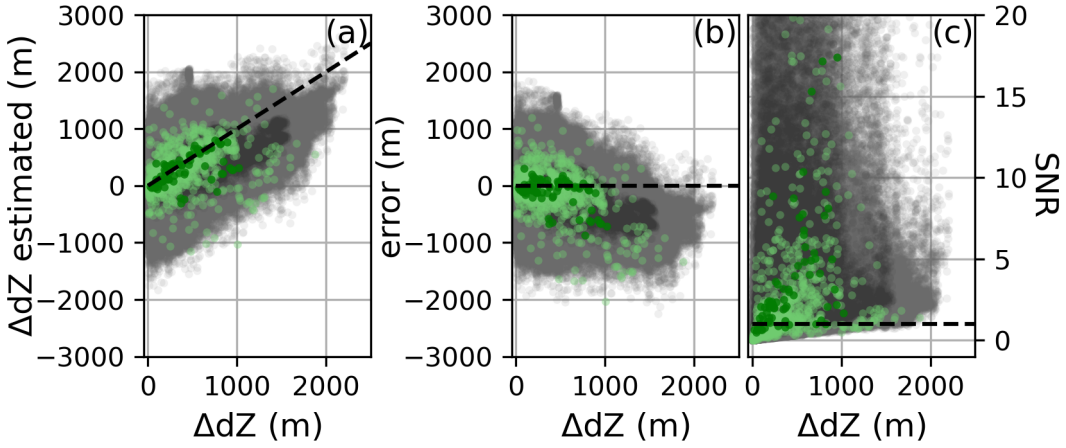

Figure B.7: Ensemble error in paleoaltimetry estimates of relative elevation change from the Last Glacial Maximum to pre-Industrial for Antarctica. Panel (a) shows how well the estimated relative elevation change ($\Delta dz_{\text{estimated}}$) compares to the model relative elevation change (Δdz) for all ice core pairs (green) and all additional location pairs (grey) for all 10 ensemble members. See figure 1 for a map of ice core and additional locations. The ensemble means are shown in darker shades of green and grey. The black dashed line is the 1:1 line. Panel (b) shows the error (equation 3.5) of the estimated relative elvation change. The dashed black line is at zero, no error. Panel (c) shows the signal-to-noise ratio (SNR) (equation 3.6). The dashed black line is at 1, which is where the magnitude of the signal (Δdz) equals the magnitude of the error. SNR values below the black dashed line have more error than signal, while the SNR values above the line have more signal than error.

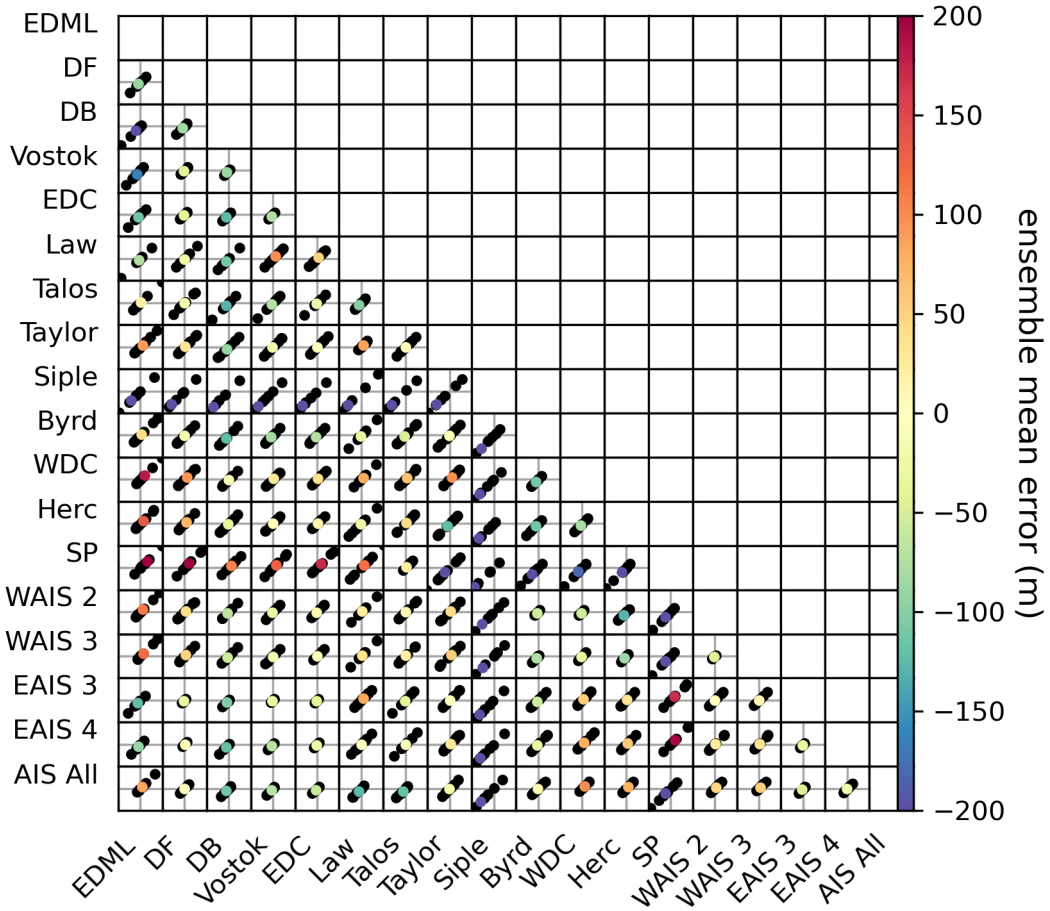

Figure B.8: Error in estimating relative elevation change (Δdz) from the Last Glacial Maximum to pre-Industrial for pairs of Antarctic ice cores and averages over cores (see table B.1 for long names). The black points show the individual ensemble members' error, while the colored points show the ensemble mean error. Each subplot has error plotted on both the x- and y-axes and each axis shows a range of -1000 to 1000 m. Positive errors indicate that the estimated Δdz is more positive or less negative than the model Δdz value. Subplots that show both a small spread in the ensemble members and a near-zero mean indicate that the models agree that this pairing of ice core sites is likely to yield a low-error estimate of relative elevation change. See Figure B.9 for a spatial representation of the ensemble mean error.

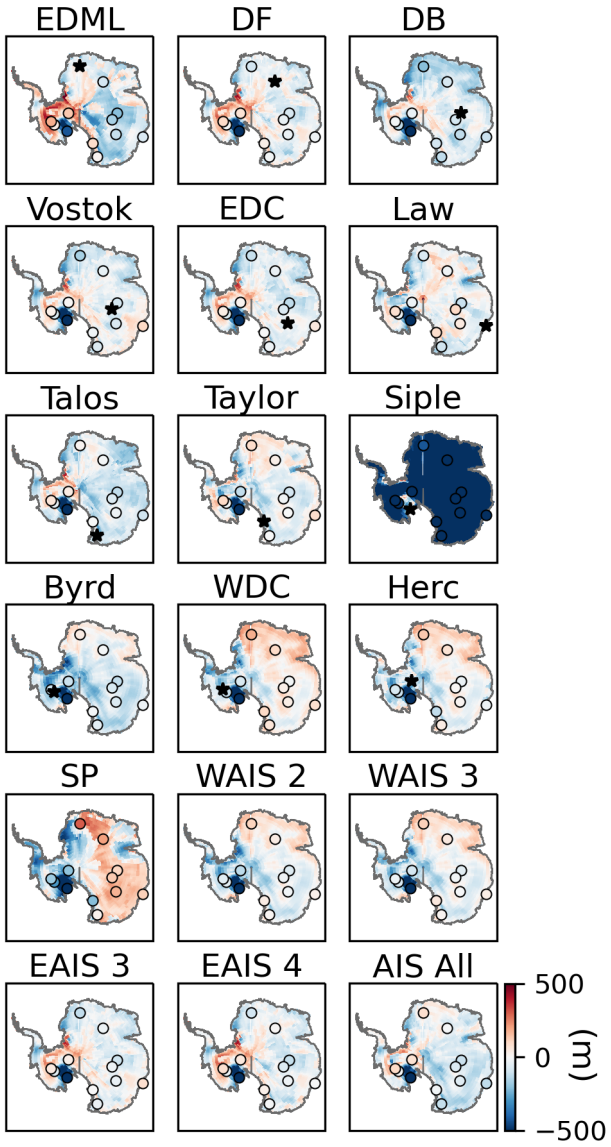

Figure B.9: Error resulting from estimating relative elevation change from the Last Glacial Maximum to the pre-Industrial in Antarctica. Each subplot shows errors for pairing each ice core and average over multiple ice cores – locations shown by black stars and names given in subplot titles (see table B.1 for long names) – with every other ice core and location around Antarctica. Black outlined circles show the locations of the other ice cores. Colors both inside and outside of the circles indicate the ensemble mean error that arises if that core or location is paired with the starred ice core or average.

B.5 Tables

Table B.1: Name and location information for each ice core and average over multiple cores. Latitudes and longitudes are reported in degrees South and East, respectively. Modern elevation is reported as meters above sea level.

Site Name	**Short Name**	**Lat (°S)**	**Lon (°E)**	**Modern Elev (m a.s.l.)**
EPICA Dronning Maud Land	EDML	75.00	0.07	2892
Dome F	DF	77.32	39.07	3810
Dome B	DB	77.08	94.92	3650
Vostok	Vostok	78.47	106.87	3488
EPICA Dome C	EDC	75.10	123.35	3233
Law Dome	Law	66.73	112.83	1390
Talos Dome	Talos	72.82	159.18	2315
Taylor Dome	Taylor	77.80	158.72	2365
Siple Dome	Siple	81.67	-148.82	621
Byrd	Byrd	80.02	-119.52	1530
WAIS Divide Core	WDC	79.46	-112.14	1766
Hercules Dome	Herc	86	-105	2600
South Pole	SP	90	0.0	2835
WDC, Byrd average	WAIS 2			
WDC, Byrd, Herc average	WAIS 3			
DF, EDC, Vostok average	EAIS 3			
DF, EDC, Vostok, EDML average	EAIS 4			
Average over all cores	AIS All			

Table B.2: Modeling centers, model names, short names used in this study, and associated project(s) for the climate simulations used in this study (Braconnot et al., 2011, 2012; Taylor et al., 2012; Eyring et al., 2016; Kageyama et al., 2017).

Model Name	**Short Name**	**Modeling Center**	**MIP**
CNRM-CM5	CNRM	CNRM-CERFACS	PMIP3, CMIP5
FGOALS-g2	FGOALS	LASG-CESS	PMIP3, CMIP5
GISS-E2-R	GISS	NASA-GISS	PMIP3, CMIP5
IPSL-CM5A-LR	IPSL	IPSL	PMIP3, CMIP5
MRI-CGCM3	MRI	MRI	PMIP3, CMIP5
AWI-ESM-1-1-LR	AWI	AWI	PMIP4, CMIP6
INM-CM4-8 INM	INM	INM	PMIP4, CMIP6
MIROC-ES2L	MIROC	MIROC	PMIP4, CMIP6
MPI-ESM1-2-LR	MPI	MIP-M	PMIP4, CMIP6
iCESM based on CESM1.2.0.1	CESM	NCAR	this study

VITA

Jessica Badgeley was grew up Seattle, Washington. In high school she participated in Girls on Ice (now Inspiring Girls Expedtions) in the North Cascades. There, she met her first science mentor, Erin Pettit, and decided to study glaciers.

Jessica attended Colorado College, where she majored in Geology, minored in Mathematics, and received her Bachelor's degree. While an undergraduate student, Jessica joined Erin Pettit for fieldwork in Antarctica to study Blood Falls using geophysical techniques. This became the subject of her undergraduate thesis and her first published paper. After graduating in 2015, Jessica was an assistant teacher for the Geographic Information Systems program at Colorado College.

In 2016, Jessica started her Ph.D. at the University of Washington working with Eric Steig and Greg Hakim. There she studied past changes in polar climate and the Greenland and Antarctic ice sheets. Jessica graduated from the University of Washington with a Doctor of Philosophy in Summer 2022.